Chemical evolution of star-forming galaxies in the overdense environment

ब्रह्माण्ड के अतिसघन वातावरण मे सितारा-निर्माण करने वाली आकाशगंगाओं का धात्विक विकास

Anshu Gupta

A thesis submitted for the degree of

Doctor of Philosophy

The Australian National University

Research School of Astronomy & Astrophysics

Submitted: 9th March, 2018

Accepted: 31th October, 2018

To Mom and Dad..

Declaration

I hereby declare that the work in this thesis is that of the candidate alone, except where indicated below or in the text of the thesis. The work was undertaken between October 2013 and March 2018 at the Australian National University (ANU), Canberra. It has not been submitted in whole or in part for any other degree at this or any other university.

This thesis has been submitted as a Thesis by Compilation in accordance with the relevant ANU policies. Each of the four main chapters are a completely self-contained articles that have been published in, or submitted to, a peer-reviewed journal. I have made significant contribution to each paper. The thesis has been excellent preparation for post-doctoral research, as I have experienced the full scientific process from planning and conducting observations to using simulations and producing peer-reviewed publications.

Chapter 2 is originally submitted as *Keck-DEIMOS flux calibration: A case study from an extragalactic survey* , A. Gupta, T. Yuan, M. Kaasinen, L. Kewley, submitted, PASP.

Chapter 3 is originally published as *Radial Distribution Of ISM Gas-phase Metallicity In CLASH Clusters at $z \sim 0.35$: A New Outlook On Environmental Impact On Galaxy Evolution*, A. Gupta, T. Yuan, K. Tran, D. Martizzi, L. Kewley, 2016, The Astrophysical Journal, 831, 104.

Chapter 4 is originally published as *Survival of Massive Star-forming Galaxies in Cluster Cores Drives Gas-Phase Metallicity Gradients : The Effects of Ram Pressure Stripping*, A. Gupta, T. Yuan, D. Martizzi, K. Tran, L. Kewley, 2017, The Astrophysical Journal, 842, 75.

Chapter 5 is originally accepted as *Chemical pre-processing of cluster galaxies over the past 10 billion years in the IllustrisTNG simulations*, A. Gupta, T. Yuan, P. Torrey, M. Vogelsberger, D. Martizzi, K. Tran, L. Kewley, F. Marinacci, D. Nelson, A. Pillepich, L. Hernquist, S. Genel, V. Springel, in press, MNRAS.

Anshu Gupta

9^{th} March, 2018

Acknowledgements

First, I would like to thank Prof. Lisa Kewley, for being an amazing and supportive supervisor. You gave me the freedom and means to find my own questions and pursue them for my thesis. Your excitement and the positive attitude towards everything is infectious and helped me to get through the PhD blues. I will always cherish the memories of parties, picnics and awesome writing retreats organised by you. I would like to thank Dr. Tiantian Yuan for your constant guidance, and patience. You helped me navigate the not-so-straightforward path from a student to an independent researcher. Thanks to Prof. Kim-Vy Tran for your guiding hand, insights and sharing her love for baking. You three will always be role models for me and I have learned a lot from each of you, both professionally and personally.

As always in Science, this thesis is outcome of collaboration with people across many institutes. I am truly grateful to my collaborators Dr. Davide Martizzi, Dr. Paul Torry, Prof. Mark Vogelsberger and the IllustrisTNG team for your invaluable inputs. I would also like to thank all members of Gears3D team for enriching my academic experience at Stromlo.

Thanks to all my friends at Stromlo, Melanie, Soniya, Ayan, Surya, Haiyang, Sarah, Mayuri, Ly, Thomas, and Fan. You guys are awesome and I enjoyed my time chatting, cooking, eating, and learning from all of you. Special thanks to Surya for listening to all my frustrated rants towards the end of my PhD. Thanks to Johanna, MariaRosa, Damien, Rose, and Jess, for making living in Canberra fun. MariaRosa and Johanna, you were awesome housemates (honorary) and I will always cherish all of our sensible and non-sensible discussions.

Finally, I would like to thank my parents for their constant encouragement and support. You always push me to strive for better things. I would like to thank Ankit for his constant presence. Thanks for patiently listening to my endless rants. Your balancing attitude makes the difficult times seem not so difficult.

Abstract

As the largest gravitationally bound systems in the Universe, galaxy clusters are a unique laboratory for studying the extremes of galaxy evolution. The general consensus is that the large cluster-scale halo and the hot intracluster medium plays a significant role in the morphological and colour transformation of galaxies. However, its effect on details of baryonic processes in cluster galaxies remains unknown. I use the gas-phase chemical abundance to trace the cumulative effect of the gas inflow/outflow modulated star formation history of a galaxy. Current observations of the gas-phase chemical abundance of star-forming galaxies in the cluster environment are highly uncertain. This thesis aims to answer whether, when and how environment affect the chemical evolution star-forming galaxies.

I present the first observation of cluster-scale radial metallicity gradients from star-forming galaxies in two CLASH clusters at $z \sim 0.35$: MACS1115+0129 and RXJ1532+3021, using observations with the DEIMOS spectrograph on the Keck II telescope. I use observations for RXJ1532+3021 to quantify the systematic uncertainties in the flux calibration of DEIMOS spectrograph. We find that the gas-phase metallicity of galaxies decreases as a function of projected cluster-centric distance for MACSJ1115+0129, i.e., galaxies near the cluster core are metal-rich compared to galaxies in the cluster outskirts. Star-forming galaxies in MACSJ1115+0129 are 0.20 dex metal-rich compared to counterpart field galaxies. The negative cluster-scale metallicity gradient in our observations is not driven by the stellar mass of galaxies.

Star-forming galaxies in RXJ1532+3021 shows a bimodal radial metallicity distribution and their mass-metallicity distribution is consistent with local field galaxies. We suspect that either interloper galaxies or an in-plane merger causes the bimodality of the radial metallicity distribution in RXJ1532+30, indicating that the cluster-scale abundance gradient can probe the dynamical state of a cluster.

We speculate that the negative cluster-scale metallicity gradient originates from ram-pressure stripping and/or strangulation processes in the cluster environments. The truncation of star formation in galactic outskirts due to ram pressure stripping (disk truncation) can observationally bias the aperture-based integrated metallicity measurements towards the central metal-rich part of the galaxy. To quantify this observational bias, I use a semi-analytic model of ram pressure stripping and conduct mock observations of disk truncated galaxies from the IFU survey of local galaxies.

Our ram pressure stripping model predicts a typical cluster-scale metallicity gradient of -0.03 dex/Mpc and a minimal metallicity enhancement of $+0.02$ dex at a fixed

stellar mass. The gas removal and subsequent quenching preferentially removes the low stellar mass galaxies from the cluster core. The small cluster-scale metallicity gradient predicted by our ram pressure stripping model is driven by the removal of the low mass galaxies from the cluster cores, which introduces a negative stellar mass gradient for the surviving population of star-forming cluster galaxies. Thus, our model shows that observational bias introduced by ram pressure stripping is not sufficient to explain the observed stellar mass independent negative cluster-scale abundance gradient and the metallicity enhancement on the mass-metallicity relation.

To identify the physical processes driving environment dependent chemical evolution, I use the new generation of cosmological simulation, in particular IllustrisTNG simulation. I investigate the evolution of the mass-metallicity relation for the star-forming cluster galaxies at $z = 0$, by tracking them back in cosmic time. The simulation predicts that star-forming cluster galaxies have higher gas-phase metallicity compared to field galaxies at $z \leq 1.0$. The metallicity enhancement predicted by simulation is qualitatively consistent with observations.

IllustrisTNG simulation predict the first systematic signature of "chemical pre-processing" of infalling cluster galaxies, i.e., the metallicity enhancement of cluster galaxies appears prior to their infall into the central cluster potential. In fact, infalling cluster galaxies show a $\sim 0.05\,\mathrm{dex}$ higher metallicity compared to field galaxies at $z \leq 0.5$ at a given stellar mass. By estimating the gas mass inflow rate and the metallicity of inflowing gas, we identify that the accretion of pre-enriched gas and the reduced gas mass inflow rate are key drivers of chemical evolution in the over-dense environment, particularly in the stellar mass range $10^9 < M_* < 10^{10}\,\mathrm{M}_\odot$. The signature of environment-dependent changes in properties of inflowing gas extends to infalling galaxies, i.e., for galaxies well outside the virial radius of clusters. Our work with IllustrisTNG motivates future observations of the chemical pre-processing and the pre-enrichment of inflowing gas in dense environments.

Contents

List of Figures

List of Tables

Chapter 1

Introduction

Space is big. Really big. You just won't believe how vastly, hugely, mind-bogglingly big it is. I mean, you may think it's a long way down the road to the chemist, but that's just peanuts to space.

–Douglas Adams, *The Hitchhiker's Guide to the Galaxy*

Galaxies live in a variety of environments – from voids to giant galaxy clusters, either in isolation or surrounded by hundreds and thousands of galaxies (Figure 1.1). Galaxy clusters form by the gravitational collapse of the largest overdensities in the primordial Universe. They are the first structure to undergo gravitational collapse, because of which galaxies residing in these massive clusters undergo accelerated evolution compare to galaxies in the average density Universe.

Separating the effect of external and internal drivers in galaxy evolution, i.e., "Nurture" versus "Nature" has been a long-standing debate in extragalactic astronomy (see review by De Lucia & Blaizot 2007). In the present day Universe, galaxy clusters only contain about 10% of the total galaxy population and contribute less than 1% to the cosmic star formation density. However, their contribution to the cosmic star formation density can be as large as 50% at higher redshift ($z > 2$ or nearly 10 Gyr ago; Chiang et al. 2017). Understanding how environmental processes affect galaxy evolution is key to understanding the rise and fall of the cosmic star formation density (Madau & Dickinson 2014) and the physics of galaxy evolution in general.

1.1 Environment and galaxy evolution

Galaxies in the low redshift Universe can be broadly separated into two categories: spirals and ellipticals. Spiral galaxies are rotation supported galaxies with a dominant flattened disk and blue colours produced by young stellar population indicative

Figure 1.1: Abell 1689. Photo credit: NASA, ESA

of the ongoing star formation. They are classified as 'spirals' because stars and gas density in the galactic disk reveal a clear spiral pattern. Elliptical galaxies are spheroidal systems supported by the random motion of stars. Elliptical galaxies have red colours suggestive of the old stellar population, which indicates little or no ongoing star formation activity. Historically, spiral and elliptical galaxies are also called as late- and early-type galaxies. Lenticular or S0 type galaxies are intermediate between spirals and ellipticals. They have a thin disk component without any clear spiral arm pattern.

The correlation between galaxy morphology and environment has been known for more than half a century, i.e., galaxies in the low density Universe are largely disky-spirals whereas galaxies in dense regions are mostly S0 or ellipticals (Hubble & Humason 1931; Shapley 1933; Abell 1965). Dressler (1980) first established this as "morphology-density" relation using a sample of 55 rich galaxy clusters. Since then numerous other studies have corroborated this relation (e.g., Poggianti et al. 1999; Van der Wel 2008).

Studies of local galaxies find that the fraction of blue, star-forming galaxies decreases with the environmental density (Kauffmann et al. 2003a, 2004; Baldry et al. 2006). Dependence of galaxy colour on the environmental density is partly a by-product of the morphology-density relation because S0 and elliptical galaxies have lower star formation rate than spiral galaxies. Observations of late-type galaxies show a systematic decrease in the mean star formation rate (SFR) with the environmental density in the local Universe (Balogh et al. 1999; Lewis et al. 2002; Balogh et al.

2004; Casado et al. 2015; Brown et al. 2017a). The excess of red, and elliptical galaxies and the sparseness of blue spiral galaxies in high density environment suggest that environment plays a significant role in quenching the star formation in cluster galaxies.

Observations in the local Universe (distances less than 100 Myr) show that the effects of stellar mass and environment on the star formation (SF) quenching are separable, indicating a stellar mass independent quenching mechanism at play in overdense environments (Van Den Bosch et al. 2008; Peng et al. 2010; Kovač et al. 2014). Local field galaxies show a monotonic decrease in the SFR with the stellar mass (main sequence, Brinchmann et al. 2004; Daddi et al. 2007; Elbaz et al. 2007). The SFR-stellar mass main sequence relation does not change in the cluster environment (Laganá & Ulmer 2018), but the fraction of passive galaxies increases significantly in cluster environments (Peng et al. 2010; Paccagnella et al. 2016; Erfanianfar et al. 2016). Peng et al. (2012) and Kovač et al. (2014) observed that the quenched fraction of central[1] galaxies primarily depends on the stellar mass, whereas the environment-dependent mechanisms have to be invoked to explain the quenched fraction of satellite[2] galaxies.

Observations of high redshift cluster galaxies indicate that the effect of stellar mass and environment on the SF quenching can be separated even at $z \sim 3$ (Muzzin et al. 2012; Lee et al. 2015; Darvish et al. 2017). In contrast, Kawinwanichakij et al. (2017) used data from the ZFOURGE survey and showed that the environmental quenching efficiency at $z > 0.5$ depends on the stellar mass of galaxies, suggesting inseparability of stellar mass and environmental quenching mechanisms at higher redshifts. Kawinwanichakij et al. (2017) found that the environmental quenching efficiency is very low at $z > 1.5$, in particular for low mass galaxies ($\log(M_*/\mathrm{M}_\odot) <$ 10.0). However, the environmental quenching mechanisms can account for nearly all passive low mass galaxies at $z < 1.0$ (Kawinwanichakij et al. 2017). Local studies also find that environmental quenching dominates for low mass galaxies ($\log(M_*/\mathrm{M}_\odot) < 10.0$; Peng et al. 2010).

Some observations of high redshift clusters ($z \sim 1.5$) find a higher fraction of star-forming galaxies in the cluster core compared to cluster outskirts, i.e., a complete reversal of the trend observed in local studies (Tran et al. 2010, 2015). However, the average SFR per galaxy in the cluster core is still smaller than in cluster outskirts (Tran et al. 2015). Recent simulations by Chiang et al. (2017) predict that the cosmic star-formation peaks for galaxies in the protocluster environment at an earlier epoch than for field galaxies, before subsequently dropping at a sharper rate than for field galaxies. Indeed, enhanced star-formation activity has been observed in high redshift protoclusters ($z \sim 2.5$; Shimakawa et al. 2018).

A number of physical processes related to the environment have been invoked to explain the observed evolutionary differences in the properties of field and cluster galaxies. These are outlined in the following subsections.

[1]in the center of the host dark matter halo
[2]not in the center of the host dark matter halo

Figure 1.2: Ram pressure stripping of spiral galaxy ESO 137-001. The blue streaks are the stripped star forming regions. The cluster center is to the top-right of the image. Photo credit: NASA/ESA/STScl

1.1.1 Galaxy harassment

Galaxy harassment is the cumulative effect of high-speed encounters between member galaxies and cluster substructures. Simulations show that the disks of the infalling galaxies can be completely destroyed after first or second passage through the cluster potential (Moore et al. 1996). Galaxy harassment has been primarily speculated as the source of the morphological transformation of spiral galaxies into elliptical or S0 type galaxies (George et al. 2013; Bialas et al. 2015). Haynes et al. (2007) speculate that galaxy harassment is responsible for the observed highly asymmetric galactic profile and disturbed H I disk of the galaxy NGC 4254 in the Virgo cluster.

Numerical simulations predict that the sensitivity of an infalling galaxy to be harassed depends on the orbits of the infalling galaxy into the cluster potential as predicted by numerical simulations (Mastropietro et al. 2005; Smith et al. 2015). Furthermore, galaxy harassment is found to be efficient at morphological transformation only if the galaxy passes within $40 - 100$ kpc from the cluster center (Smith et al. 2015). Dwarf galaxies on radial orbits through a cluster are completely destroyed by tidal interactions. Therefore, the surviving dwarf galaxies preferentially follow large pericentric orbits through the cluster (Annunziatella et al. 2016).

1.1.2 Ram pressure stripping

Ram pressure stripping (RPS) is a wind drag experienced by a galaxy moving through the hot intra-cluster medium (ICM) that can strip the gas associated with the galaxy. Figure 1.2 shows a spectacular example of RPS in the spiral galaxy ESO 137-001, where the star-forming gas can be seen trailing behind the galaxy. Gunn & Gott (1972) proposed that ram pressure exerted by the ICM on infalling galaxies is proportional to the density of the ICM at the location of the galaxy and the square of its infall velocity. This simple model of RPS can explain the gas deficiency of cluster galaxies (e.g., Chung et al. 2009; Boselli et al. 2014a). The neutral H I disk in most field galaxies has a spatial extent almost two times greater than the stellar disk (Cormier et al. 2016), whereas the neutral H I disk in cluster galaxies is smaller than or has the same size as the stellar disk due to RPS (Chung et al. 2009; Boselli et al. 2014b). Molecular gas is also affected by RPS although to a lesser extent because it exists deeper within the galaxy potential (Boselli et al. 2014b). The gas removal due to RPS in cluster environments has been used to explain the transformation of spiral galaxies into S0-type galaxies in galaxy clusters (e.g., Aragón-Salamanca et al. 2006; Bedregal et al. 2011).

Tails of neutral hydrogen gas can be seen trailing behind the stellar disks of galaxies in some spectacular displays of RPS (Figure 1.2, Chung et al. 2009; Cortese et al. 2010; Scott et al. 2015). Usually, the stripped gas remains loosely bound and does not form stars. However, some observations find ~ 100 kpc-scale neutral gas trails with a molecular gas component, out to a large distance from the stripped galaxy (Jáchym et al. 2014, 2017). Simulations show that the high pressure and density in massive clusters can induce SF in the gas trailing behind the galaxy by compressing the stripped gas (Kapferer et al. 2009; Tonnesen & Bryan 2012). Extreme ram pressure can even strip the star-forming regions of galaxies producing a "jellyfish" like geometry (Owen et al. 2006; Cortese et al. 2007; Owers et al. 2012; Poggianti et al. 2017). Bellhouse et al. (2017) found clear signatures of the on-going star formation in the stripped part of the galaxy.

Simulations predict that ram pressure can also lead to a short burst of star-formation in infalling cluster galaxies by compressing the gas supply, especially for galaxies with peripheral orbits (Bekki 2014; Steinhauser et al. 2016). Observations found an excess of post-starburst galaxies in clusters compared to the field environment, suggesting rapid quenching of SF (Dressler & Gunn 1982; Muzzin et al. 2014; Paccagnella et al. 2017). Muzzin et al. (2012) found an excess of post-starburst galaxies in the cluster core compared to the cluster outskirt at $z \sim 1$. Lopes et al. (2014) found a small increase in the fraction of blue galaxies at $\sim 0.4\,R_{200}$[3], before finally decreasing in the cluster center. Galaxies on their first infall can experience ram pressure compression that leads to a burst of star formation and rapid consumption of the gas supply, followed by a rapid quenching of SF. Consolandi et al. (2017) found enhanced SF in the leading end of an infalling galaxy with the stripped material falling back

[3] the radius within which the mean density is 200 times the critical density of the Universe

suggesting ram pressure compression in the leading end of the galaxy and stripping in the trailing end.

1.1.3 Strangulation

Ram pressure stripping can lead to an abrupt quenching of star formation. However, often only the loosely bound hot gaseous halo is stripped leaving a reduced amount of gas available for future star formation. The galaxy with stripped hot gaseous halo would continue to form stars until it consumes its remaining cold gas supply. This gradual quenching of star formation in a galaxy due to the absence of gas inflows to replenish the dwindling gas supply is referred to as strangulation (Larson et al. 1980; Balogh et al. 2000; Weinmann et al. 2009; Peng et al. 2015).

Scudder et al. (2012) found that gas exhaustion due to strangulation seems to be the dominant mechanism of SF suppression in compact group galaxies at $z \sim 0$. Observations of star-forming cluster galaxies over the past 10 Gyr find non-zero but low specific SFR (sSFR, SFR per stellar mass) for cluster galaxies compared to field galaxies, suggesting slow SF quenching indicative of the strangulation (Wagner et al. 2016; Rodríguez del Pino et al. 2017). A decreasing fraction of post-starburst galaxies with increasing cluster-centric distance also indicates that the star formation in cluster galaxies quenches slowly ($\sim$ 1Gyr; Paccagnella et al. 2016).

Taranu et al. (2014) used hydrodynamical simulations to show that long SF quenching time-scales are more effective at reproducing the cluster-centric gradients in colours of cluster galaxies than the rapid quenching mechanisms such as ram pressure stripping. However, most semi-analytic models of strangulation over-predict the fraction of quiescent red galaxies in clusters in particular at the low mass end ($\log(M_*/\mathrm{M}_\odot) < 10.0$; Baldry et al. 2006; Kimm et al. 2009; Guo et al. 2011). The assumption of instantaneous stripping of the hot gaseous component of the galaxy after the infall has been speculated as the reason behind the excessive quenching in semi-analytic models. Hydrodynamic simulations with gradual stripping of hot gas over a period of $\sim 1\,\mathrm{Gyr}$ are slightly better at reproducing the colour distribution of satellite cluster galaxies (McCarthy et al. 2008; Kang & van den Bosch 2008).

Separating the effects of ram pressure stripping, strangulation, and harassment on galaxy properties is not straightforward (e.g., Annunziatella et al. 2016). Different physical mechanisms must be invoked to explain all the observed properties of cluster galaxies. For example, both RPS and tidal interactions can be effective at removing the hot gaseous halo surrounding the galaxy. However, observationally constraining/identifying the responsible mechanism can be extremely challenging.

The gas-phase metallicity is a perfect tool to understand how the environment affects the evolution of star-forming galaxies because it represents the cumulative effect of gas inflow/outflow modulated star-formation history of a galaxy. Even the most recent burst of star-formation can affect the gas-phase metallicity of a galaxy because the most massive stars distribute their metal yield into the interstellar medium on a relatively short time-scale ($< 1\,$Myr). Hence, all the environmental processes affecting the star formation and gas content of a galaxy on short and long time-scale should leave an imprint on its gas-phase metallicity.

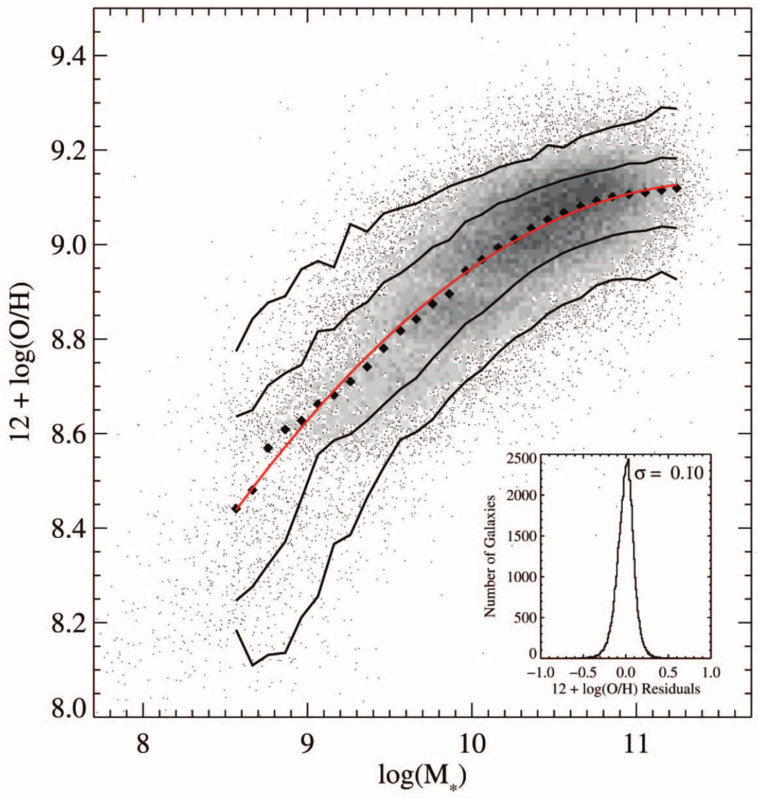

Figure 1.3: The relation between the stellar mass and the gas-phase oxygen abundance for star-forming galaxies in the SDSS. The filled squares represent median gas-phase metallicity in bins of 0.1 dex in stellar mass. The solid black lines show the contours enclosing 68% and 95% of the data. Figure reproduced from Tremonti et al. (2004)

1.2 Chemical Evolution of Star-forming Galaxies

In astronomy, all elements except hydrogen and helium are collectively termed as 'metals', because elements heavier than helium are mostly produced through nuclear reactions in stars. The relative abundances of all metals compared to hydrogen is often referred as the metallicity. The gas-phase metallicity of a galaxy is the relative abundance of total number of heavy elements relative to the number of hydrogen atoms in the interstellar medium (ISM). In extragalactic astronomy, metallicity is often defined by relative oxygen abundance and represented as $12 + \log \mathrm{O/H}$ for convenience.

The young, massive stars in star-forming regions produce Lyman continuum photons that ionises the surrounding ISM gas producing H II regions. The recombination of the ionised gas produces nebular emission lines of Hydrogen and collisionally excites forbidden lines from metal ions in the H II region such as [N II] λ6583, [O III] λ5007. The flux of the Hydrogen emission lines primarily depends on the Lyman continuum flux from young, massive stars, and hence is a direct proxy for the instantaneous SFR of the entire galaxy. The ratio of nebular emission lines give insight into physical properties of the ionised gas, such as ISM metallicity, electron density, pressure.

Direct estimation of the ISM metallicity depends on the electron temperature (T_e), which requires observation of temperature sensitive line ratios, e.g., [O III] λ4363 to [O III] λ5007. However, most auroral emission lines such as [O III] λ4363 are extremely weak, and hence difficult to observe. Often, theoretical and empirical calibrations based on strong emission line ratios such as [O II] $\lambda\lambda$3726, 3729, [N II] λ6583, and Hα λ6563 are used (Kewley & Dopita 2002; Pettini & Pagel 2004; Kewley & Ellison 2008; Kewley et al. 2013b).

Galaxies in the local Universe show a clear relationship between the stellar mass and the gas-phase metallicity, i.e., galaxies with higher stellar masses have higher metallicities as compared to galaxies with lower stellar masses. This is usually termed the mass-metallicity (MZ) relation. The correlation between the metallicity and stellar mass was first presented by Lequeux et al. (1979) for a sample of nearby irregular blue compact galaxies. Many observational studies have confirmed the existence of the MZ relation for local galaxies (Tremonti et al. 2004; Lee et al. 2006; Ellison et al. 2008; Zahid et al. 2012; Andrews & Martini 2013). Tremonti et al. (2004) used nearly 50,000 local galaxies from the Sloan Digital Sky Survey (SDSS), and found a relatively tight MZ relation for local galaxies extending over 3 orders of magnitude in the stellar mass (Scatter = $\pm$0.1 dex; Figure 1.3).

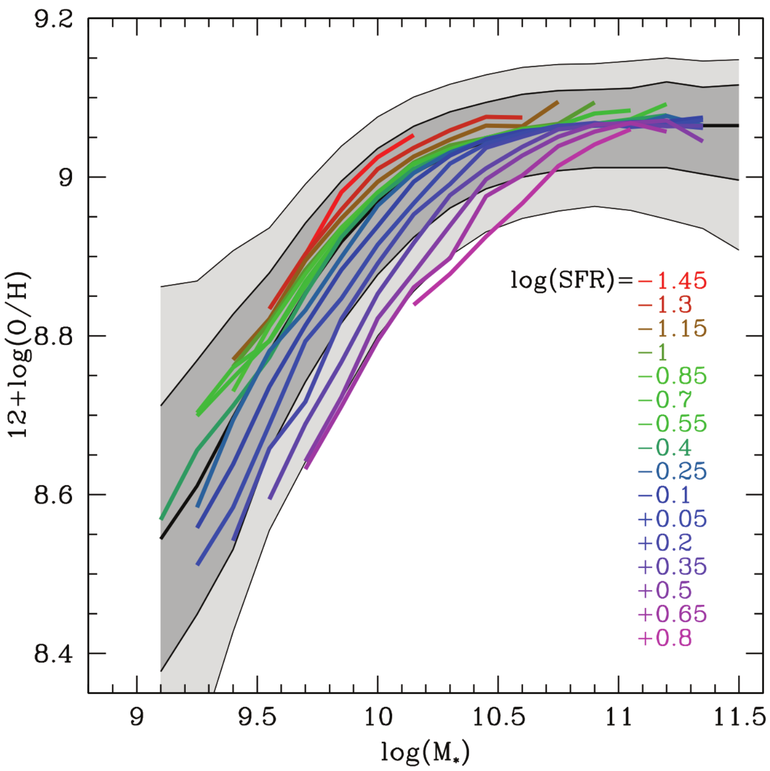

Figure 1.4: The mass-metallicity relation relation for SDSS galaxies. The coloured lines represents MZ relations for galaxies in bins of different star formation rates. The grey shaded area encompasses 60% and 90% of the data. Figure reproduced from Mannucci et al. (2010)

Observations of high redshift galaxies confirm the existence of the MZ relation at redshifts up to $z \sim 3.5$, although with an offset towards lower metallicity (Maiolino et al. 2008; Zahid et al. 2013; Sanders et al. 2015; Wuyts et al. 2016; Onodera et al. 2016; Suzuki et al. 2017). Zahid et al. (2014a) established a universal logarithmic MZ relation up to $z < 1.6$, where only the stellar mass at which metallicity saturates evolves with redshift, and attribute this to the change in the gas mass fraction of galaxies at higher redshifts. The absolute comparison of the MZ relation across cosmic time is uncertain because the normalisation of the MZ depends on the metallicity indicator used (Kewley & Ellison 2008). Additionally, it remains unclear whether the empirical metallicity calibrations derived from local studies can be used to measure metallicity of high redshift galaxies (Kewley et al. 2013a; Shapley et al. 2014).

Several authors have investigated the relationship between the intrinsic scatter in the MZ relation and the varying SFRs of galaxies. Ellison et al. (2008) reported that galaxies with higher sSFRs have systematically lower gas-phase metallicity compared to galaxies with lower sSFRs at the same stellar mass. Mannucci et al. (2010) and Lara-López et al. (2010) show that the MZ relation is just a 2-dimensional projection of more fundamental metallicity-relation (FMR) between the stellar mass, metallicity and SFR (Figure 1.4). Mannucci et al. (2010) found that the FMR does not evolve till $z < 2.5$, and that the observed evolution of the MZ relation can be accounted by the higher SFRs of high redshift galaxies. However, other observations find that the FMR evolves at high redshifts (Zahid et al. 2014b; Sanders et al. 2015; Oi et al. 2017)

The anti-correlation between the SFR and metallicity is slightly counter-intuitive because the higher SFR implies a higher rate of metal production in a galaxy. Moreover, it is unclear how metallicity, which represents the cumulative star formation history, depends on the instantaneous SFR. Telford et al. (2016) show that the signal-to-noise (S/N) cuts on individual emission lines, choice of metallicity diagnostics, and the aperture effects strongly affect the observation of a fundamental metallicity relation. Observations of spatially resolved galaxies in surveys like CALIFA and MaNGA also question the existence of a FMR (Barrera-Ballesteros et al. 2017; Sánchez et al. 2017). By comparing the metallicity at one effective radius for all star-forming CALIFA galaxies, Sánchez et al. (2017) do not observe any correlation between the metallicity and SFR.

1.3 Chemical evolution of cluster galaxies

Comparative analysis of the MZ relation in cluster and field environments is used to disentangle the effect of environment and stellar mass on the chemical evolution of galaxies. Numerous observations have focused on the how environment influences the chemical evolution of star-forming galaxies (e.g. Shields et al. 1991; Skillman et al. 1996; Mouhcine et al. 2007; Cooper et al. 2008; Ellison et al. 2009; Scudder et al. 2012; Hughes et al. 2013; Pasquali et al. 2012; Peng & Maiolino 2014; Darvish

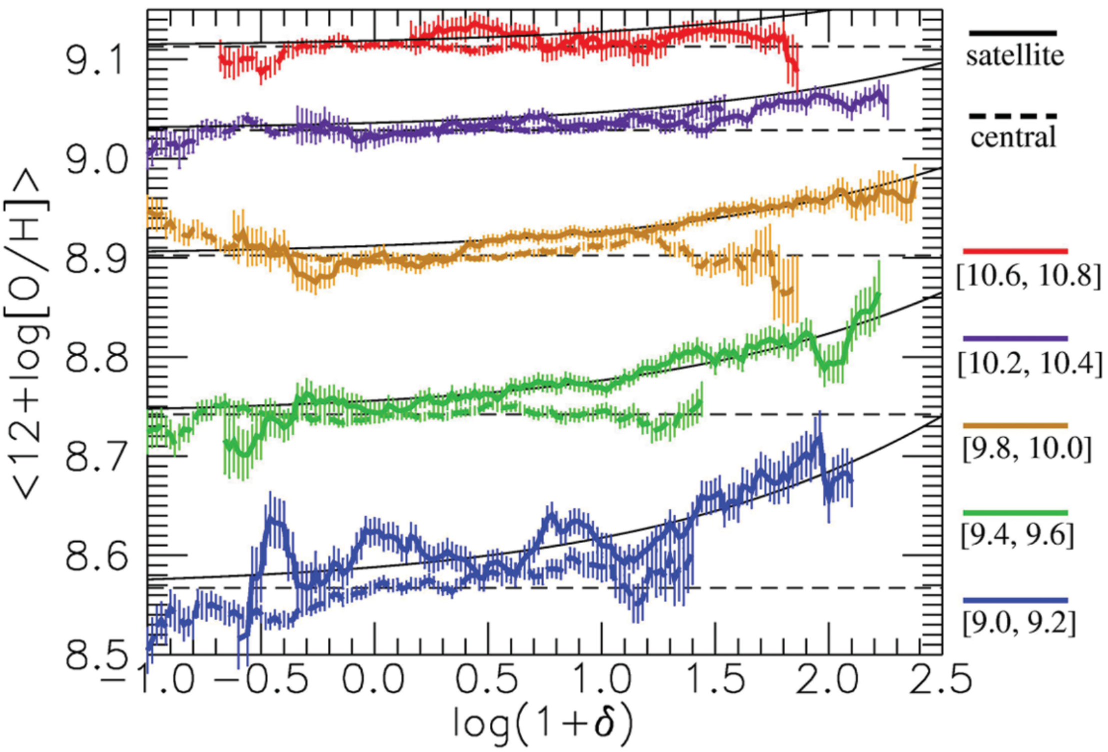

Figure 1.5: The average metallicity as a function of environmental overdensity for star-forming central (coloured dashed lines) and satellite (coloured solid lines) galaxies for different stellar masses. Horizontal black dashed lines indicate the average metallicity of the central galaxies in a stellar mass range given in legend. Solid black lines indicate a simple parameterization of environmental-dependent metallicity evolution. Figure reproduced from Peng & Maiolino (2014).

et al. 2015a; Pilyugin et al. 2017a), unfortunately without conclusive results.

1.3.1 In the local Universe

Shields et al. (1991) presented the first evidence of an environmental dependence of the metallicity, by analysing spectra of H II regions of spiral galaxies in the Virgo cluster. Ellison et al. (2009) found that local star-forming cluster galaxies from SDSS data are $0.03 - 0.05$ dex more metal-rich compared to the field galaxies. However, the metal enhancement depends on the local overdensities such as the presence of a nearest neighbour, rather than the large-scale cluster membership. Late-type isolated spiral galaxies in the Virgo cluster follow a similar MZ relation as isolated galaxies in field environments, further indicating insignificance of large-scale cluster membership (Hughes et al. 2013). The large scatter in the chemical abundance with respect to environmental density suggests a minimal role of environment in the chemical evolution of star-forming galaxies in the local Universe (Pilyugin et al. 2017a).

Semi-analytic models of galaxy formation predict different evolutionary pathways for central and satellite cluster galaxies. Pasquali et al. (2012) found significant offset in the gas-phase metallicity of central and satellite cluster galaxies at a fixed stellar mass. Peng & Maiolino (2014) further analysed the differential metallicity evolution of central and satellite cluster galaxies with environmental overdensity and found a strong dependence of the satellite metallicity on environmental overdensity (Figure 1.5). In fact, the metallicity of low stellar mass satellite galaxies ($< 10^{10}\,\mathrm{M}_{\odot}$) increases by almost 0.1 dex in the highest overdensity bins. The metallicity of central galaxies is largely independent of the environmental overdensity.

Petropoulou et al. (2012) observed that the slope of the MZ relation becomes flatter for dwarf galaxies ($10^{8} - 10^{9}\,\mathrm{M}_{\odot}$) in two massive cluster, in particular for galaxies in the Coma cluster. This suggests that the environmental imprint on the metallicity is stronger for dwarf cluster galaxies. Pilyugin et al. (2017a) also found a statistically significant (~ 0.05 dex) metallicity enhancement for low stellar mass galaxies ($10^{9.1} - 10^{9.5}\,\mathrm{M}_{\odot}$). By comparing the metallicity of cluster galaxies at small ($< 0.3\,R_{200c}$) and large ($> 0.8\,R_{200c}$) cluster-centric distance, Ellison et al. (2009) found that galaxies near the cluster centre are 0.03 dex more metal-rich compared to galaxies at larger distance. Petropoulou et al. (2012) also found a negative correlation between the cluster-centric distance and the metallicity of SF cluster galaxies, further indicating that the environmental density affects the metallicity of SF galaxies as the density in a cluster environment decreases with cluster-centric distance.

Strangulation of galaxies with stellar mass $< 10^{10.2}\,\mathrm{M}_{\odot}$ after infall can explain the higher fraction of metal-rich galaxies in the accreted region of the phase-space diagram compare to the phase-space region occupied by infalling galaxies for a cluster at $z = 0.4$ (Maier et al. 2016). Peng et al. (2015) show that slow quenching with a ~ 4 Gyr timescale via strangulation can explain the higher metal content of quiescent galaxies compared to star-forming galaxies. Darvish et al. (2015a) found that star-forming galaxies in a filamentary structure at $z \sim 0.53$ are $0.10 - 0.15$ dex more metal-rich compared to field galaxies at the same redshift. These observations show that the galactic metallicity is pre-processed in the intermediate density filamentary structure of the cosmos.

1.3.2 In the high redshift Universe

Only a limited number of observations of the MZ relation in cluster environment exist at high redshift ($z > 1.0$), and with contradictory results. Kacprzak et al. (2015) estimated the metallicity of 43 cluster members at $z \sim 2.0$ and found a minimal (0.02 dex) metal enhancement for high redshift cluster galaxies. Tran et al. (2015) also found no environmental dependence in the metallicity of SF cluster galaxies at $z = 1.67$. Whereas, Shimakawa et al. (2015a) found that galaxies in a protocluster at $z \sim 2.5$ are chemically enriched relative to the counterpart field galaxies. In contrast, Valentino et al. (2015) found that high redshift cluster galaxies are metal-poor compared to field galaxies due to their excess gas content.

High-redshift observations of the mass-metallicity relation are highly susceptible to the brightness limit and choice of emission line diagnostics. Most high redshift observations rely on the [N II]/Hα emission line ratio to estimate metallicity. However, this line ratio does not consider the evolving ionization parameter in high redshift Universe (Kewley et al. 2015), and differences in the ionization properties of galaxies in cluster and field environments (Kewley et al. 2016).

1.3.3 In cosmological simulations

Numerical simulations serve as a laboratory for astronomers, where we can conduct the experiment of building a Universe from scratch over and over again. Dark-matter only simulations are excellent at reproducing the cosmic distribution large-scale structure from the inhomogeneities in the cosmic microwave background (e.g., Springel et al. 2006). However, detailed properties of a galaxy depends on the astrophysical phenomena that affect the evolution of baryonic component under the gravitational potential of dark matter. Hydrodynamic simulations incorporates the details of baryonic physical processes such as star-formation, feedback, cooling as a subgrid parametrised prescription. Earlier version of hydrodynamic simulations fail to reproduce the key properties of galaxies such as stellar mass function, morphologies, gas and stellar components (e.g., Scannapieco et al. 2012, and references therein).

The new generation of cosmological hydrodynamic simulations reasonably recover the observed properties of galaxies such as stellar mass function, mass-metalllicity relation, star formation rate (Vogelsberger et al. 2014b; Schaye et al. 2014; Bahe et al. 2016; Torrey et al. 2017; Pillepich et al. 2018; Genel et al. 2017). They

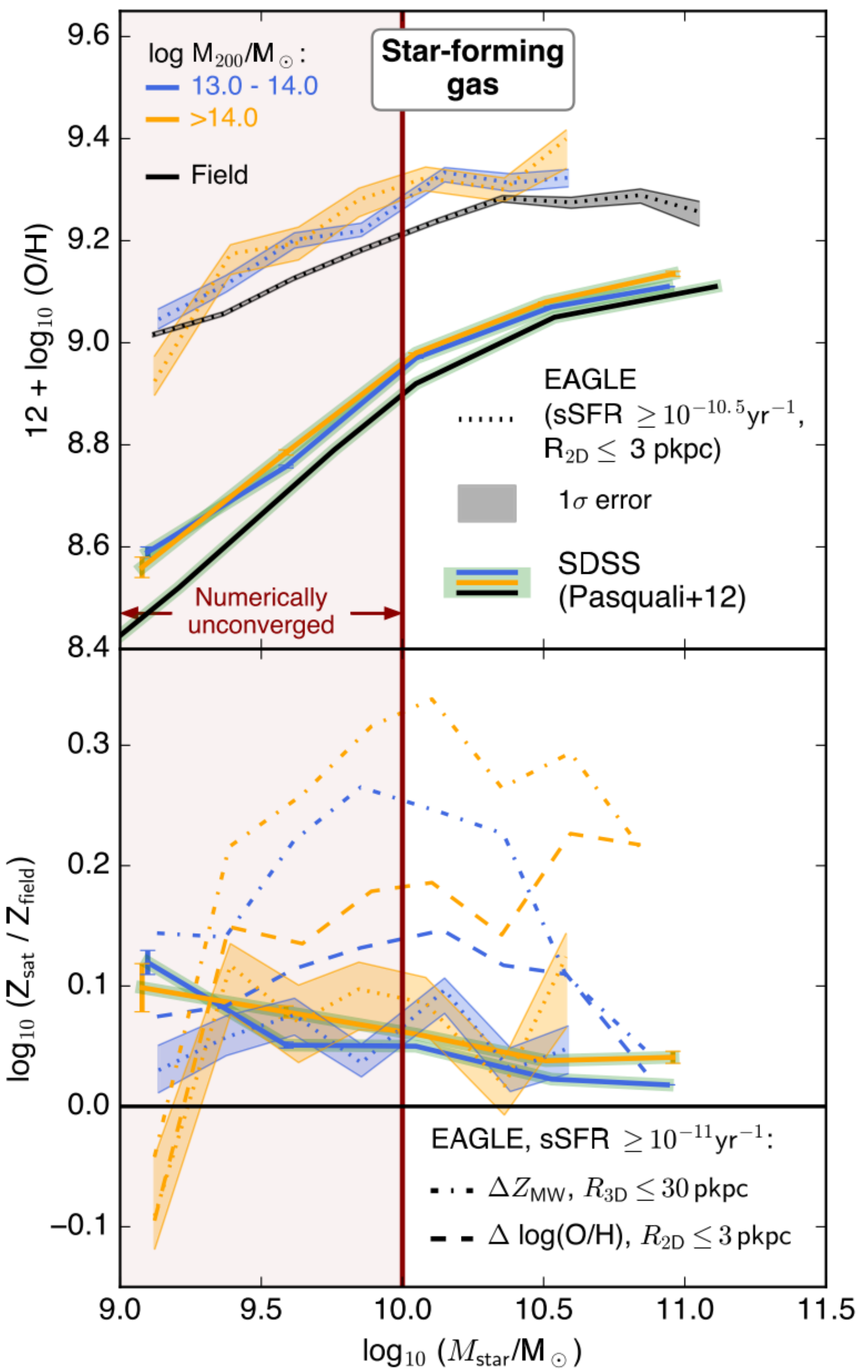

Figure 1.6: **Top panel:** Comparison of gas-phase oxygen abundance in star-forming field (black) and satellite (blue/orange) galaxies in EAGLE simulations. The width of the shaded region represents the 1σ statistical uncertainties on the median trend. The solid curves surrounded by green shaded regions show observational data from Pasquali et al. (2012). The red shaded regions represents the stellar mass range that could suffer from numerical resolution of EAGLE simulations. **Bottom panel:** Ratio of logarithmic metallicity between satellite and field galaxies. The dashed line show predictions from EAGLE for galaxies with sSFR $\geq 10^{-11}$yr^{-1} and the difference in the mass-weighted mean metallicity within a 3D aperture of 30 proper kpc (pkpc) as dash-dotted lines. The environmental predictions from EAGLE simulations matches with Pasquali et al. (2012) observation with local SDSS data. Figure reproduced from Bahe et al. (2016)

have sufficient volume ($\sim (300\,\mathrm{Mpc})^3$) to produce massive galaxy clusters with halo masses comparable to those observed ($\sim 10^{15}\,\mathrm{M}_\odot$; Vogelsberger et al. 2014b; Schaye et al. 2014; Vogelsberger et al. 2017). Thus, the new generation of cosmological hydrodynamic simulations make a powerful tool to understand the physics of the observed chemical enhancement of cluster galaxies, because they self-consistently model the formation of galaxies and their environment. Also, availability of a full 3-dimensional formation history in simulations is extremely useful to understand how and when the imprint of environmental processes appears on the metallicity.

Earlier cosmological simulations found an elevated galaxy metallicity of satellite galaxies compared to centrals (Davé et al. 2011; De Rossi et al. 2015). Genel (2016) uses Illustris simulations (Vogelsberger et al. 2014a) to understand the physical mechanism responsible for metallicity enhancement of satellite galaxies. The MZ relation of the central and satellite galaxies from the Illustris simulations is in qualitative agreement with observations from Pasquali et al. (2012). Genel (2016) compares the chemical evolutionary history of central and satellite galaxies in the narrow stellar mass range of $2 - 3 \times 10^{10}\,\mathrm{M}_\odot$. For this stellar mass range, Illustris simulations show that the central concentration of star formation and different star formation histories are responsible for the metallicity enhancement of satellite galaxies compare to central galaxies.

Using EAGLE simulations, Bahe et al. (2016) found that star-forming galaxies residing in massive halos have systematically higher global gas-phase metallicity than galaxies in average density environments (Figure 1.6). By analysing the radial metallicity profiles of galaxies in EAGLE simulations, Bahe et al. (2016) show that the metallicity enhancement of satellites is driven by an increased average metallicity at a fixed galacto-centric distance, and the stripping of low metallicity gas from the galactic outskirts. They speculate that the reduction in inflow of metal-poor gas and/or increased contribution of stellar ejecta to the depleted gas is responsible for the increased metallicity of satellite galaxies at a fixed galacto-centric radius.

1.4 Motivation

Current observations of the gas-phase metallicity of cluster galaxies are plagued by poorly understood systematic errors such as projection effects, interlopers, selection biases and metallicity diagnostics. The MZ relation studies in the local Universe relies on stacking the data from large galaxy surveys such as SDSS, because only a small fraction of galaxies in the local galaxy clusters are actively forming stars. For example, Ellison et al. (2009) combine data from 625 galaxy clusters to achieve a sample of $\sim$ 1300 cluster galaxies with nebular metallicity measurements, i.e., only 2 star-forming galaxy per cluster. The scatter introduced by the cluster-to-cluster variation can easily overwhelm the signature of the environmental dependent chemical evolution.

The formation history of a galaxy cluster can influence the physical properties of cluster galaxies, including their metallicity. Observations show a deficit in the fraction of star-forming galaxies in clusters regions that are in the process of fall into the cluster potential (a process referred to as 'pre-processing', Wetzel et al. 2013). Recent observations by Bianconi et al. (2018) found that the fraction of star forming galaxies in infalling groups does not change with respect to the cluster-centric distance, suggesting that gravitational and tidal interactions in infalling groups are efficient at quenching the star formation. Thus, combining data from hundreds of galaxy clusters at different stages of their formation history can dilute the small signatures of the environmental dependence of the MZ relation.

Differences in the definition of environment make the comparison across observational studies ambiguous. Ellison et al. (2009) found slightly different environmental dependence of the MZ relation ($0.02 - 0.05\,\text{dex}$), by using the distance to the cluster center, the distance to the 10 nearest galaxies and cluster halo mass as a measure of environment. Pilyugin et al. (2017a) also found a minimal dependence of the MZ relation on the environment, using the number of neighbours within a certain projected distance and velocity phase-space to separate the local SDSS galaxies into low- and high-density environment. On the other hand, Pasquali et al. (2012) and Peng & Maiolino (2014) separated the SDSS galaxies into centrals and satellites and found a strong correlation between the metallicity of satellite galaxy and environmental overdensity (Figure 1.5).

Additionally, the normalisation of metallicity measurements depends on the metallicity diagnostic. Kewley & Ellison (2008) showed that both the slope and the saturation metallicity of the MZ relation depends on the choice of metallicity diagnostic. Even the relative metallicity measurement could be affected by the systematic uncertainties introduced by the metallicity diagnostics (Kewley & Ellison 2008; Andrews & Martini 2013). On top of that, SFR cuts or brightness limit of observations can bias the observation against cluster galaxies undergoing the environmental-dependent transformations because they will preferentially have lower SFRs.

The new generation of cosmological simulations can help us untangle the complex interplay of various physical processes undergoing in galaxy clusters. In the current generation of numerical simulations, we can track the detailed properties of gas inflows and outflows as a function of environment and place constraints on their relative significance on the chemical evolution of cluster galaxies. The predictions from simulations can guide us to design future observations aimed at observing the small environment-dependent chemical enrichment signatures.

In this thesis, I observe galaxy clusters at intermediate redshift ($z \sim 0.35$) to have a statistical sample of star forming galaxies per galaxy cluster. The differences in the relative MZ relation between various galaxy clusters help us understand the effect formation history of a galaxy cluster has on the chemical evolution of its star-forming cluster galaxies. I present the first observation of a negative gradient in the integrated metallicity of cluster galaxies with the cluster-centric distance. Using IllustrisTNG cosmological simulations, I make the first systematic predictions of the chemical pre-processing of infalling cluster galaxies and identify that the inflow of enriched gas (pre-enrichment) is driving the chemical evolution in overdense environments. My Ph.D. dissertation combines observations, theoretical models, and cosmological simulations to identify the drivers of the chemical evolution in the cluster environment.

1.5 Thesis Outline

This thesis aims to answer several fundamental questions: whether the environment affects the chemical evolution of star-forming galaxies, and what the physical drivers of galaxy evolution in the cluster environment are?

Chapter 2 presents our work on quantification of flux calibration errors of the DEIMOS spectrograph. It presents our observation and data reduction technique with DEIMOS.

Chapter 3 presents observations of a cluster-scale abundance gradient in two galaxy clusters at $z \sim 0.35$; MACS1115+0129 and RXJ1532+3021, using observations from Keck/DEIMOS. My observations show that the cluster-scale abundance gradient is an alternate method to identify the environmental effects on chemical evolution.

In Chapter 4, I investigate whether truncation of the star formation in the outer galactic disk is sufficient to reproduce observations of cluster-scale abundance gradients and metallicity enhancement on the mass-metallicity relation. I use a self-developed analytic model of ram pressure stripping and conduct mock observations of CALIFA galaxies.

Chapter 5 presents the chemical enrichment history of galaxies in a set of new generation cosmological hydrodynamical simulations (IllustrisTNG). By identifying the progenitors of the present day cluster galaxies, I investigate whether the metallicity enhancement of cluster galaxies emerges before or after infalling on to the main cluster halo.

Chapter 6 summarises the main conclusions of my thesis. It briefly describes the current and future work stimulated by my thesis.

Chapter 2

DEIMOS/Keck flux calibration

Context and Contribution

This chapter is originally submitted as *Keck-DEIMOS flux calibration: A case study from an extragalactic survey* **, A. Gupta, T. Yuan, M. Kaasinen, L. Kewley, submitted, PASP. This chapter is included in the thesis as a representation of my contribution to quantification of flux calibration errors for DEIMOS spectrograph at Keck-II telescope. The whole paper was written by myself with suggestions provided by co-authors.**

2.1 Introduction

Optical spectroscopy has played a vital role in shaping the modern understanding of our Universe such as cosmic expansion (see review by Tegmark et al. 2004), large-scale structure formation (e.g., Broadhurst et al. 1990; Eisenstein et al. 2005; Blake et al. 2011) and the evolution of fundamental physical properties of galaxies with redshift (e.g., Cowie et al. 1996; Le Fèvre et al. 2005; Kobulnicky & Kewley 2004; Lilly et al. 2007; Zahid et al. 2011; Yuan et al. 2013a).

Multi-object spectroscopy is the simultaneous spectroscopy of hundreds of targets spread over a wide field of view (FOV). Multi-object slit spectroscopy is ideal for observing crowded regions of the Universe such as globular clusters (Pota et al. 2013), galaxy clusters (Tanaka et al. 2013; Richard et al. 2011; Bayliss et al. 2011; Ebeling et al. 2014) and for conducting large spectroscopic surveys of field galaxies (e.g., Davis et al. 2002; Scoville et al. 2007; Jones et al. 2009; Cooper et al. 2012; Newman et al. 2013; Darvish et al. 2015b). Almost all modern telescopes have optical or near-infrared multi-object spectrograph, e.g., GMOS at Gemini with $30-60$ slits and a FOV of $5.5' \times 5.5'$ (Oke et al. 1995), DEIMOS at Keck-II with $150-200$ slits and FOV of $16' \times 4'$ (Faber et al. 2003), VIMOS at VLT with $40-200$ slits and FOV of $4 \times 7' \times 8'$ (LeFevre et al. 2003), MOIRCS at Subaru with 40 slits and FOV of $4' \times 7'$ (Suzuki et al. 2008) and MOSFIRE at Keck-I with $\sim$30 slits and FOV of $6.1' \times 6.1'$ (McLean et al. 2012).

The absolute flux calibration of a spectrograph is essential to extract accurate information from a spectrum. Estimating physical quantities such as star formation rates (e.g., Kennicutt, Jr. 1998), dust extinction (e.g., Calzetti et al. 2000) and luminosity of supernovae (e.g., Riess et al. 1998) depends on the accuracy of the flux calibration. Stellar population models are based on stellar spectral libraries that are flux calibrated (e.g., Bruzual & Charlot 2003). Moreover, accurate flux calibration of data from individual instrument is essential in order to combine and analyse multi-wavelength data from different instruments (e.g., Sobral et al. 2015).

The standard method of flux calibration with any spectrograph is to observe a spectrophotometric flux standard star and derive the flux scaling relation. However, accurate flux calibration of the DEep Imaging Multi-Object Spectrograph (DEIMOS) on Keck-II is non-trivial. DEIMOS is a large spectrograph with a single slitmask of size 28 inches and 8 2048×4096 pixel science CCDs. Each spectrum spans 2 CCDs; referred to as the 'blue' and the 'red' sides (Faber et al. 2003). The large slitmask size, in combination with instrument flexure, leads to uneven slit illumination for different CCDs, which can result in systematic differences in the response of different CCDs. The brightness of the source is dependent on its location with respect to the readout amplifier (Bohlin et al. 2014).

Quantifying the flux calibration errors for DEIMOS is challenged by the systematic differences among CCDs. For this reason, DEIMOS has been primarily used for redshift identification, kinematic analysis and equivalent line widths measurements in the extragalactic community where absolute flux-calibration is not necessary (e.g., Schenker et al. 2012; Ebeling et al. 2014; Bellstedt et al. 2017). Flux-calibrated DEIMOS data has a much wider scientific application and can be extremely useful in studies such as emission line ratio analysis of galaxies in $0.5 < z < 1.6$, where a subset of the strong emission lines span across both the optical and near infra-red wavelengths (e.g., Sobral et al. 2015; Kaasinen et al. 2016). However, no literature has reported the quantitative errors of DEIMOS flux calibration, even after 16 years of its commissioning. This motivates us to present a simple case study on the flux calibration of DEIMOS with the goal of providing a quantitative reference on using DEIMOS in a flux-calibrated manner.

In this paper, we investigate the systematic differences in the absolute flux calibration of DEIMOS across its 8 CCDs. We compare two DEIMOS flux calibration techniques recommended by Keck: (i) separate flux calibration curves for each CCD (slitless mode) and (ii) a single flux calibration curve for all CCDs (longslit mode). Our observations are summarised in Section 2.2. We describe the data reduction in Section 2.3, including the longslit and slitless modes of flux calibration. We describe our testing methods in Section 2.4 and conclude in Section 2.5. All magnitudes are expressed in the AB system.

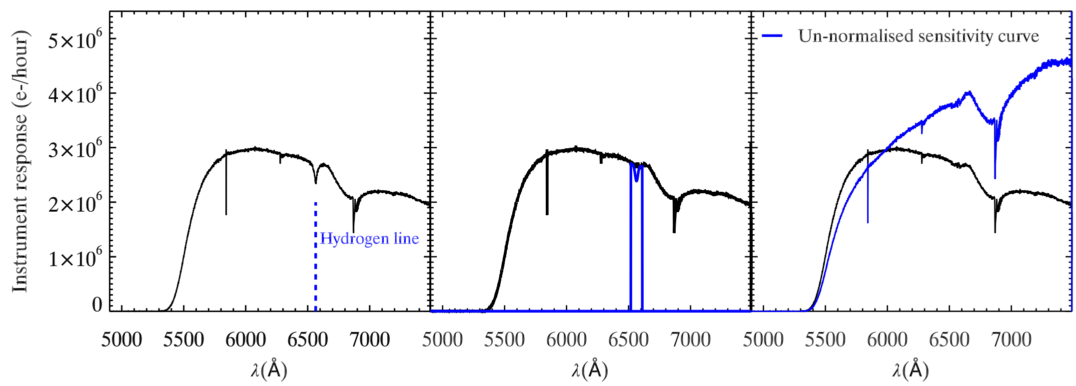

Figure 2.1: Derivation of the sensitivity curve using the standard star G191B2B for the blue CCD of DEIMOS. The absolute spectrum of the star is obtained from the CALSPEC Calibration Database. **Left panel:** The black curve shows the observed stellar spectrum. The blue dashed line represents the stellar absorption features identified using the absolute stellar spectrum. **Middle panel:** The observed stellar spectrum after correcting for the stellar absorption (black). The blue curve represents the best-fit absorption profile. **Right panel:** The blue curve represents the stellar blackbody profile corrected spectrum. The blue curve represents the sensitivity curve for the blue CCD before normalisation. The black curve is same as in the middle panel.

Table 2.1: Observation summery - DEIMOS flux calibration

Targets	α(J2000)	δ(J2000)	Mask	airmass	Exposure time
RXJ1532+30	15:32:53.8[a]	+30:20:58[a]	Multi-slit	1.09	$5 \times 1200s$
G191-B2B[b]	05:05:30.6	+52:49:54	Long-slit	1.19	45s
G191-B2B[c]	05:05:30.6	+52:49:54	no mask (CCD1)	1.19	15s
G191-B2B[c]	05:05:30.6	+52:49:54	no mask (CCD2)	1.19	15s
G191-B2B[c]	05:05:30.6	+52:49:54	no mask (CCD3)	1.19	15s
G191-B2B[c]	05:05:30.6	+52:49:54	no mask (CCD4)	1.19	15s

Notes:

[a] Coordinates of the BCG centroid (J2000)

[b] Used for telluric correction and longslit mode flux calibration

[c] Slitless mode flux calibration

Seeing $\sim 0.8''$

2.2 Sample selection and Observations

To quantify the accuracy of flux calibration for DEIMOS, we use the data from our Gravitationally Lensed-galaxies Observable With-Adaptive Optics (GLOW-AO) survey (Chapter 1). In the GLOW-AO survey, we observe 8 strong lensing clusters from the Cluster Lensing And Supernova survey with Hubble (CLASH; Postman et al. 2012), including RXJ1532+3021. The GLOW-AO survey targets lensed galaxies in the redshift range of $0.8 < z < 1.6$ that can be followed-up with adaptive optics. A single DEIMOS slitmask can have ~ 150 slits but the candidate lensed galaxies only occupy 10-20 slits. We fill the rest of the slitmask with bright cluster members and field galaxies.

All observations were conducted on UTC February 24, 2014 with a 600ZD grating, an OG550 filter and a central wavelength of 7500 Å. The wavelength coverage of our spectra is $5500\,\text{Å} - 9800\,\text{Å}$ with a dispersion of $0.65\,\text{Å}\,\text{pixel}^{-1}$. The slit width of all observations was $1''$. Table 2.1 summarises the observations for the data used in this paper.

We use the spectrophotometric standard DA-type white dwarf star G191B2B ($m_{\rm V} = 11.74$) to flux calibrate our data (Oke 1990; Rauch et al. 2013) because white dwarfs are relatively simple objects with fewer metal lines compare to other stars. We obtain its absolute spectrum from the CALSPEC Calibration Database[1]. A bright white dwarf star HIP 23694 was simultaneously observed to estimate the accuracy of our flux calibration technique for bright targets. HIP 23694 has r-band magnitude $m_r = 9.72$ (Munari et al. 2014). We use the data obtained for the cluster RX J1532+3021 ($z = 0.35$) to quantify and compare the accuracy of our flux calibration techniques for faint targets.

To measure the differential sensitivity of DEIMOS CCDs, we acquire a separate spectrum of the standard star by manually repositioning the star on each CCD. Traditionally, the longslit mode is used to acquire the standard star spectrum. However, in the longslit mode the star is positioned on the 3rd and 7th CCDs of DEIMOS. Manually repositioning the standard star on DEIMOS CCDs can be achieved more easily in the slitless mode because the star remains in the FOV during small telescope adjustments.

For the slitless mode observations, we first centre the standard star G191B2B using the $1''$ longslit, which positions the stellar spectrum on the 3rd and 7th CCDs. We then remove the slitmask and acquire an image to confirm the location of the standard star on the detector. Finally, we reposition the star on each CCD through incremental telescope adjustments and image acquisitions, acquiring a spectrum for each desired CCD.

[1] See http://www.stsci.edu/hst/observatory/crds/calspec.html

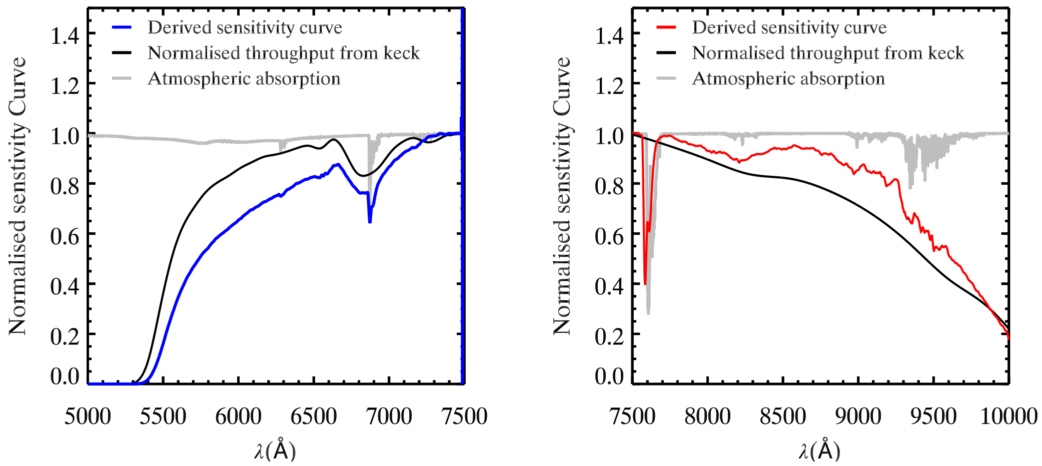

Figure 2.2: Normalised sensitivity curves for the blue (left panel) and red (right panel) CCDs from the longslit mode observation of the standard star G191B2B. The black curve in each panel represents the normalised spectroscopic throughput for the respective CCDs provided by the Keck observatory. The grey curve in both panels shows the atmospheric transparency curve[3]. Our sensitivity curves nearly follows the general shape of the Keck spectroscopic throughputs. The difference between our sensitivity curves and Keck spectroscopic throughputs is because of atmospheric absorption (Keck throughput considers only the response from the telescope and instrument).

2.3 Data Reduction

We reduce the data in two steps. We use the spec2d pipeline (Cooper et al. 2011; Newman et al. 2013) to reduce the raw spectra. The spec2d pipeline produces a 2-dimensional (2D) slit spectra for each object after correcting for the instrument bias, flat-fielding, slit-tilt and cosmic rays. The spec2d pipeline also performs wavelength calibration of the data. Secondly, we apply our IDL-based code, to correct for the atmospheric absorption, instrument sensitivity and to flux calibrate the 2D slit spectra.

We compare the accuracy of flux calibration using two techniques: (i) longslit mode and (ii) slitless mode. The longslit mode is the traditional flux calibration technique in which a single stellar spectrum is acquired by placing a longslit on the standard star. In the longslit mode, a single scaling relation is used to convert the net signal across all DEIMOS CCDs into the absolute flux density. The slitless mode is the non-traditional flux calibration technique in which we derive a separate scaling relation for each CCD by acquiring a separate standard star spectrum on each CCD. By comparing the longslit and slitless mode techniques, we quantify the effect of the differential CCD sensitivity on the flux calibration accuracy.

2.3.1 Longslit Mode

Instrument sensitivity correction

For instrument sensitivity correction, we use the longslit mode observation of the standard star G191B2B (Section 2.2). In this work, we define the *sensitivity curve* as the dimensionless quantity representing the convolution of the instrument response and the atmospheric absorption as a function of wavelength. Figure 2.1 shows the derivation of the sensitivity curve from the observed stellar spectrum for the blue CCD. We first extract the stellar 1D-spectrum by fitting a Gaussian curve along the spatial profile from the 2D slit spectrum and integrating the flux within the full width at half maximum (FWHM). The intrinsic stellar features such as stellar absorption at 6563 Å and the underlying black body profile at 60920 K (Gianninas et al. 2011) were fitted and removed. The sensitivity curve is represented by the normalised 1D stellar spectrum after correcting for the intrinsic stellar features. The normalisation is necessary because sensitivity curve represents the relative instrument sensitivity convolved with the atmospheric absorption as a function of wavelength.

Figure 2.2 shows the derived sensitivity curves for the blue and red CCDs. Our sensitivity curves matches the normalised spectroscopic throughputs[2] (black curves Figure 2.2) provided by the Keck observatory, except for the clear telluric bands at $6850-6960$ and $7580-7700$Å. The difference between the normalised Keck throughput and our sensitivity curves is because Keck spectroscopic throughputs represent the convolution of the telescope and instrument response, and does not include atmospheric absorption[3]. Also, different observing conditions such as variations in seeing and airmass can also contribute to the difference in the Keck spectroscopic throughputs and the sensitivity curves derived by us.

We divide all 2D slit spectra by the derived sensitivity curves to simultaneously correct for the atmospheric absorption and instrument response function. This calibration is also useful in applications of DEIMOS in non-flux calibrated cases.

Flux Calibration

In the longslit mode of flux calibration, we utilise the longslit mode observation of the spectrophotometric standard star G191B2B. We define the flux calibration curve (Fcc) as:

$$\mathrm{Fcc}_{\mathrm{longslit}}(\lambda) = \frac{N_e(\mathrm{e}^-/\mathrm{hour})}{F^*_{ab}(\mathrm{erg/s/cm^{-2}})}, \tag{2.1}$$

where N_e is the observed signal from the standard after correcting for the instrument sensitivity (Section 2.3.1), and F^*_{ab} is the absolute flux density of the standard star. Both N_e and F^*_{ab} are wavelength dependent. Note that the units for DEIMOS

[2] See https://www2.keck.hawaii.edu/inst/deimos/ripisc.html

[3] See http://www.gemini.edu/sciops/telescopes-and-sites/observing-condition-constraints/ extinction

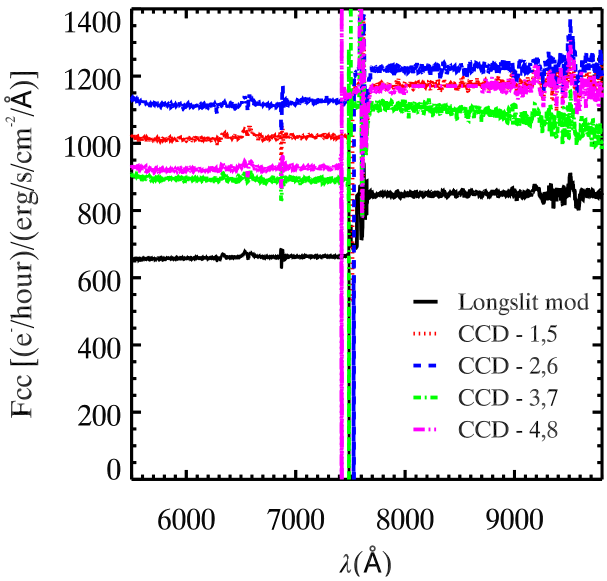

Figure 2.3: The coloured curves show the flux calibration curves ($\mathrm{Fcc}_{\mathrm{slitless}}(\lambda)$) for the different DEIMOS CCDs derived from the slitless mode observations of the standard star G191B2B. The black curve represents the $\mathrm{Fcc}_{\mathrm{longslit}}(\lambda)$ derived form the longslit mode in Section 2.3.1. The gap at ~ 7500 Å indicates the switch in CCDs from the blue to the red.

spectra are e^-/hour. The absolute flux density (F^*_{ab}) for standard star G191B2B is obtained from the CALSPEC Calibration Database[1]. We obtain N_e by dividing the 1D stellar spectrum with the sensitivity curve derived in Section 2.3.1, simultaneously correcting for the instrument sensitivity and the atmospheric absorption in the observed stellar spectrum.

Figure 2.3 shows the derived flux calibration curve from the longslit mode observations of the standard star ($\mathrm{Fcc}_{\mathrm{longslit}}(\lambda)$). The median conversion factor ($\mathrm{Fcc}_{\mathrm{longslit}}(\lambda)$) for the blue and red CCDs is 660 (e^-/hour)/(erg/s/cm^{-2}/Å) and 850 (e^-/hour)/(erg/s/cm^{-2}/Å) respectively. To perform flux calibration in the longslit mode, we divide the instrument sensitivity corrected spectra of target objects by $\mathrm{Fcc}_{\mathrm{longslit}}(\lambda)$ (the black curve in Figure 2.3), irrespective of the CCD the individual spectrum was observed on.

2.3.2 Slitless Mode

We consider the differential DEIMOS sensitivity to perform flux calibration using the slitless mode observation by deriving a separate flux calibration curve ($\mathrm{Fcc}_{\mathrm{slitless}}(\lambda)$) for each CCD. The flat-fielding and wavelength calibration in slitless observation mode is not straightforward. It is impossible to take arc and flat-fielding calibration frames in the slitless mode because the effective "slit" is the entire FOV. Therefore, we use the calibration frames from the longslit mode observation of the standard star.

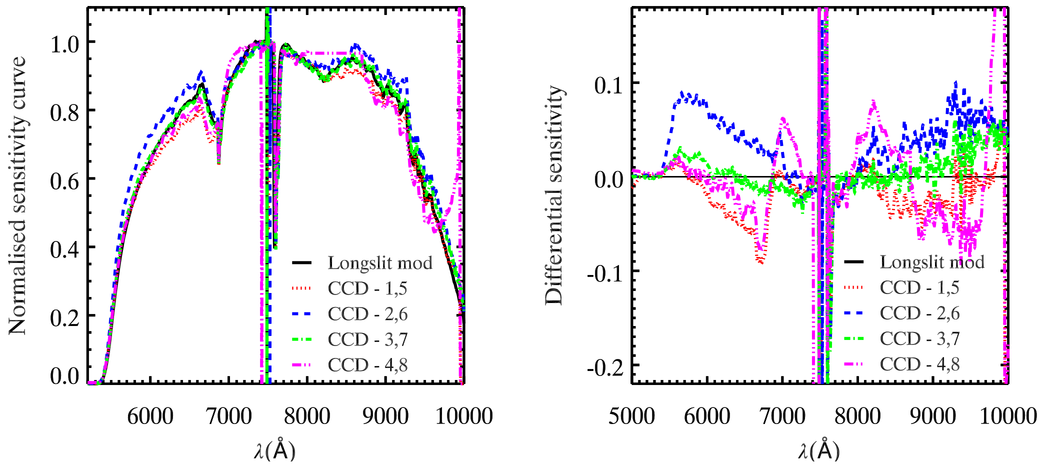

Figure 2.4: Left panel: Comparing the sensitivity of individual CCDs derived via the slitless mode. The black line represents the sensitivity curve we derived from the longslit mode in Section 2.3.1. The gap at ~ 7500 Å indicates the gap in CCDs from the blue to the red. **Right panel:** The difference between the sensitivity curve of individual CCD and the sensitivity curve derived in the longslit mode (black curve in left panel of Figure 2.4). The sensitivity curves of individual CCDs shows wavelength dependent variations that can vary by more than 10% from the longslit mode sensitivity curve.

To check the accuracy of the wavelength calibration, we match the stellar absorption feature at 6563 Å and atmospheric absorption at 7600 Å. We estimate a constant wavelength offset between $5 - 30$ Å depending on the CCD and correct for it while deriving the sensitivity curve for each CCD. In the slitless mode, the spectra of all objects in the FOV is acquired. To identify our standard star, we match the stellar absorption features in the observed stellar spectrum with the absolute flux density spectrum of the standard star.

Instrument sensitivity correction

We derive a separate sensitivity curve for each DEIMOS CCD from the slitless mode observations of the standard star G191B2B (Figure 2.4) using the procedure described in Section 2.3.1. Figure 2.4 shows the difference in the sensitivity of different DEIMOS CCDs with respect to the sensitivity curve derived from the longslit mode observation of the same standard star. The difference between the CCD sensitivity curves can be as large as 10% and are wavelength dependent (Figure 2.4: right panel). The slitless mode sensitivity curve for chip 3 and 7 shows the best agreement with the sensitivity curve from the longslit mode observation as would be expected.

Flux Calibration

We use equation (2.1) to derive a separate flux calibration curve for each CCD from the slitless mode observations of the standard star. We derive N_e for each CCD by dividing the observed stellar spectrum with the respective sensitivity curve of the CCD (left panel of Figure 2.4). The flux calibration curves derived for different CCDs are compared in Figure 2.3. We observe wavelength dependent differences as large as 50% between the $\mathrm{Fcc}_{\mathrm{slitless}}(\lambda)$ for different DEIMOS CCDs (Figure 2.3). To conduct flux calibration in the slitless mode, we divided the 2D slit spectra with the derived $\mathrm{Fcc}_{\mathrm{slitless}}(\lambda)$ after matching with DEIMOS CCDs.

2.3.3 Galactic Extinction

We correct spectra of extragalactic targets for Galactic extinction using the parametrisation by Fitzpatrick (1999). The average extinction for RXJ1532+3021 targets is $E(B-V) = 0.067$, which leads to minimal change in the observed flux density of targets. For stellar targets, we apply an $E(B-V) = 0.0005$ (Groenewegen & Lamers 1989).

2.3.4 Slit-loss Estimation

Estimating slit-loss is crucial to quantify the statistical and systematic errors in the flux calibration. Almost 80% of our targets are galaxies at $z \sim 0.35$ that have an angular size greater than the average seeing ($\sim 0.7''$) and the slit width ($1.0''$) of our observations. Hence, only a fraction of light from the observed galaxies is captured. The same is true for the longslit mode observations of the standard star.

Modified longslit calibration

Without the slit-loss correction, the longslit mode observation underestimates the light from the standard star, thereby overestimating the flux in the science target spectrum. The 2D slit spectra are generated by the summation of photons within the slit-width, giving us a spectrum at each pixel along the slit. In the longslit mode the slit width is $1''$, whereas the slitless mode observations have no aperture. Therefore, the total flux observed for the standard star in the longslit mode is less than the total flux in the slitless mode. The loss of flux due to the finite slit width in the longslit mode accounts for the difference in median $\mathrm{Fcc}(\lambda)$ values derived from the longslit versus slitless mode (Figure 2.3). We derived a slit loss factor of 0.85 in the longslit mode, by taking the ratio of the total stellar flux in the longslit versus the slitless mode observations. Thus, the modified flux calibration curve for

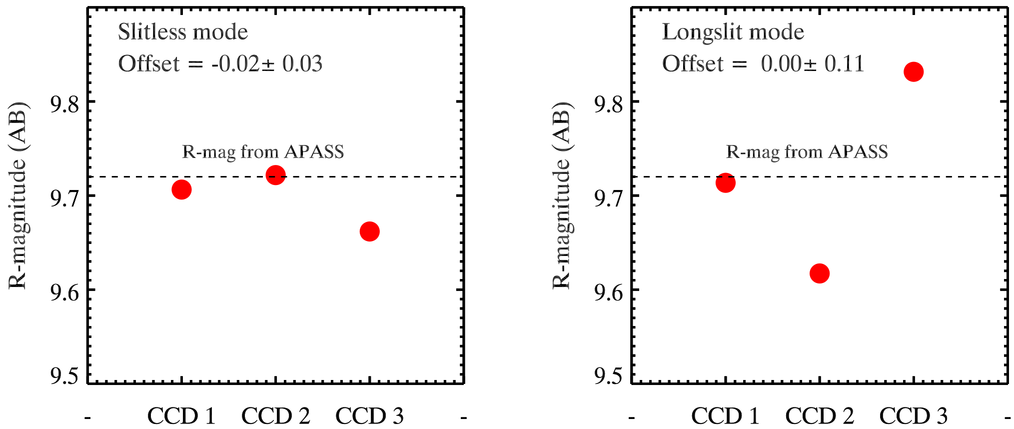

Figure 2.5: Comparison between the R-band spectroscopic magnitudes measured for star HIP 23694 across different CCDs. **Left panel:** slitless mode. **Right panel:** longslit mode. The mean and the 1-sigma standard deviation are displayed in the legend of each panel. The dashed line represents the photometric magnitude for the star form the APASS survey (Munari et al. 2014).

the longslit mode is given by,

$$Fcc'_{\text{longslit}}(\lambda) = \frac{Fcc_{\text{longslit}}(\lambda)}{0.85} \tag{2.2}$$

where $Fcc_{\text{longslit}}(\lambda)$ is derived in the longslit mode in subsection 2.3.1. The slit-loss factor between the longslit mode and the slitless mode is equivalent to the loss factor for an 0.7″ (seeing of the observations) object observed with a 1″ slit width. We use the $\text{Fcc}'_{\text{longslit}}(\lambda)$ to conduct flux calibration in the longslit mode.

Aperture correction for the test galaxy sample

Most galaxies in our sample were observed with an average seeing of 0.7″ and are spatially resolved. To calculate the absolute flux of an integrated galaxy spectrum, we need to correct for the flux lost due to the limited slit width. We obtain the 2D spatial extent of galaxies from the Sloan Digital Sky Survey (SDSS; Alam et al. 2015) photometric data. Assuming the same Gaussian width (σ) for the modelled profile and the SDSS photometric data, the slit loss factor is given by:

$$c = \frac{\text{erf}(\sqrt{\ln 2})}{\text{erf}(0.5/\sqrt{2}\sigma_{SDSS})}, \tag{2.3}$$

where σ_{SDSS} is from the SDSS data (Alam et al. 2015). The modelled photometric magnitudes in the SDSS catalog are generated by integrating flux within the FWHM. The extra factor of $\text{erf}(\sqrt{\ln 2})$ in the numerator accounts for the SDSS aperture size. To perform aperture correction, we divide the flux calibrated spectra with the slit-loss factor from Equation (2.3).

2.4 Comparing flux calibration techniques

2.4.1 Using stellar spectra

To compare the accuracy of our two flux calibration schemes (Section 2.3.1), we estimate the absolute flux of a bright test star HIP 23694 that was observed across multiple DEIMOS CCDs. The star HIP 23694 ($m_r = 9.72$) was observed on the 1st, 2nd and 3rd CCD of DEIMOS. We use the value of $\mathrm{Fcc}_{\mathrm{slitless}}(\lambda)$ derived in Section 2.3.2 to calibrate the stellar spectra in the slitless mode after matching with DEIMOS CCDs. For the longslit mode flux calibration, we use the $\mathrm{Fcc}'_{\mathrm{longslit}}(\lambda)$ irrespective of the DEIMOS CCD (Section 2.3.4).

We derive synthetic r-band spectroscopic magnitudes from the absolute flux calibrated spectra for our test star (Pickles & Depagne 2010). The average flux density within a photometric filter is given by,

$$< f_r(\lambda) >= \frac{\int \lambda S_r(\lambda) f(\lambda) d\lambda}{\int \lambda S_r(\lambda) d\lambda}, \tag{2.4}$$

where $S_r(\lambda)$ is the filter response curve and $f(\lambda)$ is the flux calibrated spectrum. We convert the average flux density to an AB magnitude using,

$$m_r = -2.5 \log \left(\frac{\lambda_p^2 < f_r(\lambda) >}{c} \right) - 48.60, \tag{2.5}$$

where λ_p is the pivot-wavelength of the filter given by:

$$\lambda_p = \sqrt{\frac{\int \lambda S_r(\lambda) d\lambda}{\int S_r(\lambda) d\lambda / \lambda}}. \tag{2.6}$$

We use the Sloan r-band filter response curve to derive the spectroscopic magnitude because the APASS R-band magnitudes are given in terms of the Sloan r-band magnitudes (Doi et al. 2010).

Figure 2.5 shows the estimated spectroscopic magnitudes for the test star HIP 23694 from our two flux calibration schemes. The mean spectroscopic magnitude is consistent with the absolute magnitude of the standard star within 1-sigma errors, suggesting systematic consistency in the absolute flux measurement from both modes of flux calibration. We estimate a scatter of $\Delta m_{\mathrm{longslit}} = 0.11$ in the spectroscopic magnitude of the test star in the longslit mode of flux calibration, whereas in the slitless flux calibration mode the scatter is only $\Delta m_{\mathrm{slitless}} = 0.03$.

The longslit mode flux calibration results in a 10.7% precision in the absolute flux density across DEIMOS CCDs as opposed to the 2.8% precision in the slitless mode ($\Delta m = -2.5 \log(f_1/f_2)$). Thus, by correcting for the differential profile of DEIMOS CCDs, we improve the flux calibration accuracy from $\sim 11\%$ to 3% for a test star of magnitude $m_r = 9.72$.

2.4.2 Using galaxy spectra

To estimate the accuracy of flux calibration on faint targets, we apply our calibration schemes on a set of test galaxies. Our test galaxies are selected from the observation of the galaxy cluster RXJ1532+3021 because a single DEIMOS slitmask simultaneously observes nearly 100 objects. We apply the following criteria:

(i) a strong continuum ($f_\lambda > 10^{-17}$erg/s/cm^{-2}/Å) to minimises statistical error in the spectrometric magnitude measurements,

(ii) a lack of absorption and emission features to reduce spectral feature contamination, and

(iii) a similar number of galaxies from each of the DEIMOS CCD.

We compare the synthetic spectroscopic magnitudes (Equation (2.4) and (2.5)) with the SDSS photometric magnitudes to estimate the statistical and systematic uncertainties in our flux calibration schemes. DEIMOS spectra covers full spectral range for the SDSS $r-$ and $i-$bands, hence we calculate synthetic spectroscopic $r-$ and $i-$band magnitudes for our test galaxies. Slit-losses for spatially resolved sources are accounted by applying a correction factor to each test galaxy (Section 2.3.4).

For faint targets, the slitless mode does not improve the accuracy of flux calibration significantly. We quantify the flux calibration accuracy and precision by estimating the mean and the 1-sigma error in the offset between the synthetic spectroscopic magnitudes and the SDSS photometric bands. The systematic offset in synthetic spectroscopic magnitudes for both photometric bands and both modes of flux calibration is statistically zero (Figure 2.6). We do not observe any systematic offsets suggesting that slit-loss factors were estimated correctly (Section 2.3.4). The slitless flux calibration mode results in slight increase in the 1-sigma scatter in the $\Delta m \sim 0.25$ (Figure 2.6: left panel) compared to the longslit mode $\Delta m \sim 0.20$ (Figure 2.6: right panel). The accuracy of absolute flux calibration is $\sim 20\%$ in both calibration modes.

2.5 Conclusions

We quantify the statistical and systematic errors associated with DEIMOS flux calibration. In this paper, we investigate two techniques of flux calibration for DEIMOS/Keck-II: the slitless mode, where we derive a separate flux calibration curve for each DEIMOS CCD, and the longslit mode where a single flux calibration curve is used for all CCDs. We use the spectrophotometric standard G191B2B ($m_{\rm V} = 11.74$) to flux calibrate the data.

We conclude following from this exercise:

- Various CCDs of DEIMOS have slightly different sensitivity curves, with relative differences as large as 10% and wavelength dependent (Figure 2.4).

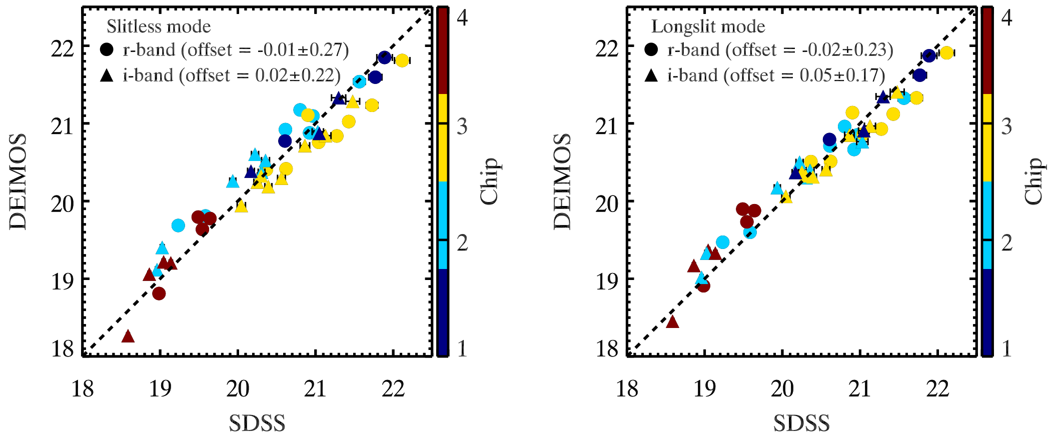

Figure 2.6: Comparison between the synthetic spectroscopic magnitude and the SDSS photometric magnitude in $r-$band (black dots) and $i-$band (red triangles). The data points in the left panel were calibrated using the slitless mode whereas the data points in right panel were calibrated using the longslit mode. Each data point is colour coded based on its location on the DEIMOS CCD. The dashed line is where $x = y$.

- The precision in the absolute flux density of the star HIP 23649 ($m_r = 9.72$) improves from 11% to 3% after accounting for the differential sensitivity of DEIMOS CCDs.
- The flux calibration accuracy for faint targets ($m_r \sim 21.0$) with DEIMOS is $\sim$ 20% for both modes of flux calibration in our test case. The slitless mode result in slightly enhanced calibration error compared to the longslit mode for faint targets.

Our work demonstrates that the flux calibration technique for DEIMOS should be chosen based on the average brightness of the targets. The slitless calibration mode is recommended for bright targets ($m_r < 10.0$). However, for faint targets a single calibration curve from the longslit mode is sufficient to achieve an absolute flux calibration accuracy of 20%. For faint targets the low S/N is the limiting source of errors rather than the differential CCD sensitivity. This implication is not surprising but has never been quantified before. In this paper, we report limitations and provide a quantitative reference for the flux calibration of DEIMOS.

This work is based on data obtained at the W. M. Keck Observatory. We are grateful to the Keck Observatory staff for assistance with our observations, especially Jim Lyke, Marc Kassis and Luca Rizzi. We thank Prof. Micheal Cooper, for his help with spec2d pipeline. L. Kewley gratefully acknowledges the support of an ARC Future Fellowship and ARC Discovery Project DP130103925. The authors wish to recognize and acknowledge the very significant cultural role and reverence that the summit of Mauna Kea has always had within the indigenous Hawaiian community. We are most fortunate to have the opportunity to conduct observations from this mountain.

Chapter 3

Cluster-scale abundance gradient for star-forming cluster galaxies

Context and Contribution

This chapter is originally published as *Radial Distribution Of ISM Gas-phase Metallicity In CLASH Clusters at $z \sim 0.35$: A New Outlook On Environmental Impact On Galaxy Evolution*, **A. Gupta, T. Yuan, K. Tran, D. Martizzi, L. Kewley, 2016, The Astrophysical Journal, 831, 104. This chapter is included in the thesis as a representation of my contribution showing the existence of a negative cluster-scale abundance gradient for star-forming cluster galaxies. I planned and conducted the observations, and reduced and analysed the data presented in this paper. The whole paper was written by myself with suggestions provided by co-authors.**

3.1 Introduction

Understanding the effect of cluster environment on galaxy formation and evolution is a central topic in extragalactic astronomy. A galaxy falling into the dense environment of a galaxy cluster experiences many high-speed tidal encounters with the cluster members and the cluster potential, leading to the removal of gas and disk destabilization (galaxy harassment, Moore et al. 1996). At the same time, the hot intra-cluster medium (ICM) interacts with the interstellar medium (ISM) of the galaxy and strips off its gas reservoir through ram pressure (ram pressure stripping, Gunn & Gott 1972; Dressler & Gunn 1983; Gavazzi et al. 1995). The galaxy loses a large fraction of the halo gas as it moves through the cluster, resulting in a gradual decline of star formation as it slowly runs out of fuel (strangulation, Larson et al. 1980). Additionally, if the dynamical friction time is sufficiently short, the galaxy will ultimately reach the cluster center and merge with the central brightest cluster galaxy (BCG; galactic cannibalism, Ostriker & Tremaine 1975; Hausman & Ostriker 1978; De Lucia & Blaizot 2007). All of the above processes are directly associated with the mass and ICM gas distribution (e.g., Gunn & Gott 1972; Dressler 1980;

De Lucia & Blaizot 2007; Bialas et al. 2015). Although the functional form of the density profile of the cluster is universal (e.g., Navarro et al. 1997; Huss et al. 1999), the exact structure of the local mass and ICM gas density depends on the dynamical state of the cluster (Dressler & Shectman 1988; Serna & Gerbal 1996; Adami et al. 2005).

Gas-phase metallicity provides a fossil record of the formation history of galaxies, modulated by galactic-scale gas flows. Metallicity can trace the impact of mass and environment on galaxy evolution. The mass-metallicity relation in the local universe has minimal dependence on environment as shown by most observations and simulations in local field and cluster galaxies (Tremonti et al. 2004; Mouhcine et al. 2007; Ellison et al. 2009; Davé et al. 2011; Scudder et al. 2012; Hughes et al. 2013). Cluster galaxies are shown to have slightly enhanced metallicity with respect to field galaxies at a fixed stellar mass (~ 0.04 dex), but the enhanced metallicity is driven by the local over-density instead of the large-scale cluster environment (Ellison et al. 2009).

More recent studies such as Peng & Maiolino (2014) find a stronger correlation of metallicity with environmental over-density in the local the Sloan Digital Sky Survey (SDSS) galaxies. Darvish et al. (2015a) found that galaxies in the filamentary structure at $z \sim 0.5$ have ~ 0.15 dex higher metallicity than their counterpart field galaxies. In high density environments such as inner regions of the galaxy clusters, the gas phase metallicity is higher by $0.08 - 0.20$ dex than counterpart field galaxies (Mouhcine et al. 2007). Studies at higher redshift ($z \sim 2$) are inconclusive about the environmental dependence of metallicity (e.g., Kacprzak et al. 2015; Tran et al. 2015; Valentino et al. 2015; Shimakawa et al. 2015b). Most studies on the environmental dependence of mass-metallicity relation select field versus cluster galaxies, but the local environment density depends on the cluster-centric distance, thus complicating the dependence of metallicity on cluster environment.

Galaxy properties such as color, morphology and luminosity show a strong dependence on the density (or cluster-centric distance) in galaxy clusters. The morphology-density relation shows that the elliptical galaxy fraction is higher in the cluster core than the cluster outskirts (e.g., Dressler 1980; Houghton 2015). Similarly, the environmental dependence of the luminosity function shows that the most luminous (or most massive) galaxies exist in the densest parts of the universe, i.e., the cores of galaxy groups and clusters (Davis et al. 1988; Zandivarez & Martínez 2011). In addition, the red galaxy fraction decreases with cluster-centric distance (Martínez et al. 2008; Ribeiro et al. 2013), implying an increasing star formation rate with cluster-centric distance. Simulations of galaxy clusters can reproduce the color distribution of cluster members by assuming a decreasing star formation rate after galaxies enter the cluster (Balogh et al. 2000). A recent study by Maier et al. (2016) finds a higher fraction of metal rich galaxies in the accreted region of the galaxy cluster than galaxies in the infalling region. However, there is no comprehensive study on the radial dependence of cluster member metallicities.

The radial metallicity distribution can constrain the mass assembly of galaxy clusters and the effect of cluster environment on individual cluster galaxy evolution. Both simulations and X-ray observations find that the X-ray plasma in galaxy clusters have higher metallicities in the cluster core than at larger cluster radius (De Grandi & Molendi 2001; Hlavacek-Larrondo et al. 2013), representing the excess average star formation in the cluster core. The observed negative radial gradients in ICM metallicity are often used as a constraint in galaxy cluster simulations (e.g., Kapferer et al. 2007; Cora et al. 2008; Rasia et al. 2015; Martizzi et al. 2016). Recent simulations by Martizzi et al. (2016) show that the ICM metallicities can be explained by a simple "regulator" model of stellar yield and gas accretion. Martizzi et al. (2016); Rasia et al. (2015) also find a mild correlation between stellar metallicity and cluster-centric distance, with X-ray luminous (cool-core) clusters exhibiting steeper metallicity gradients than non-cool core clusters. These results imply that the chemical evolution of individual cluster galaxies is intimately linked with the local ICM properties of the cluster. Observations of the ISM gas-phase metallicity in galaxies as a function of the ICM density (or cluster-centric distance), therefore provide new insights into the interplay between cluster galaxies and the cluster environment.

We present the first observations of the radial distribution of global ISM metallicity of star-forming galaxies in galaxy clusters. This work is based on optical spectra obtained with the DEIMOS spectrograph on Keck II telescope. The large field of view (FOV) of the DEIMOS spectrograph allows the observation of cluster members to large distances ($r \sim 2 \times r_{vir}$) as compared to the small central region probed by X-ray observations (< 200 kpc). We investigate the global metallicity of star-forming galaxies as a function of radial distance in two X-ray luminous clusters, MACS1115+0129 and RXJ1532+3021 at $z \sim 0.35$, and compare our observations with the Rhapsody-G simulations from Martizzi et al. (2016).

We organize this paper as follows. In Section 3.2, we describe the cluster sample selection, observations, data reduction and the derived quantities including the metallicity diagnostics. The main results of this paper are presented in Section 3.3. In Section 3.4, we discuss the possible mechanisms responsible for the origin of a cluster scale metallicity gradient. Throughout this work, we assume a standard ΛCDM cosmology with $h = 0.696$, $\Omega_\Lambda = 0.714$ and $\Omega_M = 0.286$ (Hinshaw et al. 2013).

3.2 Observations and data reduction

3.2.1 Cluster Sample Selection

The data used in this paper are part of our Gravitationally Lensed-galaxies Observed With-Adaptive Optics (GLOW-AO) survey. For the GLOW-AO survey the galaxy clusters were selected from the Cluster Lensing And Supernova survey with Hubble (CLASH, Postman et al. 2012) clusters. Our GLOW-AO survey was designed to

Table 3.1: X-ray and optically derived properties of galaxy cluster sample

Cluster	z[a]	kT[b] (keV)	L_{Bol}[b] (10^{44} erg s^{-1})	$r^c_{\rm vir}$ (Mpc/h)	$M^c_{\rm vir}$ ($10^{15}M_\odot/h$)	$c^c_{\rm vir}$	σ^d_{cl} (km/s)	$M^d_{\rm vel}$ ($10^{15}M_\odot/h$)
MACS1115+0129	0.352	8.0 ± 0.4	21.1 ± 0.4	1.78	1.13 ± 0.10	2.9 ± 0.9	960 ± 147	1.91 ± 0.61
RXJ1532+3021	0.362	5.5 ± 0.4	20.5 ± 0.9	1.47	0.64 ± 0.09	3.8 ± 1.7	1487 ± 213	3.78 ± 0.73

Notes.
[a] Redshift derived from SDSS spectra of central BCG.
[b] kT is the temperature and L_{Bol} is the total luminosity derived from the X-ray data (Postman et al. 2012).
[c] $r_{\rm vir}$ is the virial radius, $M_{\rm vir}$ is the total halo mass at the virial radius, and $c_{\rm vir}$ is concentration parameter at the virial radius of the cluster derived by combining the strong and weak lensing observations (Merten et al. 2015).
[d] σ_{cl} is the radial velocity dispersion from our observations and $M_{\rm vel}$ is the halo mass estimated from the velocity dispersion.

detect lensed galaxies in the redshift range of $0.8 < z < 1.6$ that can be observed with adaptive optics. The CLASH galaxy clusters were originally selected from a sample of X-ray bright clusters based on their gravitational lensing strength. The GLOW-AO survey is optimized for lensed galaxies to be followed up with AO observations using the OSIRIS instrument at the Keck I telescope. We, therefore select clusters that have at least one bright star ($R_{\rm AB} < 18.0$) within a radius of $60''$ from the central bright cluster galaxy (BCG). In order to perform a comprehensive analysis of the effect of cluster environment on the abundance gradient, we choose galaxy clusters with at least 15 cluster members. This restricted our cluster sample to 2 out of the 8 observed galaxy clusters, MACS1115+0129 and RXJ1532+3021.

MACS1115+01 (Ebeling et al. 1998) and RXJ1532+30 (Ebeling et al. 2010) are massive clusters with $M > 10^{14}M_\odot$ (Postman et al. 2012). Table 3.1 lists the derived physical and observational parameters for the selected clusters. X-ray morphology maps for both clusters exhibit minimal disturbances, highlighting the dynamically relaxed nature of the clusters (Allen et al. 2007). However, radio mini-halos were found around the central ~200 kpc of RXJ1532+30, suggesting a possible dynamical disturbance in the central region of this cluster (Kale et al. 2013). No radio disturbance is found in MACS1115+01. The non-uniform large scale temperature distribution from X-ray observations of RXJ1532+30 suggests a past minor merger with a cooler sub-cluster (Hlavacek-Larrondo et al. 2013). Spectroscopic data for MACS1115+01 and RXJ1532+30 are very limited. Our optical spectra provide important data to investigate dynamical structures of the clusters through the velocity and metallicity distributions of cluster members.

3.2.2 Local comparison field sample

We derive our field comparison sample from the Sloan Digital Sky Survey (SDSS) for our mass-metallicity study (AdelmanMcCarthy et al. 2006). Despite being at a lower redshift, SDSS galaxies were used as the comparison sample as there is little evolution in the ISM properties of field galaxies between $z \sim 0.1$ to $z \sim$

Table 3.2: Priority list of targets

Objects	Priorities[a]
Lensed candidates	1000
Photometric z ($0.8 < z < 2.5$)	900
NGS galaxies	800
LGS galaxies	600
Galaxies ($R_{\rm AB} < 24.0$)	100

Notes:
Objects is the category of galaxies in the DEIMOS mask.
[a] Priorities is the number we assign by us while designing the DEIMOS mask.

0.35 (Kewley et al. 2013a). The stellar mass of SDSS galaxies was calculated from the SDSS photometry using the stellar templates from Bruzual & Charlot (2003) with Chabrier IMF (Chabrier 2003)[1]. The SDSS sample was selected to match the stellar mass range of our DEIMOS cluster data ($8.5 < \log(\mathrm{M}_*/\mathrm{M}_\odot) < 11.0$). To ensure $> 20\%$ aperture coverage for each galaxy and minimize the aperture effects (Kewley et al. 2005), we select SDSS galaxies within the redshift range of $0.05 < z < 0.10$. We select star-forming galaxies using the standard BPT diagram criteria described in Kewley et al. (2006). We further restrict the SDSS sample by selecting galaxies with $S/N > 5.0$ for the following emission lines, [OII]$\lambda\lambda 3726, 3729$, H$\beta\lambda 4861$, [OIII]$\lambda\lambda 4959, 5007$, [NII]$\lambda\lambda 6549, 6583$, H$\alpha\lambda 6563$ and [SII]$\lambda\lambda 6717, 6731$. The final sample of 55759 SDSS star-forming galaxies is used to compare with our cluster member sample.

3.2.3 Mask Design and Spectroscopy

The mask for MACS1115+01 was designed using publicly available Hubble Space Telescope (HST) images and photometric catalogs. Because the HST images cover only the central $\sim 120''$, we used Canada France Hawaii Telescope (CFHT) color images offered by C. J. Ma and Harald Ebeling (private communication) to select potential cluster members and background lensed galaxies. Lensed galaxy candidates were identified based on their morphology, position around central brightest cluster galaxy (BCG) and photometry. The highest priority slits were placed on candidate lensed galaxies and cluster members. The subsequent priorities of objects are listed in Table 3.2. Galaxies that can be observed with a natural guide star, i.e. a $R_{\rm AB} < 18.0$ star at a separation of $< 30''$ radius from the central BCG, are referred to as NGS. Similarly, galaxies referred as LGS can be observed with laser guide star, i.e. they have a star with $R_{\rm AB} < 18.0$ within a $60''$ radius. The remainder of the mask was filled with galaxies with $R_{\rm AB} < 24$. We designed each mask to have at least two stars with $R_{\rm AB} < 15$ on each side to ensure proper mask alignment.

[1] See `http://wwwmpa.mpa-garching.mpg.de/SDSS/DR7/Data/stellarmass.html`

Table 3.3: Observation summery

Targets	α(J2000)	δ(J2000)	Mask	airmass	Exposure time
MACSJ1115+01	11:15:52.1[a]	+01:29:53[a]	Multi-slit	1.06	$3 \times 1200s$
RXJ1532+30	15:32:53.8[a]	+30:20:58[a]	Multi-slit	1.09	$5 \times 1200s$
G191-B2B[b]	05:05:30.6	+52:49:54	Long-slit	1.19	45s
G191-B2B[c]	05:05:30.6	+52:49:54	no mask (CCD1)	1.19	15s
G191-B2B[c]	05:05:30.6	+52:49:54	no mask (CCD2)	1.19	15s
G191-B2B[c]	05:05:30.6	+52:49:54	no mask (CCD3)	1.19	15s
G191-B2B[c]	05:05:30.6	+52:49:54	no mask (CCD4)	1.19	15s

Notes:
[a] Coordinates of the BCG centroid (J2000)
[b] Used for telluric correction and longslit mode flux calibration
[c] Slitless mode flux calibration
Seeing $\sim 0.8''$

3.2.4 DEIMOS Observations

All observations were conducted with the DEIMOS spectrograph (Faber et al. 2003) at the KECK II telescope on UTC February 24, 2014. We used the 600ZD grating at $\lambda_c = 7500$Å and the OG550 filter. Our spectra had a wavelength coverage of 5500 Å − 9800 Å with a dispersion of 0.65 Å/pixel. The slit width for all observations was $1''$ and all slits had a constant position angle the same as the DEIMOS mask. A DA-type white dwarf star G191-B2B (Rauch et al. 2013) of $V_{\mathrm{AB}} = 11.74$ was used for flux calibration. We developed a robust technique to flux calibrate the DEIMOS observations by deriving the separate sensitivity function of individual CCDs of the spectrograph (Chapter 2). Absolute flux calibrated spectrum of the star G191-B2B was obtained from the ESO archive[2]. Table 3.3 summarizes the observations for the data used in this paper. The mask for MACS1115+01 was observed with a total integration time of 1 hour split into 3×20 minutes exposures to eliminate cosmic rays. The mask for RXJ1532+30 had a total integration time of 1 hour 40 minutes (5×20 minutes exposures). Each mask had ≈ 130 slits and the average seeing during observations was $\sim 0.8''$.

3.2.5 Data reduction

We reduced the data in two stages. First, we used the publicly available spec2d pipeline written by Michael Cooper (Cooper et al. 2011) to reduce the raw data. The pipeline generates 2D slit-spectra after performing the bias removal, flat-fielding, slit-tilt correction, cosmic ray rejection and wavelength calibration. Secondly, we used our IDL-based code (Chapter 2) to correct for atmospheric absorption, derive instrument sensitivity and flux calibrate the 2D slit spectra.

[2] See `http://www.eso.org/sci/observing/tools/standards/spectra.html`

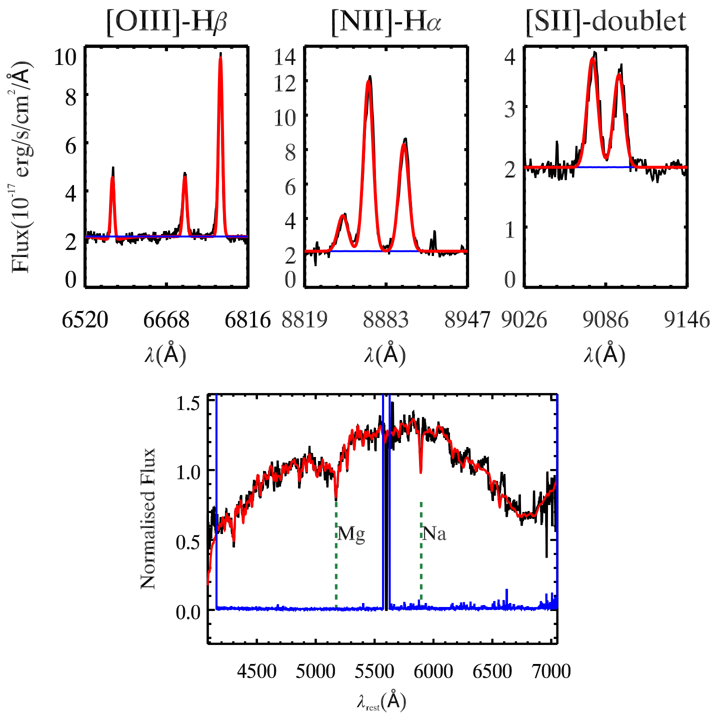

Figure 3.1: DEIMOS spectra of cluster members in MACS1115+01. **Left panel:** An example of emission line galaxy spectrum at $z = 0.351$ and line-profile fittings in following order, [OIII]-Hβ, [NII]-Hα and [SII]. **Right panel:** An example of absorption line galaxy spectrum (black curve) with the pPXF fit (red curve) at $z = 0.347$. Blue curve shows the error spectrum supplied to the pPXF.

For telluric correction, we used the long-slit mode observation of the standard star G191-B2B, which is a DA type white dwarf star with an effective temperature of 60920K (Rauch et al. 2013). The atmospheric absorption profile convolved with instrument response curve was derived from stellar 1D spectrum after removing the intrinsic stellar absorption features and the underlying blackbody profile. All 2D spectra were divided by the derived sensitivity curve to correct for instrument sensitivity and telluric absorption.

We used the process described in Chapter 2 to flux calibrate 2D slit spectra from DEIMOS. The 1D-spectrum of the observed objects was extracted by fitting a Gaussian curve to the spatial slit profile and integrating the flux within the full width half maxima (FWHM). For galaxies where Gaussian fitting was not possible, we used FWHM calculated from the point spread function (PSF) of alignment stars on the DEIMOS mask to extract 1D spectrum.

3.2.6 Emission line fitting

We visually inspected all 2D slit spectra to estimate an initial redshift by identifying strong emission lines like [OII] $\lambda\lambda 3726, 3729$, H$\beta$, [OIII]$\lambda 4959, 5007$, H$\alpha$, [NII]$\lambda 6583$. Multiple Gaussian profiles were fit to emission lines simultaneously depending on their separation in wavelength. For the [OII] doublet $\lambda\lambda3726, 3729$, we fit a double Gaussian with 5 free parameters: redshift, flux peak-1, flux peak-2, line width and continuum level. A similar double Gaussian function was used for the [SII]$\lambda\lambda6717, 6731$ doublet. We fit a triple Gaussian to the [NII], Hα emission lines using 6 free parameters: redshift, flux-Hα, flux-[NII], line width-Hα, line width-[NII] and continuum level. The ratio of [NII]$\lambda6548$ to [NII]$\lambda6583$ was constrained to its theoretical value of 1/3 (Osterbrock 1989). The [OIII], Hβ emission line group was simultaneously fit using 4 Gaussians with 8 free parameters: redshift, flux-[OIII], width-[OIII], flux-Hβ, width-Hβ, flux absorption-Hβ, width absorption-Hβ and continuum level. Figure 3.1: left panel presents the example of emission line fits for cluster member in MACS1115+01 at $z = 0.351$. We identified 73 redshifts out of 127 slits in the redshift range of $0.05 < z < 1.13$ for the mask MACS1115+01. For RXJ1532+30, 83 redshifts were identified out of the 139 slits in the redshift range of $0.036 < z < 0.992$.

We identify and fit emission lines to 14 and 21 cluster members in MACS1115+01 and RXJ1532+30 respectively. Ratios of major emission lines, [OIII]/Hβ, [NII]/Hα, [SII]/Hα and [NII]/[SII] for the cluster members in MACS1115+01 and RXJ1532+30 are given in Table 3.4 and Table 3.5 respectively.

3.2.7 Absorption line galaxies

Spectra with no apparent emission lines but with a strong continuum were visually inspected for Naλ 5872, Mgλ 5174 and Balmer absorption lines, to estimate an initial redshift. We performed single stellar population fitting using the penalised pixel-fitting routine (pPXF, Cappellari & Emsellem 2004) to fine-tune the redshifts of the absorption line galaxies. We used the MILES stellar population models (Vazdekis et al. 2010) to best match the spectral resolution of our observations. The sky-lines and bad pixels were masked before fitting the continuum models. The right panel in Figure 3.1 shows the example of fit from pPXF for a cluster member in MACS1115+01 at $z = 0.347$. Using pPXF, we calculated the redshift of 8 absorption line galaxies for MACS1115+01 (Table 3.6) and 15 galaxies for RXJ1532+30 (Table 3.7).

3.2.8 Active galatic nuclei (AGN) removal

Abundance calibrations using strong emission lines are only robust for star-forming galaxies. Therefore, we need to remove AGNs from our cluster member sample. Galaxies can be classified on the basis of their global energetics using optical strong emission line ratios such as [O III]/Hβ and [N II]/Hα (Baldwin et al. 1981, BPT). The hard ionizing radiation field from AGN increases the intensity of the metal ion forbidden lines (e.g., N^+, O^{++}) as compared to the hydrogen recombination lines. Kewley et al. (2001, hereafter Ke01) developed a theoretical "maximum starburst

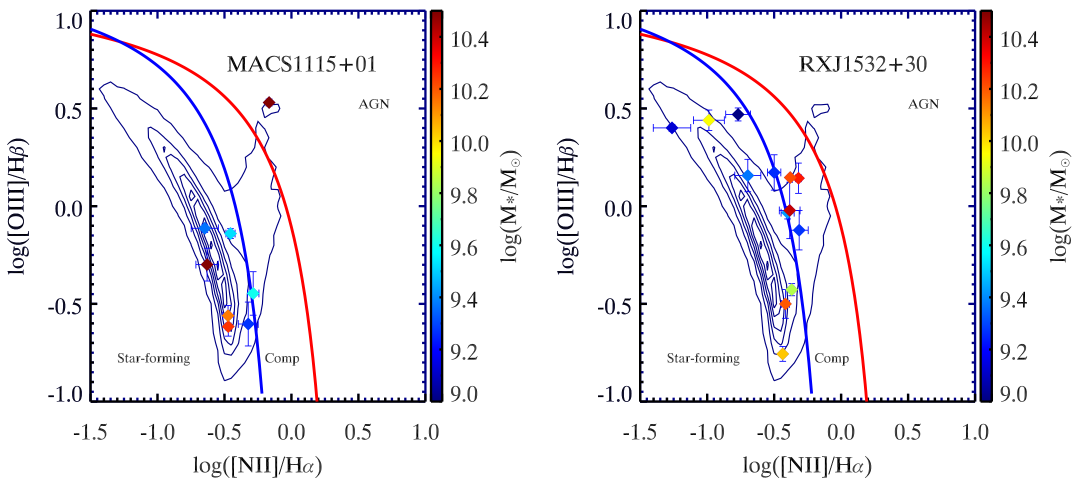

Figure 3.2: Optical BPT diagnostic diagrams for the observed cluster members for MACS1115+01 (left panel) and RXJ1532+30 (right panel). The data points in each panel are color coded with stellar mass ($\log(M_*/M_\odot)$). The red (Kewley et al. 2001) and blue (Kauffmann et al. 2003b) curves divide the galaxies into three subclasses i.e. star forming, composite and AGN. The blue contours show line ratios for the local comparison sample. AGN galaxies are removed to ensure star forming sample for the optical diagnostics.

line" on the BPT diagram using a combination of stellar population synthesis, photoionisation and shock models. An "empirical star-forming line" was developed by Kauffmann et al. (2003b, hereafter Kau03) using the SDSS data. Using Ke01 (red curve) and Kau03 (blue curve), we can separate galaxies into star-forming, composite and AGN groups on the [O III]/Hβ and [N II]/Hα BPT diagram (Figure 3.2). The AGN versus star-forming classification was developed for $z \sim 0$ galaxies. Because the redshift evolution between $z \sim 0$ and $z \sim 0.35$ is negligible on the BPT diagrams, the $z \sim 0$ classification can be used for our cluster sample at $z \sim 0.35$. Our results remain unchanged even if we use the new redshift dependent classification by Kewley et al. (2013a). For analysis of metallicity gradients, we use galaxies below the Ke01 line, thus incorporating both the star-forming and the composite galaxies.

3.2.9 Stellar mass

We derived the stellar mass from SDSS broad-band photometry (u, g, r, i, z) using the *Le Phare* package (Arnouts et al. 1999; Ilbert et al. 2006) with the stellar templates from Bruzual & Charlot (2003) and Chabrier IMF (Chabrier 2003). The stellar templates have seven exponentially decreasing star formation models (SFR $\propto e^{-t/\tau}$) with $\tau = 0.1, 0.3, 1, 2, 3, 5, 10, 15, 30$ Gyr and three metallicities. To correct for dust attenuation in stellar continuum, the Calzetti et al. (2000) models were used with $\mathrm{E(B-V)} = 0$ to 0.6. The stellar templates with stellar population ages from 0 to 13 Gyr were used. Throughout this paper, we have used the median of the generated mass distribution as the stellar mass of our galaxies. The typical error from *Le Phare* in the mass estimation from the SDSS photometry is 0.2 dex.

3.2.10 ISM parameters

We use a new theoretical calibration by Dopita et al. (2016) to derive the global metallicities for our selected cluster member galaxies. Direct measurement of the ISM metallicity requires observations of extremely weak auroral emission lines such as [OIII]λ4363, which is difficult for high redshift galaxies. Thus, the metallicity is often determined via theoretical and empirical calibrations based on strong emission lines such as Hα and [NII]. The strength of these emission lines depends on the ionization conditions in the galaxies i.e., ionization parameter and ISM pressure. The new calibration by Dopita et al. (2016) using the log([NII]/Hα) and log([NII]/[SII]) ratios is independent of ionization conditions and scales linearly with the oxygen abundance (a proxy for metallicity; $12 + \mathrm{Log(O/H)}$).

We use the Dopita et al. (2016) calibration given by:

$$12 + \log(\mathrm{O/H}) = 8.77 + \log([\mathrm{NII}]/[\mathrm{SII}]) + 0.264 \log([\mathrm{NII}]/\mathrm{H}\alpha), \tag{3.1}$$

to derive the metallicity for both our cluster galaxies and the local comparison sample. We require a signal to noise (S/N) of 3 for all necessary emission lines to derive the metallicity. Using an independent metallicity calibration such as the Pettini & Pagel (2004, N2) does not affect our results. We also determine the ionization properties of the cluster galaxies using [OIII]/Hβ and [NII]/Hα. We found no statistically significant relationship between the ionization state of the gas and cluster radius, given our small sample size.

3.3 Results

3.3.1 Cluster member identification

We identified cluster members based on the radial velocity of galaxies around the redshift of the central BCG. The peak of the redshift distribution for each mask coincides with the redshift of the central BCG of the respective clusters (Figure 3.3). We used an initial radial velocity cut of $\pm 10,000$ km/s and a further 2.5σ clip on the radial velocity with a basic outlier rejection.

We identified 22 cluster members for MACS1115+01, of which 14 are emission line galaxies. The radial velocity distribution of selected cluster members is represented by the blue bars in Figure 3.4. The normality in velocity dispersion has been used to characterize the dynamically relaxed state of a galaxy cluster (e.g., Yahil & Vidal 1977; Ribeiro et al. 2013). A one sided Kolmogorov–Smirnov (KS) test yields a

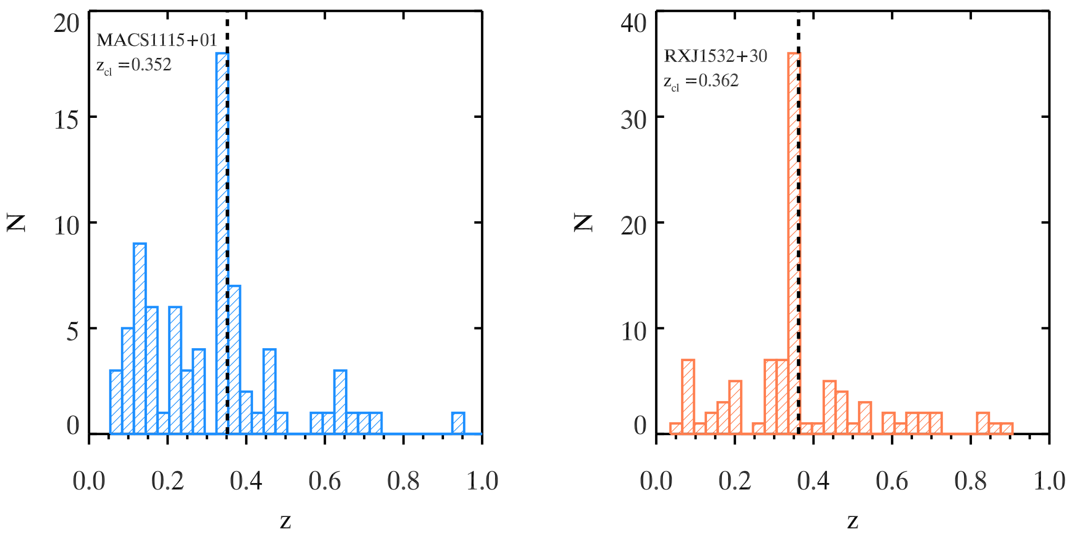

Figure 3.3: Redshift distribution of all objects observed on the DEIMOS mask. **Left panel:** MACS1115+01, and **right panel:** RXJ1532+30. The black line in each panel indicates the redshift of the clusters. The peak in histogram at the cluster redshifts clearly indicates detection of cluster members.

probability of 55% for the velocity distribution of MACS1115+01 to be drawn from the normal distribution, indicating the dynamically relaxed state of the galaxy clusters. The velocity dispersion for MACS1115+01 is $\sigma_{cl} = 960 \pm 147$ km/s. Assuming virialization, the total mass of MACS1115+01 is $M_{\rm vel} = 1.91 \pm 0.61 \times 10^{15}\ M_\odot/h$, which is within the 1σ error of the virial mass calculated from the gravitational lensing observations ($M_{\rm vir} = 1.13 \times 10^{15}\ M_\odot/h$, Merten et al. 2015, Table 3.1). We find no obvious dependence of the stellar mass of cluster member galaxies on the position around the cluster centre, for both emission line (Figure 3.5: left panel - diamonds) and absorption line (Figure 3.5: left panel - circles) systems.

For RXJ1532+30, we identify 36 cluster members, from which 21 are emission line galaxies. The cluster member mass of RXJ1532+30 also appears to be independent of the spatial position around the central BCG (Figure 3.5: right panel). For RXJ1532+30, the probability of the radial velocity distribution (Figure 3.4: red bars) to be drawn from a normal distribution is only 5% according to the KS-test. The observed velocity dispersion for RXJ1532+30 is $\sigma_{cl} = 1487 \pm 213$ km/s. Assuming a virialized state for the cluster RXJ1532+30, the total cluster mass estimated from the velocity dispersion would be $M_{\rm vel} = 3.78 \pm 0.73 \times 10^{15}\ M_\odot/h$, nearly 6 times the mass calculated from the gravitational lensing observations ($M_{\rm vir} = 0.64 \times 10^{15}\ M_\odot/h$, Merten et al. 2015, Table 3.1). We discuss the discrepancy in the mass estimation from the radial velocity dispersion and gravitational lensing in Section 3.4.1.

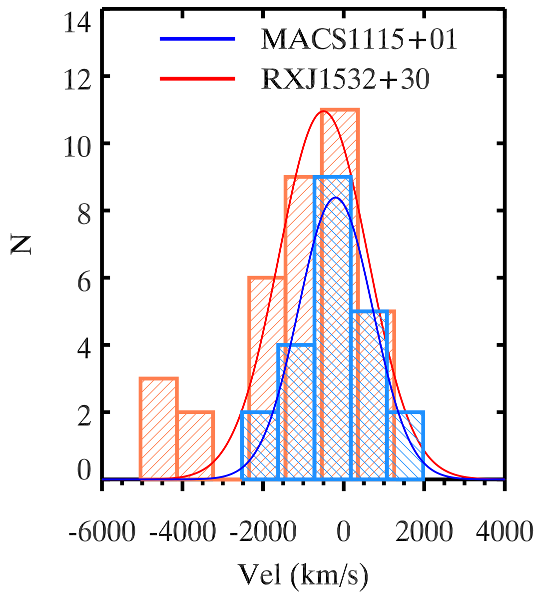

Figure 3.4: The radial velocity distribution of selected cluster members. The cluster members for MACS1115+01 are shown in blue and RXJ1532+30 in red. Solid lines indicates the Gaussian profiles of the velocity distribution clearly showing the different dynamical state of the two cluster.

3.3.2 Mass-metallicity relation (MZR)

In Figure 3.6, we show the MZR for the star forming cluster members in the two clusters (colored diamonds) and we compare the cluster MZR with the MZR for the local sample (contours). The metallicities of cluster members and SDSS sample were derived using the strong emission line diagnostics log([NII]/Hα) and log([NII]/[SII]) (See Section 3.2.10). The stellar mass derived from SDSS photometry (Section 3.2.9). After applying a S/N cut of 3 for the necessary emission lines, the metallicities could be for 12 and 16 cluster members for MACS1115+01 and RXJ1532+30 respectively.

Both clusters show a positive correlation between stellar mass and gas phase metallicity. The MZR for MACS1115+01 (Figure 3.6: left panel) has an offset of 0.2 dex to higher metallicity compared to the local field sample at a fixed mass. A double two-sided KS-test yields the probability of stellar mass and metallicity distribution of the cluster members and the local comparison sample to be derived from the same parent population as 28.9% and 0.03% respectively for MACS1115+01. Thus, the cluster members for MACS1115+01 show enhanced metallicity irrespective of the stellar mass, indicating the impact of cluster environment on the chemical evolution of galaxies.

The MZR for RXJ1532+30 (Figure 3.6: right panel) follows nearly the same distribution as the SDSS local comparison sample. The median offset in metallicity for RXJ1532+30 and the SDSS sample is within the errors of our observations. The KS-test probability of stellar mass and metallicity distribution of cluster members and the local comparison sample to be derived from the same parent population is 7.6% and 28.9% respectively. This implies that the mass-metallicity distribution of RXJ1532+30 and the local comparison sample are subsamples of the same parent population.

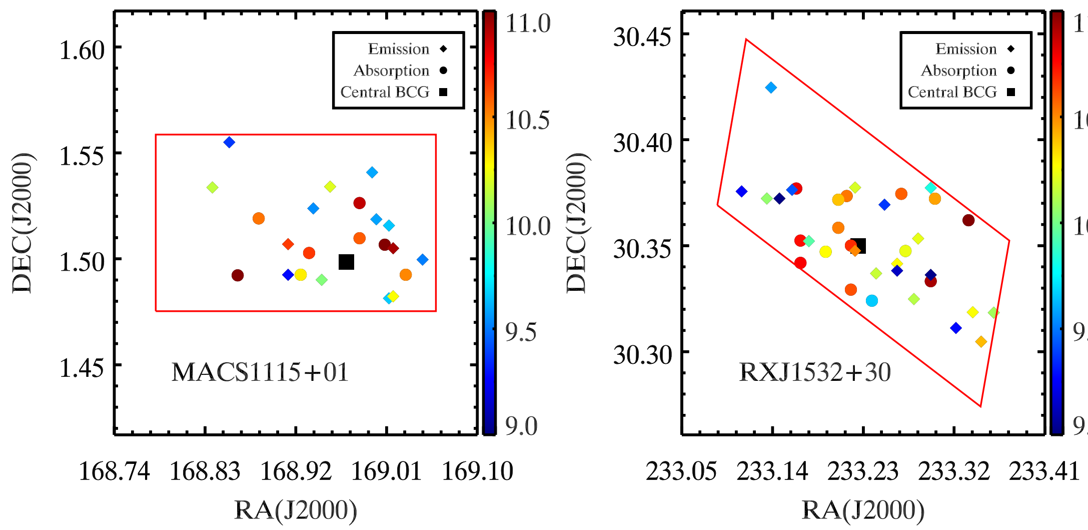

Figure 3.5: Spatial distribution of all cluster members with absorption line galaxies shown as circles and emission line galaxies shown as diamonds. **Left panel:** MACS1115+01, and **right panel:** RXJ1532+30. The square box in each panel shows the location of the central bright cluster galaxy (BCG) for each cluster. The large box in each panel represents the field of view of the DEIMOS mask used in our observations. The data is color coded with stellar mass ($\log(M_*/M_\odot)$) through out this paper. This figure does not show evidence of mass segregation for both clusters as the spatial location of cluster member is independent of their stellar mass.

The metallicity offset in MACS1115+01 (0.2 dex) is significantly higher than the metallicity offset observed in any previous studies of the MZR in the field versus cluster galaxy sample. In contrast, the MZR for RXJ1532+30 is consistent to the local comparison sample. Earlier studies of the MZR in cluster versus field galaxy samples constrain the environmental dependence to be around 0.04 dex (Ellison et al. 2009), significantly less than the metallicity offset observed for MACS1115+01. However, the cluster galaxy sample for studying the environmental dependence of MZR is usually collected from a large number of clusters without considering the internal variations among the galaxy clusters. Combining the metallicity data from multiple clusters might be responsible for the non-detection of a metallicity difference between field and cluster galaxies in previous studies. The extremely different MZR for MACS1115+01 and RXJ1532+30 in our observations supports this hypothesis.

3.3.3 The metallicity gradient in galaxy clusters

We observe an anti-correlation between the cluster member metallicity and projected distance for MACS1115+01 (Figure 3.7: left panel). Using the linear regression after a 2σ outlier rejection, the metallicity gradient for MACS1115+01 is -0.15 ± 0.08 dex/Mpc. The observed metallicity gradient is not driven by the stellar mass of galaxies because there is no preferential occurrence of high mass galaxies towards

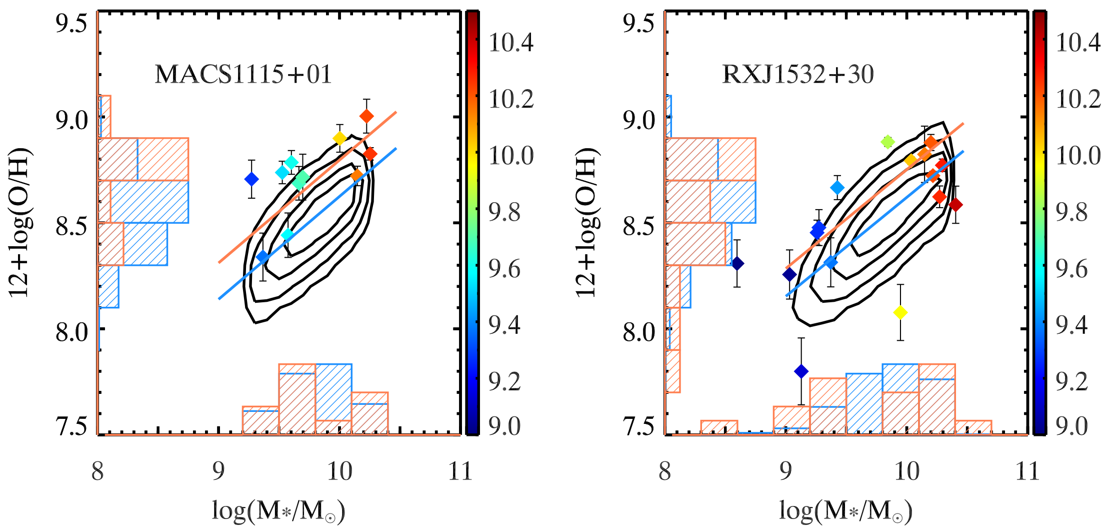

Figure 3.6: The mass-metallicity relation for cluster members. **Left panel:** MACS1115+01, and **right panel:** RXJ1532+30. The contours in each panel represents the MZR for the local comparison sample from SDSS (see Section 3.2.2). The red and blue histogram in each panel represents the mass and metallicity distribution of the cluster members and SDSS control sample respectively. The metallicity distribution for MACSJ1115+01 and the local comparison sample is clearly different.

the cluster centre. The Spearman rank correlation coefficient for MACS1115+01 is $\rho = -0.682$ with a significance of 0.021. Therefore, the Spearman rank probability of no correlation between the metallicity and the projected distance is 2.1% for MACS1115+01.

The metallicity versus projected distance distribution for RXJ1532+30 (Figure 3.7: right panel) is different from MACS1115+01. A slight negative gradient (-0.09 ± 0.12 dex/Mpc) was derived for RXJ1532+30 after a 2σ outlier rejection. The Spearman rank correlation coefficient for RXJ1532+30 is $\rho = -0.044$ with a significance of 0.87 i.e., the probability of no correlation between the metallicity and the projected distance is 87%. Thus, the metallicity gradient in RXJ1532+30 is statistically flat considering all observed cluster members.

Interestingly, the metallicity versus projected distance for RXJ1532+30 seems to show two branches. If we exclude the low-mass galaxies ($\log(M_*/M_\odot) < 9.5$), the linear regression after a 2-sigma rejection for the rest of the cluster members yields a negative metallicity gradient of -0.14 ± 0.05 dex/Mpc (Figure 3.8: dashed line; hereafter upper branch). Similar linear regression fitting for the low-mass galaxies ($\log(M_*/M_\odot) > 9.5$) yields a positive abundance gradient of 0.3 ± 0.2 dex/Mpc (Figure 3.8: dotted line; hereafter lower branch). We speculate that the lower-mass galaxies constituting the positive radial gradient are either interlopers or a group of in-plane mergers from a sub-cluster.

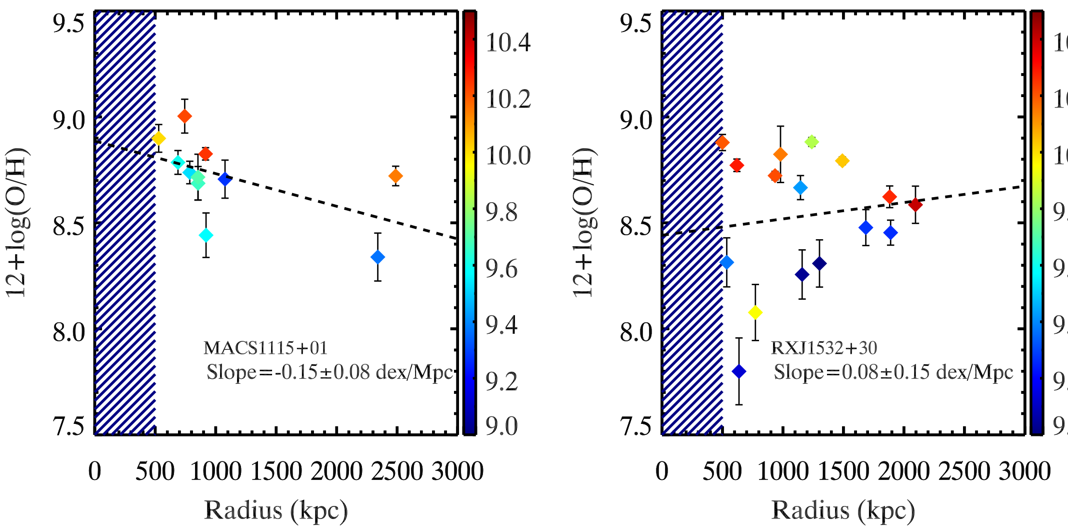

Figure 3.7: Radial metallicity distribution for individual clusters, where metallicity is derived using N2S2 method described in Section 3.2.10. **Left panel:** MACS1115+01, and **right panel:** RXJ1532+30. The dashed line in each figure is the best linear fit to the data. The slope and standard error in slope of the best-fitting line are labelled in each figure. The metallicity of cluster members in MACS1115+01 anti-correlates with the projected distance, whereas the radial metallicity distribution of RXJ1532+30 is bimodal that is collectively equivalent to a flat metallicity gradient.

3.4 Discussion

We present the first detections of negative radial gradients in the gas-phase metallicity of galaxies in cluster environment. We survey two CLASH clusters, MACS1115+01 and RXJ1532+30, with the DEIMOS/Keck-II detecting 22 and 36 cluster members for each respectively. The gas-phase metallicities are derived for a sample of 12 and 16 star-forming galaxies in MACS1115+01 and RXJ1532+30 respectively, using strong emission line diagnostics.

3.4.1 Gas-phase metallicity gradient and cluster dynamics

Even though MACS1115+01 and RXJ1532+30 are both massive clusters with $M_{\rm vir} \sim 10^{14}\ M_{\odot}/h$, the observed metallicity distribution is significantly different. The gas-phase metallicities of star-forming galaxies in MACS1115+01 exhibit an anti-correlation with projected distance, with a gradient of -0.15 ± 0.08 dex/Mpc (Figure 3.7: left panel), whereas the metallicity distribution of RXJ1532+30 with projected distance is suggestive of bimodal (Figure 3.7: right panel). In addition, the MZR of MACS1115+01 exhibits an elevated metallicity by 0.2 dex for cluster members as compared to the local SDSS sample (Figure 3.6: left panel). In contrast, the MZR of RXJ1532+30 is statistically similar to the local comparison sample (Figure 3.6: right panel).

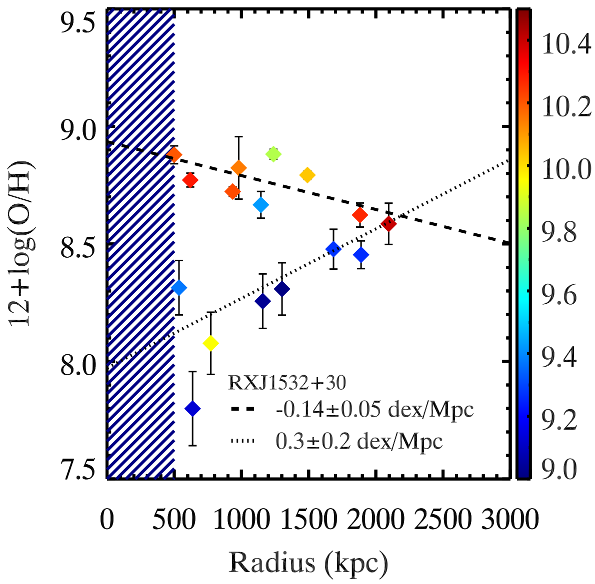

Figure 3.8: Bimodal metallicity distribution of RXJ1532+30 using a stellar mass cut of $\log(M_*/M_\odot) = 9.5$. The dashed line represents the best-fitting metallicity gradient line for galaxies with $\log(M_*/M_\odot) > 9.5$ (upper branch) and the dotted line gives the best-fitting metallicity gradient line for galaxies with $\log(M_*/M_\odot) < 9.5$ (lower branch). The figure shows a negative abundance gradient for high mass galaxies with slope similar to MACS1115+01 (Figure 3.7: left panel), whereas low mass galaxies show a positive abundance gradient.

Contrary to X-ray morphology studies that conclude the relaxed nature of both clusters (Allen et al. 2007), the redshift distribution from our study indicates that the two clusters have different dynamical states. A standard KS-test suggests the redshift distribution of RXJ1532+30 is non-Gaussian as opposed to the Gaussian redshift distribution of MACS1115+01. The comparison of virial mass estimated from the velocity dispersion measurement of our observations to the virial mass estimated from weak lensing also suggests differences in the dynamical state. From the velocity dispersion, we calculate the virial mass for MACSJ1115 to be $M_{\rm vel} = 1.91 \pm 0.61 \times 10^{15}\ M_\odot/h$, consistent with the lensing mass within the 1-sigma errors ($M_{\rm vir} = 1.13 \pm 0.1 \times 10^{15}\ M_\odot/h$, Merten et al. 2015). For RXJ1532, the estimated virial mass is $M_{\rm vel} = 3.78 \pm 0.73 \times 10^{15}\ M_\odot/h$ from velocity dispersions, about 6 times larger than the lensing mass ($M_{\rm vir} = 0.64 \pm 0.09 \times 10^{15}\ M_\odot/h$, Merten et al. 2015). In fact, the presence of radio mini-halos and the inhomogeneity in large scale X-ray temperature distributions in RXJ1532 also indicate possible unrelaxed dynamics (Kale et al. 2013; Hlavacek-Larrondo et al. 2013).

The two branches in the radial metallicity distribution of RXJ1532+30 could be the result of a minor merger with a cooler sub-cluster or a group of interloper galaxies. The upper branch ($\log(M_*/M_\odot) > 9.5$) cluster members of RXJ1532+30 exhibit a negative abundance gradient with a slope matching the metallicity gradient of MACS1115+01 (Figure 3.7, Figure 3.8). However, the lower branch galaxies ($\log(M_*/M_\odot) < 9.5$) exhibit a positive metallicity gradient.

The existence of low mass galaxies in a separate substructure is confirmed by a virial mass analysis. We measure a velocity dispersion of 773.6 ± 162.3 km s^{-1} for RXJ1532+30 after excluding the lower branch galaxies, which estimates the virial mass for RXJ1532+30 to be $M_{\rm vel} = 1.02 \pm 0.55 \times 10^{15}\ M_\odot/h$. The estimated virial mass after excluding the lower branch galaxies is consistent with the lensing mass within 1-sigma errors, suggesting that the low-mass galaxies belong to a separate

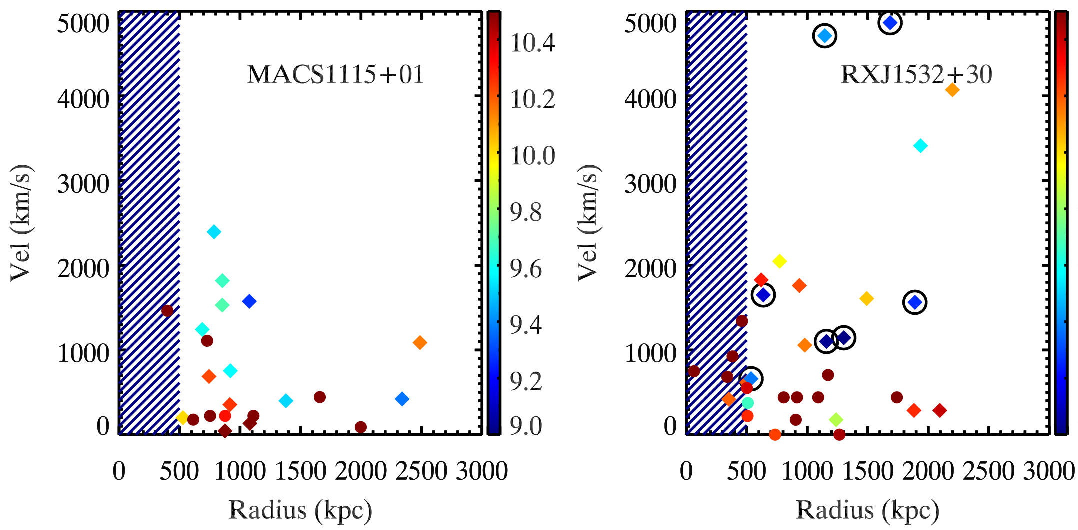

Figure 3.9: Projected phase space diagram for the observed clusters. **Left panel:** MACS1115+01, and **right panel:** RXJ1532+30. Emission line galaxies are represented as diamonds and absorption line galaxies as circles. The data is color coded with stellar mass. There is inconclusive evidence of mass segregation from the projected phase space diagram for the two clusters. The open circles in the right panel represent galaxies that belong to the lower branch ($log(M_*/M_\odot < 9.5)$) in Figure 3.8. The random positions of the merging sub-cluster galaxies suggests an in-plane merger.

substructure and/or are a population of interloper galaxies. The possibility of a minor merger between a cooler sub-cluster and RXJ1532+30 was first suggested by Hlavacek-Larrondo et al. (2013) based on the spatial asymmetry in the large scale X-ray temperature of RXJ1532+30. We hypothesize that the upper branch galaxies ($\log(M_*/M_\odot) > 9.5$) belong to the dynamically relaxed massive component of the cluster RXJ1532+30, with a metallicity gradient similar to the dynamically relaxed cluster MACS1115+01. The lower branch galaxies belonging to a merging cooler sub-cluster and/or interloper galaxies that are misidentified as cluster galaxies due to projection effects. To understand whether projection effects play a role in our metallicity gradient measurements, we compare our results with the metallicity gradient from Rhapsody-G simulations.

3.4.2 Comparison with Rhapsody-G simulations

We compare our data to the Rhapsody-G simulations performed with the Ramses (Teyssier 2002) adaptive mesh refinement (AMR) code (Hahn et al. 2015, Martizzi et al. 2016, Wu et al. 2015) because the mass rage of simulated clusters matches the mass of observed clusters. The Rhapsody-G sample currently includes cosmological hydrodynamical zoom-in simulations of 10 massive galaxy clusters of virial mass $M_{\rm vir} \sim 6 \times 10^{14}$ $\rm M_\odot/h$. The simulations assume standard ΛCDM cosmology with $\Omega_{\rm M} = 0.25$, $\Omega_\Lambda = 0.75$, $\Omega_{\rm b} = 0.045$, $h = 0.7$. The different cosmological parameters of the observations and simulations will introduce an offset in distance measurement up to 20 kpc. In the RHAPSODY-G terminology, the simulations used for our comparison have 'R4K resolution': dark matter particle mass $m_{\rm dm} = 8.22 \times 10^8 h^{-1}$ M$_\odot$; initial baryonic matter resolution element $m_{\rm b} = m_{\rm dm}\Omega_{\rm b}/(\Omega_{\rm M} - \Omega_{\rm b}) = 1.80 \times 10^8 h^{-1}$ M$_\odot$; maximum resolution reached in these simulations is $\Delta x = 3.8h^{-1}$ kpc (in physical units). Gas cooling, star formation, metal enrichment from supernovae, supernova feedback and AGN feedback are included in RHAPSODY-G.

These simulations successfully reproduce the mass distribution, baryonic abundances, cool core/non-cool core dichotomy and SZ properties of observed clusters (Hahn et al. 2015). We select simulated cluster member galaxies with star formation rate greater than $1M_\odot$ yr^{-1} to best compare with the observations of metallicity gradient. Note that the absolute metallicity of the simulations is lower than that of observations, therefore we can not directly compare the absolute simulated and observed metallicities. This offset may be related to the observational metallicity calibration used (e.g., Kewley & Ellison 2008). We do not compare the impact of environment on the mass-metallicity relation in simulations because there are no field galaxies in the simulations. However, we can investigate signatures of relative metallicities, such as metallicity gradients, in the Rhapsody-G simulations. We note that a direct comparison with the simulations of Taylor & Kobayashi (2015), who use a sophisticated supernova feedback and chemical evolution prescription, was not possible because their current simulations do not contain relaxed clusters on the mass scales of interest here.

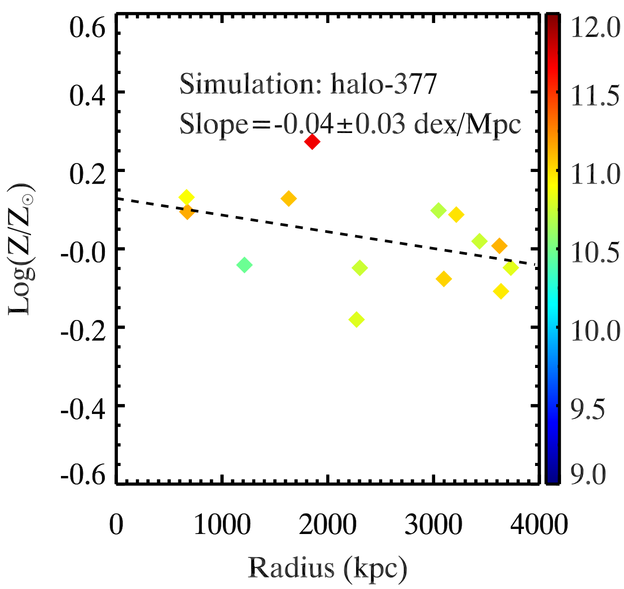

Figure 3.10: Radial distribution of star-forming galaxies in halo-377 in the Rhapsody-G simulations. We have used projected distance instead of radial distance and colour coded the simulated galaxies according to their stellar mass for a direct comparison with the observations. The simulations show mass-independent negative metallicity gradient similar to the metallicity gradient in our observations.

We select the simulated galaxy cluster, which has the closest value of concentration to the observations. The concentration is a proxy for the age and dynamical state of the cluster (Dutton & Macciò 2014). Therefore, we use the concentration parameter of the simulations ($c_{\rm vir} = r_{\rm vir}/r_s$, where the $r_{\rm vir}$ is the virial radial and r_s is the scale radius of the density profile of the cluster) to match with the observations. Both

MACS1115+01 and RXJ1532+30 have similar concentration parameters resulting in the selection of the halo-377 for both clusters. Observationally, the similar concentration of MACS1115+01 and RXJ1532+30 does not fully rule out the dynamically unrelaxed nature of RXJ1532+30 because concentration is not strongly affected by minor merger events.

The comparison simulated cluster exhibits a negative abundance gradient of -0.04 ± 0.03 dex/Mpc (Figure 3.10). The negative metallicity gradient in the simulation is not driven by the stellar mass in accordance with the mass-independent abundance gradient of our observations. The existence of a negative metallicity gradient in simulations confirms that the observed metallicity gradient is not a projection effect, but the shallower slope may be related to a lack of information about the projection axis of the observed clusters. To compare the metallicity gradients in the simulations with the observations, we have projected the simulated galaxies onto the plane of the sky. However, for a non-spherically symmetric halo the projected distance depends upon the axis of projection onto the sky, thus affecting the observed metallicity gradient.

3.4.3 Origin of cluster-scale metallicity gradient

Truncation of galactic-disk

Galaxies moving through the dense environment of galaxy clusters experience high speed interactions with other cluster members, leading to destabilization of the outer disk (galaxy harassment, Moore et al. 1996). In addition, the gas component of a galaxy experiences a ram pressure due to the hot ICM, leading to the removal of cold gas in the outer disk of the galaxies (ram pressure stripping, Gunn & Gott 1972; Dressler & Gunn 1983; Gavazzi et al. 1995). In combination, the galaxy harassment and ram pressure stripping result in truncation of the outer galactic-disk as the galaxy falls into the cluster environment. Metallicity measurements via strong emission lines in high redshift galaxies are biased towards the high surface brightness regions, thus the truncation of the outer disk of galaxy biases the metallicity measurements to the inner metal-rich galactic-disk (e.g., Yuan et al. 2013b; Genel 2016). Therefore, as the galaxy falls into the galaxy cluster, a consecutive decrease in the galactic-disk size as a result of the loss of outer-disk due to ram pressure stripping or galaxy harassment, would result in successive high metallicity measurements in spatially non-resolved observations. This effect might play a role in causing the observed negative abundance gradient in the global metallicity of star-forming cluster members.

Morphological changes in the galaxy as a function of radial distance are a direct consequence of the galactic-disk destabilization/truncation due to galaxy harassment and/or ram pressure stripping. Unfortunately, the existing imaging data from CFHT and SDSS is not deep enough to observe these morphological changes, and HST data only spans the inner $\sim$300 kpc of the cluster. Thus, we require deeper imaging data in the outskirts of galaxy clusters to observe the morphological changes in star-forming galaxies with radial distance. Separating the effect of ram pressure and galaxy harassment is impossible with the current sample, as both galaxy clusters in our current sample are X-ray luminous. Future metallicity gradient observations with a broader sample of X-ray luminous (ram pressure dominant) and the X-ray non-luminous (galaxy harassment dominant) clusters can help to distinguish the relative role of ram-pressure stripping and galaxy harassment. Finally, in order to understand the effect of disk truncation on metallicity gradients, deep imaging and spatially resolved spectroscopic observations are required.

Self-enrichment via strangulation

In addition to disk truncation due to ram pressure stripping or galaxy harassment, the ICM also strips the galaxy of the loosely bound hot/warm halo gas (fuel for future star formation). Depriving the galaxy of a fresh supply of gas results in a gradual decline in star formation as the galaxy consumes its existing cold gas reservoir (strangulation, Larson et al. 1980). The dilution from the inflowing pristine gas in the strangulation mode does not exist, which results in self-enrichment of the galaxy as it goes through successive cycles of star formation. Assuming the infall time-scale for galaxies in inner region of the cluster is greater than the infall time-scale for galaxies in the outskirts, the star-forming galaxies in the inner regions, which have undergone more cycles of star formation would be more metal rich compared to galaxies in outskirts. Thus, preferential self-enrichment of galaxies in the inner regions of the cluster as compared to the galaxies in the outskirts can also generate the observed negative abundance gradient. In order to study the self enrichment of galaxies in galaxy clusters due to strangulation, we require integral field spectroscopy of a mass-matched sample of star-forming cluster galaxies at different radial distances in the cluster.

A direct consequence of self-enrichment of galaxies with radial distance would be mass segregation (i.e., preferential existence of high-mass galaxies in the inner cluster radii). However, we do not observe any obvious mass segregation in our data within our errors. The lack of an apparent mass segregation might be a a result of one or more of the following: (i) selective removal of massive quenched galaxies due to our sample bias of star-forming galaxies, (ii) mass growth as a function of infall time depends on the details of star formation history, such as mergers and ram pressure-enhanced star formation rate (Dressler & Gunn 1983; Gavazzi et al. 1995), (iii) projection effects leads to uncertainty in radial distance measurement (discussed in the subsequent subsection).

Systematic uncertainties due to projection effects

Observational measurements of the absolute cluster-centric distance are impossible, we only have information about the projected distance of a galaxy in a triaxial cluster halo. Adding the line of sight velocity of the galaxy relative to the galaxy cluster can reduce the uncertainty in the absolute cluster-centric distance measurement. A recent study by Maier et al. (2016) uses a projected phase space diagram to separate the cluster members into groups of accreted versus infalling galaxies. Adding the line of sight velocity via the projected phase-space diagram does not improve the signature of mass segregation in our observations (Figure 3.9). In addition, the low mass cluster members for RXJ1532+30 (lower branch on Figure 3.8) do not occupy any special location on the projected phase-space diagram (Figure 3.9: right panel), which we propose belongs to an in-plane merging cooler sub-cluster and/or interloper galaxies. However, even the projected phase-space diagram does not contain full 3 dimensional information about a galaxy cluster, and therefore, is insufficient to rule out the uncertainty in radial distance measurements.

Our current simulations do not have sufficient resolution to fully investigate the effects of disk truncation and self-enrichment on the origin of metallicity gradient. A more detailed analysis of galaxy tracking in simulations with high resolution is required to properly study the effects influencing the metallicity distribution in cluster satellites. Moreover, to fully understand the origin of cluster-scale metallicity gradients, we require metallicity gradient observations with a broader sample of a range of X-ray luminosity and dynamical state.

3.5 Conclusions

Using the multi-object optical spectrograph DEIMOS on the Keck II, we observe two CLASH clusters at $z \sim 0.35$, MACS1115+01 and RXJ1532+30. We analyse the gas-phase metallicity of star-forming galaxies derived from [NII]/[SII] and [NII]/Hα, as a function of projected distance from the central BCG. Our main results are:

- For MACS1115+01, we identify 22 (14 - emission line galaxies) cluster members corresponding to a velocity dispersion of $\sigma_{cl} = 960 \pm 147$ km/s. For RXJ1532+30, we identify 36 (21 - emission line galaxies) cluster members corresponding to a velocity dispersion of $\sigma_{cl} = 1487 \pm 213$ km/s. The virial mass estimated from the velocity dispersion is consistent with the gravitational lensing mass for MACS1115+01, but is 6 times more than the gravitational lensing mass for RXJ1532+30.

- We observe a significant metallicity enhancement in the star-forming galaxies in MACS1115+01 (0.2 dex) at a fixed stellar mass with respect to the local field galaxies. This is the largest metallicity enhancement observed for galaxy clusters to date. The mass-metallicity relation of RXJ1532+30 is consistent with the mass-metallicity relation of local field galaxies. The significant difference between mass-metallicity relation of MACS1115+01 and RXJ1532+30 show that the non-detection of metallicity enhancement in galaxy clusters in previous studies might be due to the combination of data from multiple clusters with different mass-metallicity relation.

- We present the first observation of a negative abundance gradient in the global metallicity of star-forming galaxies in galaxy clusters. We observe an abundance gradient of -0.15 ± 0.08 dex/Mpc for MACS1115+01 and a bimodal like metallicity distribution for RXJ1532+30. The upper branch galaxies in RXJ1532+30 also show a negative abundance gradient similar to MACS1115+01 (-0.14 ± 0.05 dex/Mpc). We speculate that the lower branch galaxies in RXJ1532+30 belong to a merging sub-cluster and/or are interloper galaxies. The velocity dispersion after excluding the lower branch galaxies is 773.6 ± 162.3 km/s, which gives a virial mass consistent with the lensing mass, suggesting a separate substructure for the lower branch galaxies.
- Star-forming galaxies in a simulated galaxy cluster also exhibit a negative abundance gradient, but with a shallower slope (-0.04 ± 0.03 dex/Mpc).
- We speculate that the origin of the negative abundance gradient in galaxy cluster could be due to (i) the truncation of outer galactic-disk due to galaxy harassment or ram pressure stripping, and (ii) the self-enrichment of galaxy after the ICM cuts off the gas supply for star formation.
- We hypothesize that a cluster-scale gradient in the ISM metallicity of galaxy members exists in clusters that (i) are X-ray luminous (i.e., have enough hot ICM), and (ii) in a relatively relaxed dynamical state (i.e., no significant recent merger).

In our follow-up work, we will use the Rhapsody-G simulations at significantly higher resolution to investigate the origin of metallicity gradients in galaxy clusters. To fully test our hypothesis, we require deep imaging and integral field spectroscopy for galaxy clusters with different X-ray and dynamical properties.

Acknowledgements

This work is based on data obtained at the W. M. Keck Observatory. We are grateful to the Keck Observatory staff for assistance with our observations, especially Jim Lyke, Marc Kassis and Luca Rizzi. The Observatory was made possible by the generous financial support of the W. M. Keck Foundation. A.G. acknowledges Prof. Micheal Cooper for his help with spec2d pipeline, I-Ting Ho for supplying the SDSS data and Melanie Kaasinen for her help in the editing of this paper. We thank C. J. Ma and Harald Ebeling for sharing their CFHT color images for the cluster RXJ1532+30. L.J.K. gratefully acknowledges the support of an ARC Future Fellowship and ARC Discovery Project DP130103925. K. Tran acknowledges support by the National Science Foundation under Grant #1410728. PT acknowledges support from a Discovery Project DP150104329 from the Australian Research Council . The authors wish to recognize and acknowledge the very significant cultural role and reverence that the summit of Mauna Kea has always had within the indigenous Hawaiian community. We are most fortunate to have the opportunity to conduct

observations from this mountain.

Table 3.4: Data table for observed emission line galaxies in MACS1115+01

objid	α (J2000)	δ (J2000)	z[a]	$\log(M_*/M_\odot)$[b]	log([OIII]/Hβ)[c]	log([NII]/Hα)[c]	log([SII]/Hα)[c]	log([NII]/[SII])[c]
1115020-0	11:15:46.29	+1:29:24.29	0.353	10	....±....	-0.39 ±0.05	-0.63±0.04	0.23±0.06
1115026-0	11:15:38.34	+1:30:24.95	0.351	10.64	0.53±0.02	-0.17±0.01	-0.44±0.01	0.28±0.01
1115042-0	11:15:44.46	+1:31:25.64	0.341	9.53	-0.14±0.03	-0.46±0.03	-0.54±0.04	0.09±0.05
1115069-0	11:16:3.18	+1:30:17.96	0.352	10.94	-0.3±0.08	-0.63±0.08	-0.12±0.02	-0.51±0.08
1115072-0	11:15:58.20	+1:32:26.88	0.349	9.57	....±....	-0.67 ±0.09	-0.52±0.04	-0.15±0.09
1115077-0	11:15:24.19	+1:33:18.07	0.354	9.37	-0.11±0.02	-0.65±0.1	-0.39±0.02	-0.26±0.1
1115088-0	11:16:10.62	+1:29:58.70	0.35	9.51	....±....	.... ±....	-0.04±0.17	....±....
1115096-0	11:15:38.65	+1:29:32.89	0.345	9.27	-0.6±0.11	-0.32 ±0.07	-0.34±0.05	0.02±0.08
1115103-0	11:15:48.81	+1:32:2.62	0.355	10.22	....±....	-0.28±0.07	-0.59±0.07	0.31±0.07
1115112-0	11:16:2.41	+1:28:52.93	0.36	9.66	....±....	-0.29 ±0.05	-0.28±0.06	-0.01±0.07
1115116-0	11:15:59.81	+1:31:7.18	0.346	9.6	-0.45±0.11	-0.29 ±0.04	-0.38±0.04	0.09±0.05
1115117-0	11:16:3.94	+1:28:56.28	0.35	10.25	-0.62±0.05	-0.47±0.02	-0.65±0.02	0.18±0.03
1115119-0	11:15:20.70	+1:32:1.28	0.357	10.15	-0.56±0.05	-0.47±0.04	-0.55±0.02	0.08±0.04
1115121-0	11:16:2.93	+1:30:56.52	0.345	9.7	....±....	-0.28 ±0.09	-0.31±0.07	0.02±0.1

Notes:

[a] z represents the best-fitting redshift to the DEIMOS spectra using the emission lines.

[b] $\log(M_*/M_\odot)$ is the stellar mass derived from the SDSS photometry (See Section 3.2.9).

[c] log([OIII]/Hβ), log([NII]/Hα), log([SII]/Hα) and log([NII]/[SII]) are the emission line ratios derived from the DEIMOS spectra (See Section 3.2.6).

Table 3.5: Data table for observed emission line galaxies in RXJ1532+30

objid	α (J2000)	δ (J2000)	z^a	$\log(M_*/M_\odot)^a$	$\log([OIII]/H\beta)^a$	$\log([NII]/H\alpha)^a$	$\log([SII]/H\alpha)^a$	$\log([NII]/[SII])^a$
1532008-1	15:32:53.99	+30:20:51.43	0.363	10.53	....±....	-0.23±0.04	....±....	....±....
1532017-0	15:32:42.42	+30:21:7.85	0.353	9.95	0.44±0.05	-0.99±0.12	-0.55±0.03	-0.43±0.12
1532023-0	15:33:7.43	+30:19:29.43	0.357	10.15	....±....	-0.22±0.11	-0.33±0.08	0.11±0.12
1532028-0	15:32:38.76	+30:22:34.93	0.341	9.43	-0.03±0.03	-0.4±0.05	-0.4±0.03	0±0.05
1532032-0	15:33:11.79	+30:20:10.42	0.357	9.03	....±....	-0.72±0.1	-0.4±0.03	-0.32±0.1
1532034-0	15:32:35.02	+30:22:20.21	0.357	8.6	0.47±0.03	-0.77 ±0.09	-0.51±0.05	-0.26±0.1
1532066-0	15:32:58.82	+30:20:12.95	0.364	10.19	....±....	....±....	....±....	....±....
1532074-0	15:32:53.85	+30:22:38.82	0.365	10.2	-0.5±0.07	-0.42±0.03	-0.63±0.02	0.22±0.03
1532080-0	15:33:0.78	+30:22:9.70	0.365	9.37	0.16±0.08	-0.7 ±0.1	-0.42±0.05	-0.27±0.1
1532086-0	15:33:3.55	+30:20:29.36	0.354	10.29	0.14±0.08	-0.32±0.02	-0.4±0.02	0.09±0.03
1532087-0	15:33:3.95	+30:20:17.59	0.355	9.13	0.4±0.02	-1.26 ±0.14	-0.62±0.01	-0.64±0.14
1532093-0	15:33:8.87	+30:21:12.13	0.354	10.22	0.15±0.01	-0.38±0.02	-0.43±0.01	0.05±0.02
1532098-0	15:33:11.63	+30:22:38.28	0.361	9.84	-0.43±0.03	-0.37±0.02	-0.58±0.01	0.21±0.02
1532102-0	15:32:32.41	+30:22:20.21	0.355	10.04	-0.76±0.04	-0.44±0.02	-0.57±0.01	0.14±0.02
1532110-0	15:33:17.70	+30:18:40.25	0.34	9.27	-0.12±0.1	-0.31 ±0.07	-0.1±0.06	-0.21±0.08
1532116-0	15:32:26.79	+30:22:32.27	0.355	9.26	0.17±0.09	-0.5 ±0.05	-0.32±0.03	-0.18±0.05
1532118-0	15:32:33.67	+30:25:28.70	0.347	9.57	0.5±0.04	.... ±....	-0.5±0.11	....±....
1532119-0	15:33:21.72	+30:19:7.00	0.361	10.27	....±....	-0.31±0.04	-0.25±0.04	-0.06±0.05
1532122-0	15:33:23.94	+30:18:17.03	0.361	10.4	-0.02±0.14	-0.38±0.08	-0.3±0.04	-0.08±0.08
1532125-0	15:33:26.90	+30:19:6.28	0.343	10.1	-0.56±0.05	....±....	....±....	....±....

Notes:
[a] Same as Table 3.4, but for galaxy cluster RXJ1532+30.

Table 3.6: Data table for observed absorption line galaxies in MACS1115+01

objid	α (J2000)	δ (J2000)	z^a	$\log(M_*/M_\odot)^b$
1115025	11:15:43.51	+1:30:9.94	0.347	10.66
1115043	11:15:31.53	+1:31:8.65	0.354	10.54
1115057	11:15:55.28	+1:30:34.99	0.359	10.59
1115064	11:15:55.62	+1:31:34.79	0.351	10.88
1115076	11:16:6.40	+1:29:32.96	0.351	10.5
1115098	11:15:41.69	+1:29:33	0.353	10.3
1115100	11:15:26.86	+1:29:31.96	0.352	11.06
1115115	11:16:1.60	+1:30:24.01	0.351	11.44

Notes:
[a] z represents the best-fitting redshift to the DEIMOS spectra using the absorption lines (See Section 3.2.7).
[b] $\log(M_*/M_\odot)$ is the stellar mass derived from the SDSS photometry (See Section 3.2.9).

Table 3.7: Data table for observed absorption line galaxies in RXJ1532+30

objid	α (J2000)	δ (J2000)	z^a	$\log(M_*/M_\odot)^a$
1532009	15:32:52.90	+30:21:0.25	0.359	10.69
1532012	15:32:49.90	+30:21:30.46	0.359	10.52
1532018	15:32:40.86	+30:21:8.72	0.361	10.74
1532019	15:32:40.66	+30:20:30.84	0.364	10.78
1532027	15:32:39.24	+30:22:37.16	0.36	10.8
1532031	15:33:11.13	+30:19:59.67	0.359	10.92
1532065	15:32:52.44	+30:19:45.37	0.358	10.61
1532069	15:32:51.11	+30:22:24.46	0.356	10.53
1532071	15:32:49.76	+30:22:18.12	0.359	10.39
1532075	15:32:46.03	+30:20:49.74	0.361	10.27
1532077	15:32:57.06	+30:19:26.58	0.364	9.66
1532088	15:33:5.65	+30:20:51.04	0.362	10.23
1532090	15:33:4.68	+30:22:28.13	0.36	10.59
1532100	15:33:12.61	+30:22:19.88	0.362	10.45
1532112	15:33:20.26	+30:21:43.27	0.36	11.07

Notes:
[a] Same as Table 3.6, but for galaxy cluster RXJ1532+30.

Chapter 4

Disk truncation via ram pressure stripping simulation using CALIFA galaxies

Context and Contribution

This chapter is originally published as *Survival of Massive Star-forming Galaxies in Cluster Cores Drives Gas-Phase Metallicity Gradients : The Effects of Ram Pressure Stripping*, **A. Gupta, T. Yuan, D. Martizzi, K. Tran, L. Kewley, 2017, The Astrophysical Journal, 842, 75. This chapter is included in the thesis as a representation of my contribution in understanding the physical origin of metallicity enhancement of star-forming cluster galaxies. I have developed the model and the conducted the scientific analysis presented in this paper. The whole paper was written by myself with suggestions provided by co-authors.**

4.1 Introduction

Understanding the link between internal properties of galaxies such as stellar mass, gas fraction, chemical abundance and the large-scale environment continues to be a rich area of research. Numerous studies have established that galaxy clusters have significantly larger fractions of elliptical and S0-type galaxies relative to the field galaxy populations (Dressler 1980; Poggianti et al. 1999; Van der Wel 2008). Galaxies in local galaxy clusters have lower star-formation rates and are deficient in both the molecular and atomic gas compared to field galaxies (Kauffmann et al. 2004; Balogh et al. 2004; Chung et al. 2009; Hughes & Cortese 2009; Cortese et al. 2011; Boselli et al. 2014a; Odekon et al. 2016; Brown et al. 2017a). The removal of the cold/hot gas reservoir for an infalling galaxy via ram pressure stripping (RPS; Gunn & Gott 1972) by the hot diffuse intracluster medium (ICM) can explain some of the differences between cluster and field galaxies such as lower gas fraction and lower star formation rates in cluster galaxies (Abramson et al. 2011; Chung et al.

2009; Boselli et al. 2014b).

The gas-phase metallicity of a galaxy is regulated by its star-formation history and galactic gas inflows/outflows. The interactions between the ICM and circum-galactic medium (IGM/CGM) can potentially affect the chemical evolution of cluster galaxies. Previous studies testing for environmental effects on chemical evolution have focused on measuring the stellar mass-metallicity relation (the MZ relation) variation with the local density. Observations of the MZ relation find minimal to negligible evidence of environmental influence (Cooper et al. 2008; Ellison et al. 2009; Scudder et al. 2012; Hughes et al. 2013; Pasquali et al. 2012; Peng & Maiolino 2014; Darvish et al. 2015a; Pilyugin et al. 2017b). For example, Ellison et al. (2009) and Pilyugin et al. (2017b) find that galaxies in high density environments have an enhanced metallicity of ~ 0.05 dex compared to field galaxies. However, both Ellison et al. (2009) and Pilyugin et al. (2017b) conclude that the metal enhancement depends more strongly on the local environment density than the large-scale environment density at redshift $z \sim 0$.

In Chapter 3, we measure the integrated gas-phase metallicities of cluster galaxies in MACS J1115+01 ($z = 0.35$) and study the correlation of the galaxy's metallicity with the projected cluster radius. Using this complementary method of testing for environmental effects on chemical evolution, we find that MACS J1115+01 has a negative cluster-scale metallicity gradient of -0.15 ± 0.08 dex/Mpc. In addition, cluster galaxies are on average ~ 0.20 dex more metal rich relative to field galaxies at a fixed stellar mass. Ellison et al. (2009) also observed that galaxies at small cluster-centric distance (< 0.3 R200) have a higher median metallicity than galaxies at larger cluster-centric distance (> 0.8 R200) by ~ 0.03 dex.

In Chapter 3, we propose two scenarios that can potentially explain the observed negative cluster-scale metallicity gradient: disk truncation due to ram pressure stripping and self-enrichment due to strangulation. Self enrichment leads to the physical enhancement in the metallicity of cluster galaxies, whereas disk truncation can introduce an observational bias in the integrated metallicity measured from a fixed aperture/slit.

Truncation of the gas disk by RPS can introduce a purely observationally-driven increase in the integrated gas-metallicities of an individual galaxy. RPS removes the gas reservoir outside the galactic radius where the gravitational restoring force is equal to the pressure gradient exerted on the infalling galaxy by the ICM (Gunn & Gott 1972). Stripping of gas from the outer-galactic disk instantaneously suppresses the star formation in the outer part of the galaxy. The metallicity measurements via optical strong emission lines are sensitive to star-forming regions of the galaxy. Thus, the integrated emission line flux for a cluster galaxy with truncated galactic disk will be biased towards the central metal-rich part of the galaxy, resulting in an enhanced integrated metallicity measurement. For example, Hughes et al. (2013) used disk truncation to explain the enhanced metallicity of cluster galaxies. They truncate the radial metallicity profile of NGC 4254 from Skillman et al. (1996) to 1.5 R_e and estimate a metallicity enhancement of 0.1 dex. However, their use of a fixed truncation radius does not consider the scatter in the truncation radius caused by different orbital parameters and physical properties of infalling galaxies. Thus a detailed model of RPS in a cluster environment is required to better understand how disk truncation increases the observed gas-metallicities of cluster members and potentially produces cluster-scale metallicity gradients as measured in Chapter 3.

In this paper, we focus on the effect of disk truncation on the integrated metallicity of cluster members. We simulate RPS in a galaxy cluster using the semi-analytic prescription by Luo et al. (2016) and Tecce et al. (2010). We select galaxies from the Calar Alto Legacy Integral Field Area (CALIFA) survey data release 3 (Sánchez et al. 2012) and distribute them uniformly in a galaxy cluster. We manually truncate the 3-dimensional (3D) datacubes of CALIFA galaxies based on the stripping radii calculated from the RPS model. We then conduct mock slit observations of the truncated CALIFA galaxies redshifted to $z = 0.35$ to estimate their integrated metallicity and compare with the cluster member metallicity gradients from Chapter 3. This paper is organized as follows. In Section 4.2, we describe the sample selection, the mock observation technique and the metallicity estimation. Our analytic model for the ram pressure stripping is described in Section 4.3. In Section 4.4, we describe the simulation of disk truncated cluster galaxies. In Section 4.5, we compare our results with observations. In Section 4.6, we discuss the strengths and weakness of our model. We assume a standard ΛCDM cosmology with $\Omega_{\rm M} = 0.30$, $\Omega_\Lambda = 0.70$, $\Omega_{\rm b} = 0.05$, $h = 0.7$.

4.2 Simulating Slit Spectroscopy of Cluster Galaxies at $z \sim 0.35$

Disk-truncation due to RPS of outer galactic-disk introduces an observational bias in the integrated metallicity measurements via slit spectroscopy. To determine if RPS can generate an increase in the gas-phase metallicity of cluster galaxies with decreasing cluster-centric distance, we first start with integral field unit (IFU) spectroscopy of nearby field galaxies. We can quantify the strength of the observational bias introduced in the integrated metallicity measurements by disk truncation after manually truncating the IFU datacubes using a semi-analytic model of RPS and conducting mock slit observations.

4.2.1 CALIFA: IFU spectroscopy at $z \sim 0$

We select our sample from the publicly available integral field data from the third data release (DR3) of the Calar Alto Legacy Integral Field Area (CALIFA) survey (Sánchez et al. 2012). We choose the CALIFA survey because it has better spatial resolution per galaxy compared to other ongoing local IFU surveys because of the

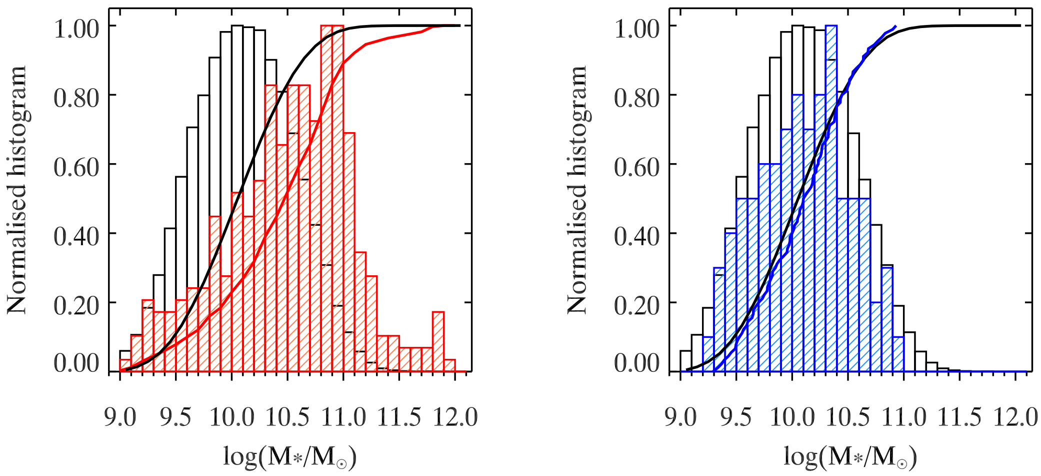

Figure 4.1: Left panel: The comparison of the mass distribution of the CALIFA DR3 (red histogram) with the SDSS DR7 (black histogram) sample. The CALIFA DR3 sample is biased towards the high stellar mass galaxies. The median stellar mass of full CALIFA DR3 sample is $10^{11} M_{\odot}$ whereas the median stellar mass of SDSS DR7 is $10^{10.5} M_{\odot}$. **Right panel:** The mass distribution of selected galaxies from the CALIFA sample (blue histogram) and SDSS DR7 (black histogram). We select CALIFA galaxies by using the stellar mass function of SDSS DR7 and populating it with CALIFA galaxies. The stellar mass distribution of our selected CALIFA galaxies and SDSS DR7 have a KS-test probability of 0.99 to be drawn from the same parent sample.

narrower redshift range ($\sim$ 400 pc Sánchez et al. 2016). Specific details of DR3 are presented in Sánchez et al. (2016) and Walcher et al. (2014). CALIFA DR3 contains about 650 galaxies in the redshift range of $0.005 < z < 0.03$. The primary CALIFA sample is derived from the Sloan Digital Sky Survey Data Release 7 (SDSS DR7; York et al. 2000; Abazajian et al. 2009). We select CALIFA galaxies with reliable stellar disk scale length provided in the Méndez-Abreu et al. (2017) catalog, restricting our sample to 280 galaxies. Each CALIFA datacube has a spatial field of view of $74'' \times 64''$ on a rectangular grid of $1''$. The average spatial resolution is $2.7''$, corresponding to an average physical resolution of $\sim$ 1 kpc. The CALIFA survey has two resolution modes, low-resolution (V500) and high-resolution (V1200), with a spectral coverages of $3740 - 7500$ Å and $3650 - 4840$ Å respectively. In this study, we will use the datacubes in the low-resolution mode (V500) that have a full width half maximum (FWHM) spectral resolution of 6 Å because we need a wide spectral coverage to measure the gas-phase metallicity.

To simulate disk truncation in cluster galaxies, we require a representative sample of field galaxies. The SDSS DR7 survey has $\sim$ 1 million galaxies and typically represents field galaxies. Using the stellar mass estimates by González Delgado et al. (2014) for the CALIFA sample, we find that the CALIFA DR3 sample is biased towards higher stellar mass relative to the full SDSS DR7 data (Figure 4.1: left panel). Stellar masses of the SDSS DR7 galaxies are taken from the MPA-JHU catalogs (**?**Brinchmann et al. 2004). We generate the stellar mass function of SDSS DR7 galaxies and populate it with CALIFA DR3 galaxies. Due to the limited number of galaxies with stellar masses below $10^{9.1} M_{\odot}$ in the CALIFA sample, we only match the stellar mass function at stellar mass $M_* > 10^{9.1} M_{\odot}$. The blue histogram in the right panel of Figure 4.1 shows the stellar mass distribution of the selected CALIFA galaxies. A two sided Kolmogorov–Smirnov (KS) test yield a probability of 99% for the stellar mass distribution of the SDSS sample and the selected CALIFA sample to be derived from the same parent population. Our final sample consists of 91 galaxies in the mass range of $9.29 < \log(\mathrm{M}_*/\mathrm{M}_{\odot}) < 10.93$.

4.2.2 Redshifting CALIFA to $z_{\mathrm{cl}} = 0.35$

The clusters observed in Chapter 3 were at a redshift of $z_{\mathrm{cl}} \sim 0.35$, whereas the average redshift of the selected CALIFA sample is $z \sim 0.013$. To redshift the CALIFA galaxies to $z_{\mathrm{cl}} \sim 0.35$, we use basic cosmology equations of angular size variation and surface brightness dimming. The mean redshift of the selected CALIFA sample is $z \sim 0.013$, leading to an average reduction in angular size and total flux by a factor of 0.054 and 9×10^{-4} respectively.

The observations in Chapter 3 were conducted with the DEIMOS spectrograph on the Keck-II telescope, which is a multi-slit spectrograph in seeing-limited conditions. To consider the effect of beam smearing in high-redshift observations, we match the spatial resolution of the redshifted datacubes with DEIMOS/Keck observations. The seeing of DEIMOS observations in Chapter 3 was $0.''8$, corresponding to a spatial

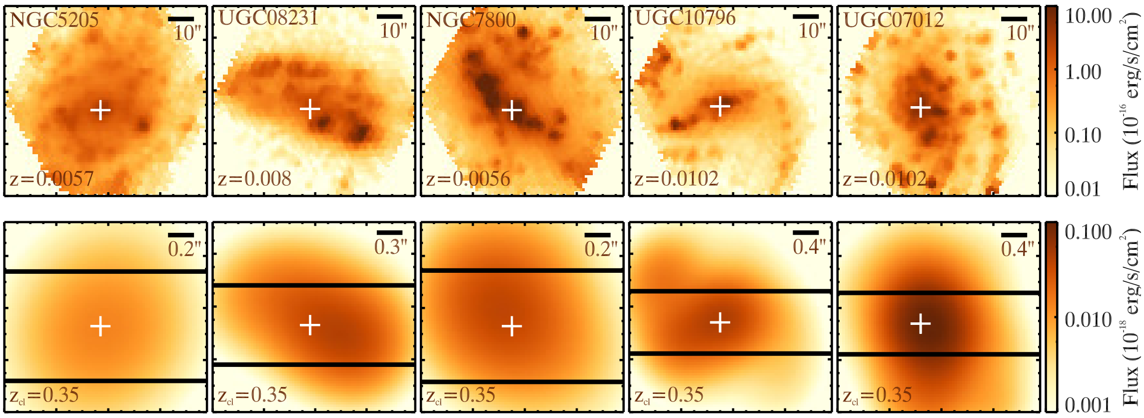

Figure 4.2: Top panel: Wavelength-collapsed Hα intensity map for a random sample of 5 galaxies from the stellar mass-matched CALIFA sample at $z \sim 0$. **Bottom panel:** Redshifted, wavelength-collapsed Hα intensity map at $z_{\rm cl} = 0.35$, with a seeing of $0.''8$. The thick black lines in each panel represent the $5'' \times 1''$ DEIMOS slit. The angular scale before and after redshifting is marked on the top right of each panel. To generate a 1D slit spectrum, we integrate the flux inside the slit for each wavelength slice in the datacube.

resolution of 3.952 kpc at $z_{\rm cl}$. The average seeing of CALIFA data is $2.''7$, with a spatial sampling of $1''$. We convolve each wavelength slice in redshifted datacubes with the point spread function (PSF) of DEIMOS observations. The top panel in Figure 4.2 shows the wavelength-collapsed Hα intensity maps for five randomly selected galaxies from the CALIFA sample and the corresponding Hα intensity map in the bottom panel after redshifting the datacubes to $z_{\rm cl} = 0.35$ and convolving with a seeing of $0.''8$.

4.2.3 Mock slit spectroscopy

We estimate the metallicity of cluster galaxies in Chapter 3 using integrated spectra from Keck/DEIMOS observations. To make a realistic comparison with the cluster-scale abundance gradient observed in Chapter 3, we conduct mock DEIMOS observations of the selected CALIFA galaxies after redshifting them to $z_{\rm cl}$. We generate a single slit spectrum for each redshifted IFU datacube by positioning a $5'' \times 1''$ DEIMOS slit on the galaxy center (Figure 4.2: bottom panel) and integrating the flux within the slit.

4.2.4 Emission line fitting and metallicity estimation

We extract emission line fluxes by following the same procedure as described in Chapter 3. In summary, we fit multiple Gaussian profiles to the 1D slit spectrum. The initial redshift is taken from the CALIFA catalog. We extract emission line fluxes of the following strong emission lines: Hβ, [O III] λ 4959, 5007, Hα, [N II] λ 6583 and [S II] $\lambda\lambda$ 6717, 6731. We remove galaxies with signal-to-noise (S/N) < 3 for any emission line. The AGN galaxies are removed using the [O III]/Hβ and [N II]/Hα diagram and the theoretical calibration of Kewley et al. (2001).

The metallicity of the star-forming galaxies is derived using the new diagnostic by Dopita et al. (2016) based on the ratio of [N II]/Hα and [N II]/[S II]. The metallicity calibration by Dopita et al. (2016) is given by:

$$12 + \log(\mathrm{O/H}) = 8.77 + \log([\mathrm{N\,II}]/[\mathrm{S\,II}]) + 0.264 \log([\mathrm{N\,II}]/\mathrm{H}\alpha). \tag{4.1}$$

Out of the 91 galaxies in the mass-selected CALIFA sample, we can reliably measure the metallicity of 61 galaxies after implementing the S/N cut and removing AGN galaxies.

4.3 Modeling the effect of disk truncation on gas metallicity measurements

RPS leads to many physical changes in properties of galaxies in the cluster environment. The atomic and molecular gas are observed trailing behind infalling cluster galaxies, giving direct evidence of RPS in cluster environments (Abramson et al. 2011; Boselli et al. 2014b; De Grandi et al. 2016). Observations of jellyfish galaxies show extreme stripping events where even the dense star-forming regions are stripped (Owen et al. 2006; Cortese et al. 2007; Owers et al. 2012; McPartland et al. 2016; Monroe et al. 2017). The gas removal by RPS can explain why cluster galaxies are HI deficient compared to field galaxies and why the HI deficiency increases as the galaxy moves closer to the cluster center (Hughes & Cortese 2009). The HI disk for field galaxies extends beyond the stellar disk (Cormier et al. 2016), whereas the HI disk in cluster galaxies is usually smaller or the same size as the stellar disk (Chung et al. 2009; Boselli et al. 2014b). The gas removal due to RPS in cluster environment has been used to explain the formation of S0-type galaxies in rich galaxy clusters (Sun et al. 2006; Aragón-Salamanca et al. 2006; Bedregal et al. 2011). The RPS leads to reduction in total mass and size of the gaseous disk of satellite galaxies, a phenomenon we refer to as disk truncation.

Disk galaxies in the local universe have a universal negative internal metallicity gradient (Zaritsky et al. 1994; Sánchez et al. 2014; Ho et al. 2015). If the progenitor of a cluster satellite exhibited a negative internal metallicity gradient before falling into the cluster, its integrated metallicity after disk truncation might be modified because of the removal of the low-metallicity outer portions of the disk. This picture is somewhat simplified because it ignores satellite-satellite interactions and residual star formation in the satellites that may lead to the production of more metals. However, in our treatment, we will neglect satellite-satellite interactions and residual star formation and focus on the zeroth order effect of disk truncation. Our goal is to test whether a simple disk-truncation model is sufficient to explain the metallicity gradient for cluster satellites observed in Chapter 3.

4.3.1 Our disk truncation model

Studying disk truncation in cluster satellites in its full complexity is very challenging because the simulation of full physics of multi-phase interstellar medium (ISM) and its hydrodynamical interaction with the ICM requires sophisticated modeling and can only be achieved using expensive, high-resolution numerical simulations (Roediger & Hensler 2005; Steinhauser et al. 2016; Luo et al. 2016). Hydrodynamical simulations use RPS of cold gas to obtain the star formation rate suppression and color transformation in simulated galaxy clusters (Abadi et al. 1999; Balogh et al. 2000; Roediger & Hensler 2005; Roediger & Brüggen 2007; Heß & Springel 2012; Steinhauser et al. 2016).

Semi-analytic models of galaxy formation usually have a simplistic description of the RPS of the gaseous component in cluster galaxies. Most semi-analytic models follow the prescription by Gunn & Gott (1972) for both the hot and the cold gas to calculate the stripping radius and the mass loss (McCarthy et al. 2008; Tecce et al. 2010; Guo et al. 2011; Luo et al. 2016). Comparisons with hydrodynamical simulations suggest that most semi-analytic models overestimate the strength of RPS, producing a larger fraction of red galaxies in clusters (Guo et al. 2013; Wang et al. 2014; Steinhauser et al. 2016). To test the effect of disk truncation on integrated metallicity observations, we choose a simplified approach that allows us to explicitly parameterize the physics of disk truncation.

We use an analytic model of disk truncation that depends only on the orbital parameters of the satellite galaxy and the local ICM properties. The procedure is summarized as follows:

1. We assume that the mass-selected CALIFA galaxies (for details see § 4.2.1) are uniformly distributed in the cluster as a first order initial condition for RPS to act upon (further discussed in Section 4.6.1). We assign the orbital velocity to each galaxy using the radial velocity distribution for MACS J1115+01 from Chapter 3 (§ 4.4).

2. We use the analytic model to calculate the stripping radius for each galaxy $r_{\rm strip}$ (§ 4.3.2). We then "simulate" disk truncation for all galaxies, i.e., we create mock datacubes for galaxies where the flux at radii $r > r_{\rm strip}$ is set to zero (§ 4.4).

3. We conduct mock DEIMOS observations of the simulated disks and measure the integrated metallicity for each simulated cluster galaxy (§ 4.2.4). We calculate the cluster-scale metallicity gradient following the same procedure of Chapter 3.

4. The above procedure generates one realisation of the disk truncation simulation with a cluster-scale metallicity gradient measurement. We repeat the above process until the mean cluster scale metallicity gradient converges (Figure 4.9), which requires a minimum of 150 realisations.

Our procedure does not take into account the full dynamics of the disk interaction with the ICM. We will discuss the ramifications of our assumptions in Section 6. Our current approach, albeit simple, provides a useful framework to understand the physical effect of disk truncation on the cluster galaxy metallicity.

4.3.2 An analytic model for the ram pressure stripping of cold gas

The multi-phase ISM of a galaxy can be divided into a cold and a hot component, primarily composed of the molecular hydrogen and neutral/ionized hydrogen, respectively. Explicit modeling of the stripping of different phases of the ISM requires properly designed numerical studies and is beyond the scope of our model. Both numerical simulations and observations show that the warmer neutral/ionized gas is stripped first (McCarthy et al. 2008; Chung et al. 2009; Boselli et al. 2014b; Steinhauser et al. 2016), but the stripping of the hot gas would not instantaneously affect the star formation rate because of large cooling timescales. The stripping of the cold gas component from the outer disk of a galaxy would quench the star formation almost immediately, resulting in the loss of emission line flux from the stripped part of the galactic disk. Thus, the stripping of the cold gas from the outer parts of the galactic disk will directly affect the average metallicity measurement for the satellite galaxy.

We follow the prescription by Gunn & Gott (1972) to model the RPS of gas in a galaxy falling into the ICM. We assume that the cold gas is fully stripped beyond the galacto-centric radius at which the internal gravitational potential energy density of the satellite galaxy is balanced by the RP. We define $r_{\rm strip}$ as the galactic radius at which the ISM pressure is equal to the RP exerted by the ICM. The RP experienced by a galaxy at a cluster-centric distance of R falling into the ICM with an orbital velocity of v_{orb} is

$$P_{r.p.} = \rho_{\rm ICM}(R) v_{orb}^2, \tag{4.2}$$

where $\rho_{\rm ICM}(R)$ is the ICM density at R. The cold gas is gravitationally bound with the ISM of the galaxy. Thus, the cold gas will be stripped only if the RP exceeds the gravitational restoring force due to the ISM ($P_{\rm ISM}$). We use Equation (4.3) given by Tecce et al. (2010) to determine the $P_{\rm ISM}$

$$P_{\rm ISM} = 2\pi G[\Sigma_*(r) + \Sigma_g(r)]\Sigma_g(r), \tag{4.3}$$

where $\Sigma_*(r)$ is the stellar surface mass density and $\Sigma_g(r)$ is the surface mass density of the gas. At $r_{\rm strip}$, $P_{r.p} = P_{\rm ISM}$, and thus we can equate (4.2) and (4.3), for a galaxy at a cluster-centric distance of R

$$2\pi G[\Sigma_*(r_{\rm strip}) + \Sigma_g(r_{\rm strip})]\Sigma_g(r_{\rm strip}) = \rho_{\rm ICM}(R)v_{orb}^2. \quad (4.4)$$

To estimate $r_{\rm strip}$ we need to model the stellar and gas surface mass density profile ($\Sigma_*(r)$ & $\Sigma_g(r)$), and the ICM density profile ($\rho_{\rm ICM}(R)$). The cold gas disk at radius $> r_{\rm strip}$ from the galactic center will be stripped away.

We assume that both the stellar disk and the gas disk follow exponential surface density profiles

$$\Sigma_*(r) = \Sigma_{*0}\exp(-r/r_*) \quad (4.5)$$

and

$$\Sigma_g(r) = \Sigma_{g0}\exp(-r/r_g), \quad (4.6)$$

where r_* and r_g are the scale length of stellar and gas disks, respectively, and Σ_{*0} and Σ_{g0} are the corresponding central surface mass density. The total stellar mass of an exponential surface density disk is given by $M_* = 2\pi r_*^2\Sigma_{*0}$ and the total gas mass is $M_g = 2\pi r_g^2\Sigma_{g0}$. We assume the same scale length for both the stellar and the cold gas disk, i.e., $r_* = r_g$, which is corroborated by the spatially resolved observations of the molecular gas for local field galaxies (Bigiel & Blitz 2012; Cormier et al. 2016). The ratio of central surface mass density of the gas and the stellar disk is equal to the molecular gas fraction (M_g/M_*) of the galaxy,

$$\frac{\Sigma_{g0}}{\Sigma_{*0}} = \frac{M_g}{M_*} = f_{gas}. \quad (4.7)$$

The molecular gas fraction for local field galaxies depends weakly on the stellar mass and has a typical value of $f_{gas} = 0.1$ (Boselli et al. 2014a). Thus, for a complete model of the gas and stellar surface density profiles, we only require the total stellar mass M_* (obtained from the CALIFA catalogs) and the scale length of stellar disk r_*. We use Méndez-Abreu et al. (2017) catalog to obtain r_* for CALIFA DR3 galaxies.

We evaluate the RP stripping radius ($r_{\rm strip}$) in Equation (4.4), using the modelled stellar and gas surface density profile (Equation (4.5) to (4.7)) as

$$r_{strip} = -\frac{r_*}{2}\ln\left[\frac{\rho_{\rm ICM}(R)v_{orb}^2}{2\pi G\Sigma_{*0}^2 f_{gas}(1+f_{gas})}\right]. \quad (4.8)$$

The modelled stripping radius ($r_{\rm strip}$) depends weakly on the ICM density ($\rho_{\rm ICM}$) and the orbital velocity (v_{orb}^2) of the satellite galaxy. A similar model of RPS has been used in various semi-analytic models of galaxy evolution (De Lucia et al. 2004; Tecce et al. 2010; Guo et al. 2011).

Different models can be used to generate the ICM density profile ($\rho_{\rm ICM}$) of the cluster. We use the Makino et al. (1998) model to generate the ICM density profile of MACS J1115+01. According to Makino et al. (1998), if the dark matter halo of the cluster follows the Navarro, Frenk and White (NFW; Navarro et al. 1997) density profile,

$$\rho_{DM}(R) = \frac{\rho_s}{(R/R_s)(1+R/R_s)^2}, \tag{4.9}$$

where ρ_s and R_s are the scale density and scale length; then the ICM density is given by:

$$\rho_{\rm ICM}(R) = \rho_{g0} e^{-B} \left(1 + \frac{R}{R_s}\right)^{(BR_s/R)}, \tag{4.10}$$

where ρ_{g0} is the central gas density and B is the ratio of the gravitational energy to the kinetic energy. In this formalism, B is given by:

$$B = \frac{4\pi G \mu m_p \rho_s R_s^2}{kT_X}, \tag{4.11}$$

where μ is the mean particle weight, m_p is the proton mass and T_X is the temperature of the hot ICM gas. The central gas density (ρ_{g0}) is given by,

$$\begin{aligned}\rho_{g0} = & \frac{f_g \Omega_b \rho_s}{\Omega_m} e^B \left[\ln(1+c) - \frac{c}{1+c}\right] \\ & \times \left[\int_0^c x^2 (1+x)^{B/x} dx\right]^{-1},\end{aligned} \tag{4.12}$$

again taken from Makino et al. (1998), where f_g is the ratio of the gas mass to the total baryonic fraction in the cluster and c is the concentration parameter given by the ratio of the virial radius to the scale length. Observationally, f_g ranges from $0.7 - 0.9$ (Gonzalez et al. 2013). We adopt $f_g = 0.8$. Thus, we require only four parameters, ρ_s (scale density of NFW profile), R_s (scale length of NFW profile), kT_X (X-ray temperature) and c (concentration parameter) to determine the density profile of the hot ICM. To compare with the cluster-scale metallicity gradient observations for MACS J1115+01, we use the cluster parameters for MACS J1115+01 provided by Merten et al. (2015) to model the density profile of ICM ($\rho_s = 0.61 \times 10^{15}\ h^2 M_\odot \mathrm{Mpc}^{-3}$, $R_s = 0.62$ Mpc/h, $kT_X = 8.0$ keV and $c = 2.9$). Thus, the stripping radius in Equation (4.8) only depends on R and v_{orb}. Before constructing a more realistic model of disk truncation in a galaxy cluster, we investigate the effect of the internal metallicity gradient on the cluster-scale metallicity gradient using an idealised approach in next subsection (§ 4.3.3).

4.3.3 Internal metallicity gradients vs. cluster-scale gradients

IFU observations of local field galaxies indicate the existence of a universal negative internal metallicity gradient for local disk galaxies (Zaritsky et al. 1994; Sánchez et al. 2014; Ho et al. 2015). The observation of metallicity enhancement via truncation of outer-galactic disk is based on the assumption that all galaxies have a negative internal metallicity gradient. To quantify the effect of an internal metallic-

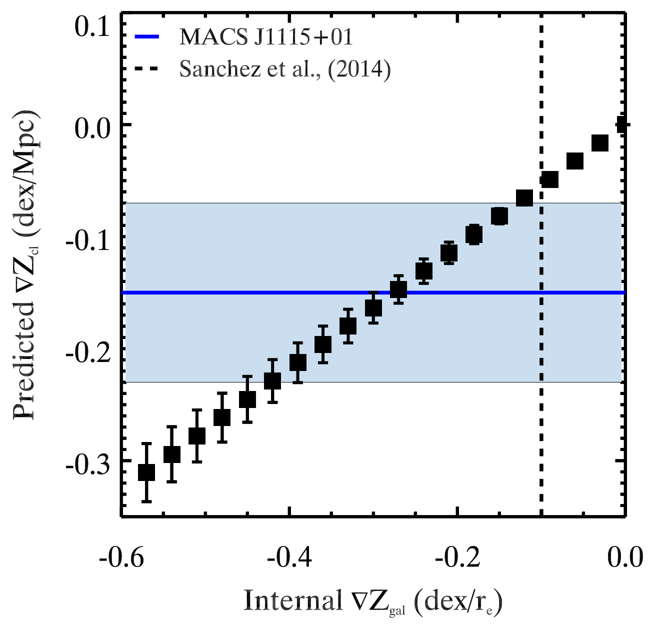

Figure 4.3: The predicted cluster-scale metallicity gradient ($\nabla Z_{\rm cl}$) as a function of the internal metallicity gradient ($\nabla Z_{\rm gal}$) of the infalling galaxy from the idealised model of disk truncation described in Section 4.3.3. The blue solid line and shaded region represent the the mean and 1σ error for the $\nabla Z_{\rm cl}$ observed for MACS J1115+01 in Chapter 3. The black dashed line represent the characteristic $\nabla Z_{\rm gal}$ for the CALIFA sample from Sánchez et al. (2014). For infalling galaxies with a constant $\nabla Z_{\rm gal} = -0.1\,{\rm dex/r_e}$, our RPS model predict a $\nabla Z_{\rm cl} = -0.05\,{\rm dex/Mpc}$.

ity gradient on cluster-scale metallicity gradient, we manually place a galaxy with fixed internal properties (such as stellar mass and internal metallicity gradient) at different cluster-centric distances.

We define $\nabla Z_{\rm cl}$ as the cluster-scale gradient in the integrated metallicity of star-forming cluster galaxies and $\nabla Z_{\rm gal}$ as the internal metallicity gradient of a satellite galaxy. We assume that a $10^{10} M_\odot$ galaxy with a particular $\nabla Z_{\rm gal}$ is falling into the cluster with an orbital velocity of 1000 km/s. The empirical stellar mass-size relation is used to estimate the stellar disk scale length for this $10^{10} M_\odot$ galaxy (Mosleh et al. 2013). We manually place the satellite galaxy at different cluster-centric distance and estimate the stripping radius at each cluster-centric distance using our RPS model (Equation (4.8)). We estimate the integrated metallicity ($Z_{\rm int}(R)$) at each cluster-centric distance by taking an intensity-weighted average of $\nabla Z_{\rm gal}$ within $r_{\rm strip}$ using following equation:

$$Z_{\rm int}(R) = \int_0^{r_{\rm strip}(R)} \exp(-r/r_e) \nabla Z_{\rm gal} dr, \tag{4.13}$$

where we assume an exponentially declining profile for the intensity (Hughes et al. 2013). We perform a linear fit between $Z_{\rm int}(R)$ and the cluster-centric distance to estimate $\nabla Z_{\rm cl}$. To estimate the relation between $\nabla Z_{\rm cl}$ and $\nabla Z_{\rm gal}$, we assume that the internal metallicity gradient of the infalling galaxy varies between $-0.6 \leq \nabla Z_{\rm gal} \leq 0.0\,{\rm dex/r_e}$ (Yuan et al. 2011; Jones et al. 2013; Ho et al. 2015) and measure $\nabla Z_{\rm cl}$ for each value of the $\nabla Z_{\rm gal}$.

Figure 4.3 shows that $\nabla Z_{\rm cl}$ is directly proportional to the $\nabla Z_{\rm gal}$ of the satellite galaxy, i.e., $\nabla Z_{\rm cl} = 0.54 \times \nabla Z_{\rm gal}$. Our RPS model predicts a $\nabla Z_{\rm cl}$ of $-0.05\,{\rm dex/Mpc}$, when adopting a $\nabla Z_{\rm gal} = 0.1\,{\rm dex}/r_e$, characteristic for CALIFA galaxies (Sánchez

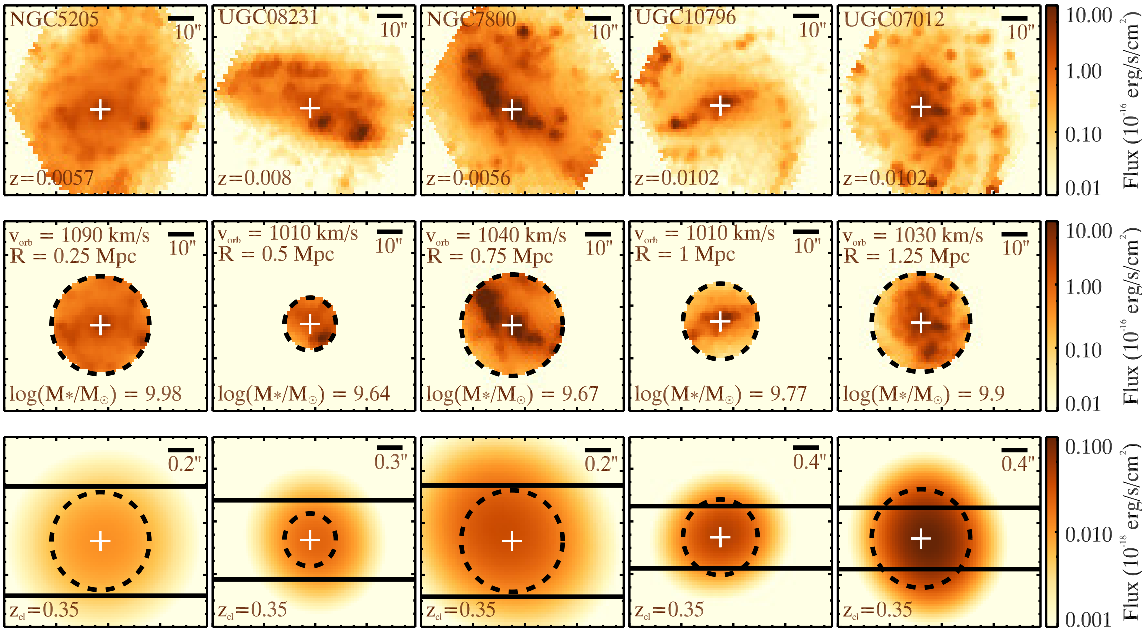

Figure 4.4: Top panel: The wavelength-collapsed Hα intensity map for 5 CALIFA galaxies (Same as top panel in Figure 4.2). **Middle panel:** Truncated Hα intensity map, where the stripping radius is calculated using R and v_{orb} specified in each panel. The dashed-circle represents the truncation region. **Bottom panel:** The truncated Hα intensity map after redshifting galaxies to $z_{\rm cl} = 0.35$, with a seeing of $0.''8$. The black lines represents the $5'' \times 1''$ DEIMOS slit. To generate a 1D-slit spectra, we integrate the flux inside the DEIMOS slit.

et al. 2014). By using the CALIFA sample to simulate cluster galaxies at $z_{\rm cl} = 0.35$, we neglect the possible evolution in the internal metallicity gradients of star-forming galaxies out to a redshift of $z_{\rm cl} = 0.35$.

The evolution of the internal metallicity gradient of star-forming galaxies with redshift is contentious. Star-forming galaxies at $z \sim 0$ have a universal negative internal metallicity gradient (Sánchez et al. 2014; Ho et al. 2015). The adaptive-optics observations of lensed galaxies show that the internal metallicity gradient steepens with redshift (Yuan et al. 2011; Jones et al. 2013). In contrast, seeing limited observations of non-lensed galaxies find a flat metallicity gradient for high redshift galaxies (Wuyts et al. 2016). Yuan et al. (2013b) show that low spatial resolution in seeing limited conditions leads to gradient flattening in the high-redshift observations. If $\nabla Z_{\rm cl}$ observed for MACS J1115+01 in Chapter 3 is caused only by the truncation of outer-galactic disks, then we predict an $\nabla Z_{\rm gal} = -0.28\,{\rm dex/r_e}$ for MACS J1115+01 cluster members in this idealised model. This internal gradient is significantly steeper than any observations of high-redshift galaxies and is unlikely to be real. Nevertheless, the variation in $\nabla Z_{\rm gal}$ would introduce scatter in the observed $\nabla Z_{\rm cl}$ and would be interesting to conduct observations to measure $\nabla Z_{\rm gal}$ for MACS J1115+01 cluster members.

Using a single galaxy with fixed internal properties disregards the scatter introduced in the predicted $\nabla Z_{\rm cl}$ due to the scatter in internal properties of infalling galaxies. To realistically simulate disk truncation in MACS J1115+01, we use a stellar mass selected sample of CALIFA galaxies.

4.4 Simulating disk truncation in a galaxy cluster

We simulate disk truncation in a galaxy cluster by uniformly distributing the mass selected CALIFA galaxies at different cluster-centric radii. The stripping radius for each galaxy is evaluated using Equation (4.8). To compare with the observations from Chapter 3, we model the ICM density profile using Equations (4.10) to (4.12), where the cluster parameters were obtained from Merten et al. (2015) for MACS J1115+01. We neglect the central 200 kpc region in the cluster because the stripping radius becomes almost negligible beyond 200 kpc (i.e., cold gas is completely stripped off the cold gas; Figure 4.5). Note that our results do not change significantly by using a minimum cluster-centric radius of 500 kpc as used in Chapter 3.

The observations in Chapter 3 give us the velocity dispersion along the line-of-sight ($\sigma_{\rm los} = 960\,{\rm km/s}$) for the cluster members. To assign orbital velocity, we assume that our simulated galaxy cluster is isotropic, i.e., all three components of velocities have the same Gaussian distribution with dispersion equal to $\sigma_{\rm los}$. The orbital velocity is given by $v_{\rm orb} = \sqrt{v_x^2 + v_y^2 + v_z^2}$. Thus, $v_{\rm orb}$ follow a Maxwell-Boltzmann distribution

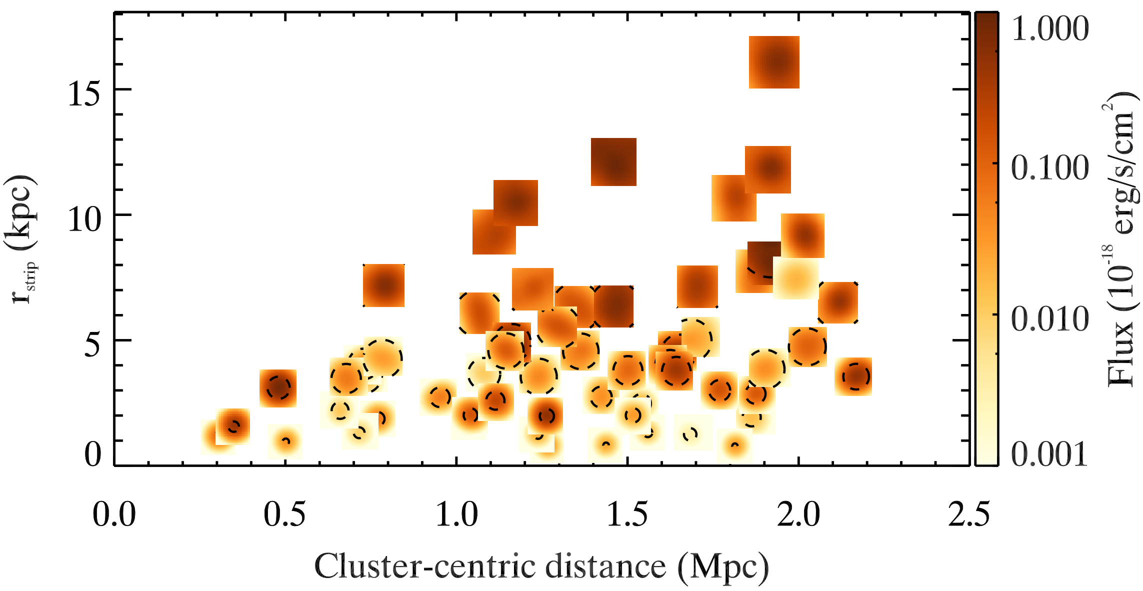

Figure 4.5: The variation of stripping radius ($r_{\rm strip}$) versus cluster-centric distance for the selected CALIFA galaxies. The stripping radius is calculated by assuming a uniform distribution of galaxies in the cluster and the Gaussian distribution of the orbital velocity. Galaxies with $r_{\rm strip}$ greater than 0.5 kpc are shown on the figure. Each data points corresponds to the wavelength-collapsed Hα map of the galaxies at $z_{\rm cl} = 0.35$ and observed with a seeing of $0.8''$. The dashed circle in each Hα map defines the stripping boundary corresponding to the $r_{\rm strip}$. The $r_{\rm strip}$ shows a clear positive correlation with the cluster-centric distance, i.e., the size of galactic disk (where ISM emission line/cold gas can be detected) decreases near the cluster center. The large scatter in the stellar mass of infalling cluster galaxies results in a large scatter in the $r_{\rm strip}$ at a particular cluster-centric distance.

with mean = 1532 km/s and dispersion = 646 km/s. We assign the orbital velocity independent of a galaxy's position in the cluster.

4.4.1 Galaxies with truncated galactic disks

We compare the $\nabla Z_{\rm cl}$ observation from Chapter 3 to $\nabla Z_{\rm cl}$ observed for the mass matched sample from CALIFA DR3. We define T-CALIFA as the sample of cluster galaxies at $z_{\rm cl} = 0.35$ with truncated galactic disks for which metallicity is estimated via the mock DEIMOS observations. The stripping radius $r_{\rm strip}$ for each T-CALIFA galaxy is estimated using Equation (4.8) after assigning orbital parameters, i.e., cluster-centric radius and orbital velocity. To simulate the disk truncation, we set the flux at $r > r_{\rm strip}$ to zero for each wavelength slice, thereby suppressing the emission line flux outside the stripping radius. We emphasize that our disk truncation model removes only the cold gas at $r > r_{\rm strip}$. Other components of the galaxy such as stars, dust and the halo are intact (§ 4.5.3). However, because we are simulating observed emission line fluxes, it is reasonable to cut off data at $r > r_{\rm strip}$ because no emission line would be detected at $r > r_{\rm strip}$. After disk truncation, we redshift the galaxies to $z_{\rm cl}$ (§ 4.2.2) and conduct mock observations with DEIMOS (§ 4.2.3). The metallicity is estimated using emission line ratios [N II]/Hα and [N II]/[S II] (§ 4.2.4) extracted from the 1D-slit spectrum for each T-CALIFA galaxy.

Figure 4.4 gives a figurative description of our disk truncation simulation for a random sample of 5 galaxies. The truncation radius for each galaxy is calculated after assigning the galaxy an orbital velocity and distance from the cluster center. The middle row in Figure 4.4 shows the truncated galactic disks after reassigning the flux outside $r_{\rm strip}$ to zero. After truncating the galactic disk, we redshift the galaxies to $z_{\rm cl} = 0.35$ (§ 4.2.2) and convolve with the PSF of $0.''8$ (Figure 4.4: bottom panel). We truncate the galactic disk before redshifting to avoid spatial resolution effects in disk truncation. The 1D spectrum of the truncated galaxy is extracted by integrating the flux within a $5'' \times 1''$ DEIMOS slit (§ 4.2.3) at each wavelength slice. Figure 4.5 shows the relation between $r_{\rm strip}$ and cluster-centric distance for the full mass selected CALIFA sample. The mean stripping radius gets smaller as cluster galaxies move closer to the cluster center. The stellar mass of infalling galaxies varies almost 2 orders in magnitude, resulting in a large scatter in the $r_{\rm strip}$ of galaxies at a particular cluster-centric distance.

4.4.2 Comparison sample

To estimate the metallicity enhancement due to disk truncation, we compare the mass-metallicity relation for the T-CALIFA galaxies with the following control samples:

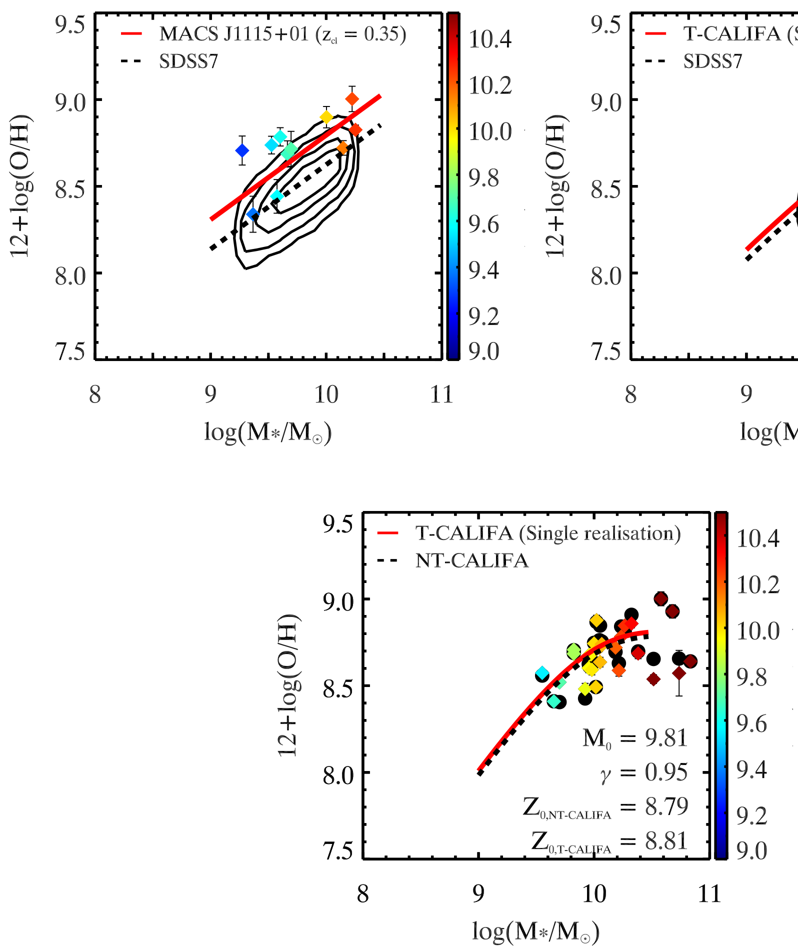

Figure 4.6: Top-left panel: The MZ relation comparison between MACS J1115+01 and the local SDSS galaxies (Figure 6 in Chapter 3). We observe an metallicity enhancement of $+0.20 \pm 0.13$ dex/Mpc for cluster members at a fixed stellar mass. **Top-right panel:** The comparison of MZ relation for T-CALIFA galaxies with the SDSS7 sample for one realisation of disk truncation simulation. The contours in left and middle panel represents the MZ relation for the local SDSS galaxies (25%, 50%, 70% and 90%). **Bottom panel:** The MZ relation comparison between T-CALIFA(diamonds) and NT-CALIFA(black circles) galaxies sample for one realisation of disk truncation simulation. The cluster data points in each panel are color coded with stellar mass. The red solid and black dashed line represents the best linear fit to MZ relation of the cluster galaxies sample and the respective comparison sample in each panel. The fit parameters are indicated in the figure legend, where $Z_{0,\mathrm{T-CALIFA}}$ is the best-fit asymptotic metallicity for T-CALIFA galaxies, $Z_{0,\mathrm{SDSS7}}$ is the best-fit asymptotic metallicity for the SDSS7 sample and $Z_{0,\mathrm{NT-CALIFA}}$ is the best-fit asymptotic metallicity for the NT-CALIFA sample. The difference between the best-fit asymptotic metallicity to the T-CALIFA sample and the control sample represents the metallicity offset due to disk truncation.

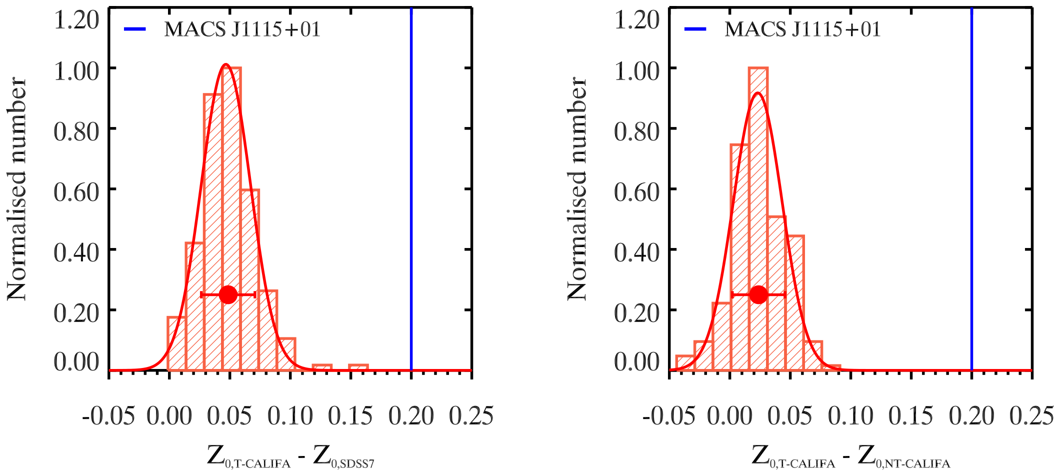

Figure 4.7: The distribution of metallicity offset between the MZ relation for the T-CALIFA galaxies and the control samples using the all realisations of the disk truncation simulation. **Left panel**: Comparison with SDSS7 sample. The red circle represents the mean (+0.05 dex) and the 1-σ scatter (0.02 dex) in the metallicity offset distribution. **Right panel** Comparison with NT-CALIFA sample. The red circle represents the mean (+0.02 dex) and the 1-σ scatter (0.02 dex) in the metallicity offset distribution. The solid blue line in each panel represents the metallicity enhancement at a fixed stellar mass observed for MACS J1115+01 in Chapter 3 (Figure 4.6: top-left panel). Disk truncation leads to a mean metallicity enhancement of 0.02 dex, but the metallicity enhancement from disk truncation is significantly less than the metallicity enhancement observed for MACS J1115+01 (0.20 ± 0.13 dex).

SDSS7 (Fiber spectroscopy)

To have a direct comparison with the metallicity offset in the mass-metallicity relation observed in Chapter 3, we use the SDSS DR7 galaxy sample as one of our control sample. The stellar mass and emission line flux measurements for SDSS DR7 galaxies are taken from the publicly available MPA-JHU catalogs [1] (Kauffmann et al. 2003a; Brinchmann et al. 2004). We use the same selection criteria as in Chapter 3 to ensure a consistent comparison sample. In brief, we remove galaxies with aperture coverage of $< 20\%$ leading to a redshift selection of $0.05 < z < 0.1$ and remove AGN galaxies using the Baldwin-Phillips-Terlevich (BPT) diagram (Baldwin et al. 1981; Phillips et al. 1986; Veilleux & Osterbrock 1987) procedure described in Kewley et al. (2006). We further remove galaxies with signal-to-noise (S/N) ratio < 3.0 for any of the following emission lines: [O II] $\lambda\lambda\,3726$, 3729, H$\beta\,\lambda\,4861$, [O III] $\lambda\lambda\,4959$, 5007, [N II] $\lambda\lambda\,6549$, 6583, H$\alpha\,\lambda\,6563$ and [S II] $\lambda\lambda\,6717$, 6731.

Non-truncated CALIFA sample

We define NT-CALIFA as the mass selected CALIFA galaxy sample redshifted to $z_{\rm cl}$ for which no disk truncation is performed. We extract the mass-metallicity relation for NT-CALIFA sample to directly compare the effect of disk truncation on metallicity. We use the same stellar mass matched sample of galaxies from the full CALIFA DR3 catalog as used for the T-CALIFA sample, redshift them to $z_{\rm cl} = 0.35$, extract 1D slit spectra and measure the global metallicity again using emission line ratios [N II]/Hα and [N II]/[S II]. The NT-CALIFA sample undergo the exact sample treatment as the T-CALIFA sample except for the disk truncation. The metallicity enhancement observed between T-CALIFA and NT-CALIFA samples can only be attributed to the bias introduced in the metallicity measurement because of disk truncation.

4.5 Comparison with observations

We extract the integrated metallicity of disk truncated cluster galaxies at $z_{\rm cl}$ (T-CALIFA; § 4.4.1). To measure the metallicity we use emission line ratios [N II]/[S II] and [N II]/H α and apply a S/N cut of 3 for all necessary emission lines. Additionally, we remove galaxies that have an AGN or the star-formation rate is less than 0.2 $M_\odot$/yr (§ 4.2.4). Méndez-Abreu et al. (2017) provide measurement of r_* for nearly 280 CALIFA DR3 galaxies out of the full CALIFA DR3 sample of 650 galaxies. The stripping radii estimation requires accurate measurement of r_*, further limiting the sample size of galaxies with reliable gas-phase metallicity estimates. To estimate the scatter introduced by the RP model, we perform multiple realisations of the disk truncation simulation, each time redistributing the mass matched CALIFA

[1] See `http://wwwmpa.mpa-garching.mpg.de/SDSS/DR7/Data/stellarmass.html`

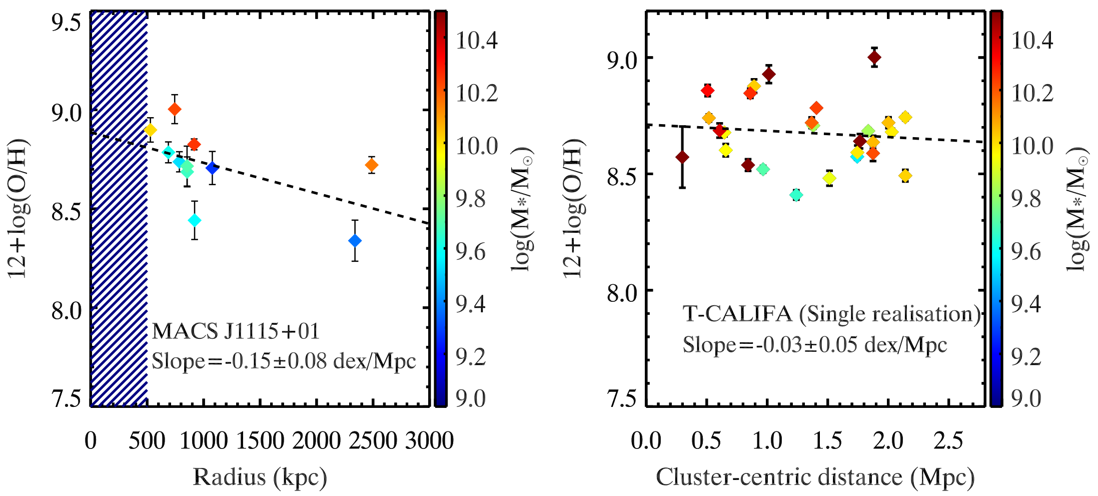

Figure 4.8: Left panel: The distribution of gas-phase metallicity of cluster members in MACS J1115+01 with respect to projected distance from the cluster center (Figure 7 in Chapter 3). **Right panel:** The distribution of integrated metallicity of star-forming galaxies in T-CALIFA sample with the cluster-centric distance for one realisation of disk truncation simulation. Each data point in both panels is color coded with the stellar mass. The dashed line in each panel represents the best linear fit to the data and the best-fit slope is labeled in the panel. We extract the intercept metallicity and the $\nabla Z_{\rm cl}$ for each realisation of disk truncation simulations to understand the distribution of $\nabla Z_{\rm cl}$ predicted by our disk truncation simulation.

galaxies in the galaxy cluster and reassigning the orbital velocity based on the Gaussian random distribution. The mean cluster-scale metallicity gradient converges in about 150 realisations of disk truncation simulation, but to avoid underestimation of scatter we repeat our disk truncation simulation for 200 realisations. Out of the 91 galaxies in the mass matched CALIFA sample, we are left with 25-30 galaxies per realisation for which metallicities could be determined.

4.5.1 Offset in the stellar mass-gas metallicity relation

The metallicity enhancement produced by disk truncation can be quantified by estimating the offset between the mass-metallicity (MZ) relation of the T-CALIFA sample and control samples. We compare the MZ relation for the T-CALIFA sample with two control samples: SDSS7 and NT-CALIFA (§ 4.4.2). We use the logarithmic form proposed by Zahid et al. (2013) parameterised as

$$12 + \log(\mathrm{O/H}) = Z_0 - \log\left[1 + \left(\frac{M_*}{M_0}\right)^{-\gamma}\right], \tag{4.14}$$

to fit the MZ relation, where Z_0 is the asymptotic metallicity, M_0 is the characteristic mass and γ represents the power law slope. The control samples are fit keeping all three parameters free. To estimate the metallicity offset between the T-CALIFA and

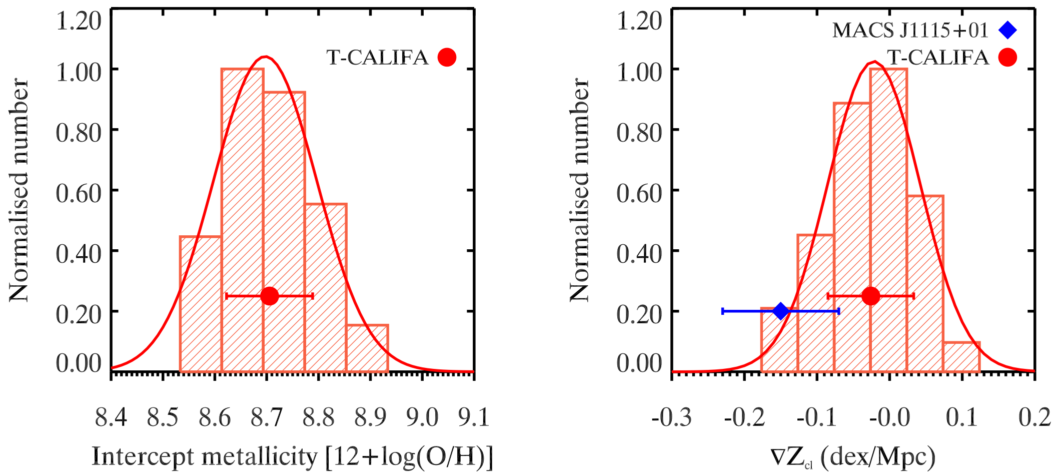

Figure 4.9: The distribution of the intercept metallicity and the $\nabla Z_{\rm cl}$ from the disk truncation simulation using full realisations of the T-CALIFA sample. **Left panel:** The intercept distribution with a mean metallicity of 8.69 ± 0.09 shown as red circle. **Right panel:** The red circle represents the mean ($\nabla Z_{\rm cl} = -0.03$ dex/Mpc) and the 1-sigma scatter (0.06 dex/Mpc) in the $\nabla Z_{\rm cl}$ distribution from the disk truncation simulation. The Blue diamond represents $\nabla Z_{\rm cl}$ observed for MACS J1115+01 cluster in Chapter 3 (Figure 4.8: left panel). The $\nabla Z_{\rm cl}$ observed for MACS J1115+01 is consistent with the $\nabla Z_{\rm cl}$ produced from disk truncation simulations within 1-sigma errors.

control samples, we fit the T-CALIFA sample as a single parameter model keeping the M_0 and γ fixed to the comparison control sample's best-fit values. The difference in the asymptotic metallicity (Z_0) for the T-CALIFA sample and the comparison control sample is equivalent to the metallicity offset between two samples.

In Chapter 3, we observe a 0.20 ± 0.13 dex metallicity enhancement for cluster members in MACS J1115+01 at a fixed stellar mass (Figure 4.6: top-left panel). Figure 4.6 shows one realisation of the MZ relation of the T-CALIFA sample in comparison with the SDSS7 (Figure 4.6: top-right panel) and the NT-CALIFA sample (Figure 4.6: bottom panel). The fit parameters for the MZ relation of the T-CALIFA galaxies and the referenced control sample are listed in the legend of Figure 4.6. For a statistical estimate of the metallicity offset between the T-CALIFA and control samples, we measure the metallicity offset for each realisation of disk truncation simulation.

Figure 4.7 gives the distribution of the metallicity offset between the T-CALIFA and the control samples. Our model predicts a mean metallicity enhancement of 0.02 dex for the disk truncated CALIFA galaxies with a 1-sigma scatter of 0.02 dex on the MZ relation. Disk truncation produces the slightly higher mean metallicity enhancement between the T-CALIFA and the SDSS7 sample but within the statistical uncertainties. The truncation of outer-galactic disk due to the RPS produces a 0.02 dex enhancement in the integrated metallicity of cluster galaxies at a fixed stellar mass. The mean metallicity enhancement from disk truncation is significantly less than the metallicity enhancement observed for MACS J1115+01 in Chapter 3 (0.20 ± 0.13 dex).

4.5.2 Cluster-scale metallicity gradient

In Chapter 3, we observe $\nabla Z_{\rm cl} = -0.15 \pm 0.08$ dex/Mpc in the integrated metallicity of star-forming galaxies for MACS J1115+01 (Figure 4.8: Left panel). Our disk truncation simulation aims at understanding the contribution of RPS in the $\nabla Z_{\rm cl}$ observed for MACS J1115+01. We have simulated disk truncation using the IFU datacubes from the CALIFA survey and manually truncate them using a semi-analytic model of RPS. The right panel in Figure 4.8 shows the distribution of the integrated metallicity of the T-CALIFA sample with the cluster-centric distance for one realisation of the disk truncation simulation. We perform robust linear regression to derive the $\nabla Z_{\rm cl}$ for each realisation of the disk truncation simulation.

Figure 4.9 shows the distribution of the intercept metallicity and $\nabla Z_{\rm cl}$ produced from multiple realisations of the disk truncation simulation (§ 4.4). Our disk truncation simulations produce a mean $\nabla Z_{\rm cl}$ of -0.03 dex/Mpc with a 1-sigma scatter of 0.06 dex/Mpc in the integrated ISM metallicity of star-forming galaxies. The mean cluster-scale metallicity gradient from the disk truncation simulation is shallower than the $\nabla Z_{\rm cl}$ observed for MACS J1115+01, although both are consistent with each other within 1-sigma standard deviations. We require measurement of $\nabla Z_{\rm cl}$ in more galaxy clusters to distinguish the existing $\nabla Z_{\rm cl}$ distribution from the $\nabla Z_{\rm cl}$ distribution produced by the truncation of outer-galactic disk. We investigate the origin of the scatter in our simulated cluster-scale metallicity gradient in the following subsection (§ 4.5.3).

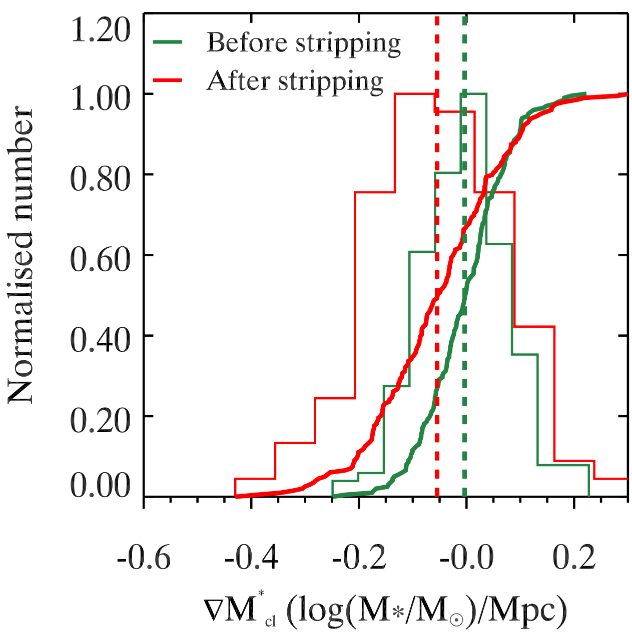

Figure 4.10: The distribution of stellar mass gradient in our disk truncation simulations. The green and red histograms represent the $\nabla M^*_{\rm cl}$ measured before and after applying the RPS model respectively. The red and green curve represents the corresponding cumulative distribution of the $\nabla M^*_{\rm cl}$. The dashed lines show the mean of the two distributions. The disk truncation shifts the mean of the $\nabla M^*_{\rm cl}$ distribution from 0.00 $\log(M_*/M_\odot)$/Mpc before stripping to -0.05 $\log(M_*/M_\odot)$/Mpc after stripping.

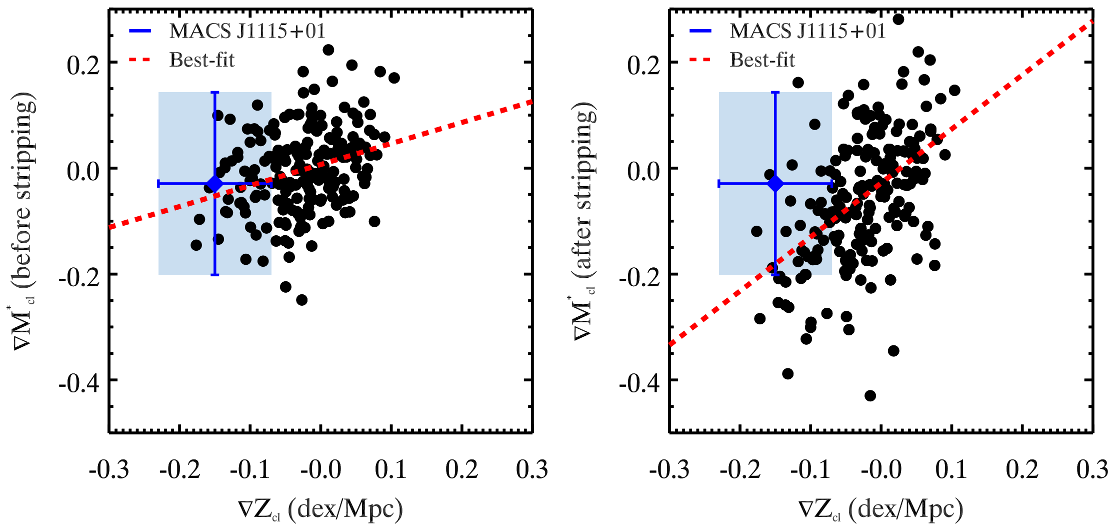

Figure 4.11: The comparison of stellar mass gradient ($\nabla M^*_{\rm cl}$) and the estimated cluster-scale metallicity gradient ($\nabla Z_{\rm cl}$). **Left panel:** The $\nabla M^*_{\rm cl}$ measured before stripping versus $\nabla Z_{\rm cl}$. The $\nabla M^*_{\rm cl}$ in y-axis is the best-fit slope between the stellar mass and cluster-centric distance (see the Appendix). The red dashed line represents the best linear fit and has a slope of 0.39 ± 0.09 $\log(M_*/M_\odot)$/dex. **Right panel:** The $\nabla M^*_{\rm cl}$ after stripping versus $\nabla Z_{\rm cl}$. The $\nabla M^*_{\rm cl}$ for each realisation is estimated by only including the simulated satellite galaxies with metallicity measurements (see the Appendix). The dashed line represents the best linear fit and has a slope of 1.00 ± 0.12 $\log(M_*/M_\odot)$/dex. The blue box in each panel represents the mean and 1-sigma measurement error in the $\nabla Z_{\rm cl}$ and the $\nabla M^*_{\rm cl}$ observed for MACS J1115+01 in Chapter 3. The $\nabla Z_{\rm cl}$ from disk truncation simulation is most sensitive to the $\nabla M^*_{\rm cl}$ introduced by RPS.

4.5.3 The scatter in cluster-scale metallicity gradient

The predicted cluster-scale metallicity gradient from our disk truncation simulation ranges from -0.21 to $+0.18$ dex/Mpc (Figure 4.9: right panel). To simulate cluster galaxies, we uniformly distribute the mass selected CALIFA galaxies with respect to the cluster-centric distance (§ 4.4.1). We define $\nabla M^*_{\rm cl}$ as the best-fit slope between the stellar mass of simulated cluster galaxies and the cluster-centric distance (see the Appendix). Before truncating the galactic disk, we measure a mean $\nabla M^*_{\rm cl} = -0.00 \log(M_*/M_\odot)$/Mpc (Figure 4.10) because of the uniform distribution of selected CALIFA galaxies with respect to the cluster-centric distance. The redistribution of galaxies in the cluster for each realisation introduces a scatter of 0.08 $\log(M_*/M_\odot)$/Mpc in the $\nabla M^*_{\rm cl}$ before stripping the galactic disks (Figure 4.10).

The RPS shifts the $\nabla M^*_{\rm cl}$ distribution towards negative values and increases the scatter. The mean $\nabla M^*_{\rm cl}$ after disk truncation is $-0.05 \log(M_*/M_\odot)$/Mpc with a 1-sigma scatter of 0.12 $\log(M_*/M_\odot)$/Mpc (Figure 4.10). The $\nabla M^*_{\rm cl}$ after truncation is estimated by only including galaxies with measurable metallicities (see the Appendix). The KS-test yields a probability of nearly zero for the $\nabla M^*_{\rm cl}$ distribution before and after truncation to be derived from the same distribution. The negative $\nabla M^*_{\rm cl}$ implies that the star-forming galaxies near the cluster center are more massive than the star-forming galaxies in the cluster outskirts.

Our RPS model does not directly affect the stellar mass of cluster galaxies. The cold gas supply of the low-mass galaxies near the cluster center gets completely stripped of due to RPS. The star formation in fully gas stripped low mass galaxies is suppressed instantaneously resulting in the complete loss of emission line flux. Therefore, we cannot measure the metallicity of the fully gas stripped low mass galaxies near the cluster center via optical emission lines. A disk truncation simulation realisation with an initial $\nabla M^*_{\rm cl}$ of zero can have a negative $\nabla M^*_{\rm cl}$ after truncation because of the selective removal of the low mass galaxies from the cluster core.

We find that the $\nabla Z_{\rm cl}$ predicted by our disk truncation simulation has a direct correlation with the $\nabla M^*_{\rm cl}$ measured after performing disk truncation. The $\nabla Z_{\rm cl}$ shows a weak correlation with the $\nabla M^*_{\rm cl}$ prior to disk truncation (Figure 4.11: left panel). We find a slope of $0.39 \pm 0.09 \log(M_*/M_\odot)$/dex between the $\nabla M^*_{\rm cl}$ measured before disk truncation and the cluster-scale metallicity gradient. On comparing the $\nabla Z_{\rm cl}$ with the $\nabla M^*_{\rm cl}$ measured after disk truncation, we find a significantly steeper slope of $1.00 \pm 0.13 \log(M_*/M_\odot)$/dex (Figure 4.11: right panel). The best-fit slope of 1.00 $\log(M_*/M_\odot)$/dex between the $\nabla Z_{\rm cl}$ and the $\nabla M^*_{\rm cl}$ after disk truncation imply that the cluster-scale metallicity gradient in our disk truncation simulation is most sensitive to the $\nabla M^*_{\rm cl}$ introduced by RPS. The negative $\nabla M^*_{\rm cl}$ introduced by the RPS results in a negative $\nabla Z_{\rm cl}$ because massive galaxies are also metal-rich.

The $\nabla M^*_{\rm cl}$ observed in Chapter 3 for MACS J1115+01 is $-0.03 \pm 0.17 \log(M_*/M_\odot)$/Mpc. The large measurement error in the $\nabla M^*_{\rm cl}$ for MACS J1115+01 does not rule out that the observed $\nabla Z_{\rm cl}$ is induced by $\nabla M^*_{\rm cl}$. Almost 85% of disk truncation realisations lie outside the 1-sigma range of the $\nabla Z_{\rm cl}$ and the $\nabla M^*_{\rm cl}$ observed for MACS J1115+01 in Chapter 3 (Figure 4.11: right panel). To separate the effect of $\nabla M^*_{\rm cl}$ from the effect of $\nabla Z_{\rm gal}$, we select disk truncation realisations with $\nabla M^*_{\rm cl} = 0.00$ after truncation. We estimate a mean $\nabla Z_{\rm cl}$ of -0.01 dex/Mpc with 1-sigma scatter of 0.05 dex/Mpc for disk truncation realisations with zero $\nabla M^*_{\rm cl}$ after truncation. The stellar mass independent $\nabla Z_{\rm cl}$ is statistically consistent with the $\nabla Z_{\rm cl} = -0.05$ dex/Mpc predicted in Section 4.3.3 for a cluster galaxy with $\nabla Z_{\rm gal}$ equivalent to the characteristic $\nabla Z_{\rm gal}$ of CALIFA galaxies (-0.1 dex/r_e; Figure 4.3). The negative cluster-scale metallicity gradient in our disk truncation simulation is caused by the negative gradient in stellar mass induced by the selective removal of low mass galaxies from the cluster core.

4.6 Discussion

4.6.1 Assumptions in disk truncation model and theoretical uncertainties

Here, we discuss some of the inherent assumptions in our RP model and their potential effect on the RP strength and thus the metallicity gradient measurements:

- **Effect of inclination angle:** The basic equation of RP stripping by Gunn & Gott (1972) assumes that galaxies are falling face-on in the cluster, i.e., the infalling galaxies experience maximum RP. Hydrodynamical simulations of RP stripping suggest that the inclination angle does not play a significant role as long as the galaxies are not moving at an almost edge-on geometry (Roediger & Brüggen 2006; Jáchym et al. 2009; Steinhauser et al. 2016). The total mass loss due to stripping is not affected by the inclination angle but the mass-loss rate is highest for galaxies falling face-on in the cluster (Steinhauser et al. 2016). Hence, we are safe to neglect the role of inclination angle on RP stripping strength.

- **Sharp cut-off in radial gas profile:** Our model assumes that all the cold gas outside the $r_{\rm strip}$ will be removed instantaneously, causing a sharp cut-off in the radial profile of cold gas. Most semi-analytic models with a sharp cut-off in cold gas profile overproduce the fraction of quenched galaxies in the cluster (Guo et al. 2013), suggesting an overestimation of the RP stripping effect. Recent simulations by Luo et al. (2016) relaxes this assumption by assuming that only a fraction of cold gas is removed outside of the stripping radius. However, the continuous cold gas depletion models also fail to improve the over-estimation of the quenched galaxy fraction. Our model uses a sharp cut-off in the radial cold gas profile, thus our results correspond to maximum RP stripping.

- **Galactic orbits in the cluster:** The Gunn & Gott (1972) formalism assumes that all galaxies are falling into the cluster in radial orbits and are on their first pass through the cluster. Three-dimensional hydrodynamical simulations suggest that the RPS strength depends on the orbit of the infalling galaxies. McCarthy et al. (2008) show that galaxies with peripheral orbits undergo a single RP stripping event whereas galaxies with radial orbits undergo multiple RP stripping events depending on the number of pericentric passage. However, more than 80% of the total mass-loss occurs on the first passage. Steinhauser et al. (2016) show that galaxies with extreme radial orbits undergo significant RPS, whereas galaxies in peripheral orbits only experience mild stripping of gas mass. Thus, the assumption about the galactic orbit would significantly effect the average RPS experienced by satellite cluster galaxies. Our RP prescription assumes that all satellite galaxies have radial orbits, thus providing a upper bound to RP stripping in clusters.

- **Instantaneous gas stripping:** The RP model assumes instantaneous stripping of cold gas and that the surface gas profile inside the stripping radius remains unaltered. The metallicity measurements via optical emission lines are sensitive only towards the star-forming regions. The RPS timescales are of the order of $t_{\rm strip} \sim 10 - 100\,{\rm Myr}$, whereas the depletion timescale of cluster galaxies are $t_{\rm dep} \sim 1\,{\rm Gyr}$. Thus, the star-formation is instantaneously suppressed in the truncated region of the galaxy because $t_{\rm strip} << t_{\rm dep}$. The star-formation inside the stripping radius continues at least till $t \sim t_{\rm dep}$. Relaxing the instantaneous stripping assumption would not significantly affect the RP strength and its effect on integrated metallicity.

- **ICM density profile:** To describe the ICM density, we use the re-scaled NFW density profile, re-scaled based on the baryonic fraction and the kinetic energy (Makino et al. 1998). Tecce et al. (2010) show that the analytic form for the ICM density overestimates the RP particularly for galaxy cluster at $z \geq 0.5$. The analytic form of the ICM density assumes that the galaxy cluster are relaxed dynamical structures that might not be true particularly at high redshift. Our simulated galaxy cluster is at $z = 0.35$ and is a dynamically relaxed system as suggested by the X-ray observations (Allen et al. 2007). The analytic form is expected to provide a good description of the density profile of the cluster. The stripping radius changes logarithmically with the ICM density $r_{\rm strip} \propto \ln(\rho_{\rm ICM})$, i.e., $r_{\rm strip}$ depends weakly on the ICM density. Changing the ICM density profile would not significantly affect the cluster-scale metallicity gradient distribution.

- **Stellar and gas disk scale length:** To model the surface mass density of the stellar and gaseous component of galaxies, we assume that both the stellar disk and the gaseous disk have the same scale length. Neutral HI gas disks can extend up to twice the stellar disk size (Swaters et al. 2005; Bosma 2016, and references therein), but the cold gas disk closely follows the stellar disk (Bigiel & Blitz 2012; Cormier et al. 2016). However, the stripping radius in

Equation 4.8 is directly proportional to the scale length of the cold gas disk, therefore uncertainty in the gas disk scale length can significantly affect the stripping radii. We assume same scale length for both gas and stellar disk because otherwise the RPS model would not have an analytic solution.

- **Radial distribution of cluster galaxies:** To setup our disk truncation simulation, we assume that galaxies are uniformly distributed across the cluster radius. The surface density distribution of both red and blue satellite galaxies follows the NFW profile, albeit with different concentration parameters (Collister & Lahav 2005; Budzynski et al. 2012; Zenteno et al. 2016). The RPS can modify the radial distribution of star-forming galaxies in the cluster. Ascertaining the radial distribution of star-forming galaxies in clusters without RP is non-trivial both observationally and via simulations. A uniform radial distribution provides a first order initial condition for the RPS to act upon. Choosing a different initial radial density distribution without invoking the stellar mass segregation would not significantly affect the predicted cluster-scale metallicity gradient distribution.

  A uniform radial distribution underestimates the average RPS particularly at radii close to the cluster center. Underestimating the average RPS can potentially affect the mean metallicity enhancement of the MZ relation. To assess the effect of the radial distribution on the MZ relation, we weight galaxies according to the radial distance while fitting the MZ relation. Galaxies near the cluster center have higher weights than galaxies in the outskirts. We do not observe a significant change in the mean and 1-sigma scatter of the metallicity enhancement. Thus, the effect of RPS on the gas-phase metallicity is unaffected by the radial distribution of galaxies in the cluster.

- **Redshift evolution of internal properties of galaxies:** We neglect any redshift evolution in the stellar mass function of field galaxies and $\nabla Z_{\rm gal}$ by matching the stellar mass function with the SDSS DR7 data at $z \sim 0$ and simply redshifting the CALIFA galaxies to $z_{\rm cl}$. The shape of the stellar mass function does not change significantly at intermediate redshift but the characteristic galaxy mass is higher in the high redshift clusters than in the local galaxy clusters or field galaxies (Vulcani et al. 2011). An absolute shift in the characteristic stellar mass would not affect the cluster-scale metallicity gradient. Observations of local field galaxies show that all isolated spiral galaxies have the same internal metallicity gradient within $\pm 0.14\, dex/R_{25}$ (Ho et al. 2015; Sánchez et al. 2016). However, the internal metallicity gradient of spiral galaxies evolves with redshift (Yuan et al. 2013b; Jones et al. 2013; Wuyts et al. 2016). In our simulation, we redshift the CALIFA galaxies from an average redshift of $z = 0.01$ to $z_{\rm cl} = 0.35$. This assumes no metallicity gradient evolution till redshift of $z_{\rm cl} = 0.35$, which might not be true. If the internal metallicity gradient of infalling galaxies steepens with redshift then the cluster-scale metallicity gradient distribution from disk truncation would shift towards more negative values (see § 4.3.3).

Considering all assumptions incorporated in our disk-truncation model and the results from recent hydrodynamical simulations, the analytic model of RP stripping used in semi-analytic models corresponds to maximum stripping strength (Steinhauser et al. 2016; Natarajan et al. 2017). The cluster-scale metallicity gradient estimated via our disk-truncation model provides an upper-bound to cluster-scale metallicity gradient produced purely by RP stripping.

4.6.2 Origin of cluster-scale metallicity gradient in the RPS simulation

RPS introduces a mean negative gradient in the stellar mass of galaxies with the cluster-centric distance (Figure 4.10). RP completely strips off the cold gas supply of the low stellar mass galaxies in the cluster core, i.e., only high stellar mass galaxies continue to form stars in the cluster core. Numerical simulations of RPS also conclude that the gas fraction lost due to stripping is higher for low mass galaxies (Bekki 2009). The metallicity measurements via optical emission lines are sensitive only to star-forming galaxies. Thus, selective quenching of the low mass galaxies in the cluster core introduces a negative gradient in the stellar mass of star-forming galaxies. The mean negative cluster-scale metallicity gradient in our disk truncation simulation is caused by the negative stellar mass gradient (Figure 4.11: right panel).

Our simulation predict a nearly flat ∇Z_{cl} purely by the stripping of outer galactic disk that is inconsistent with the ∇Z_{cl} in observations (-0.01 dex/Mpc compared to -0.15 ± 0.08 dex/Mpc). Our maximal RPS model predicts significantly smaller metallicity enhancement of the MZ relation than observations ($+0.02$ dex compared to $+0.20$ dex). We suspect that additional physical mechanisms such as self-enrichment via strangulation might be necessary to fully reproduce the observed cluster-scale metallicity gradient and metallicity enhancement of the MZ relation. Observations of more galaxy clusters are required to fully sample the existing cluster-scale metallicity gradient distribution and differentiate from the metallicity gradient distribution produced purely by disk truncation.

4.7 Conclusion

The truncation of the outer-galactic disk in the cluster environment due to RPS has been used to explain the enhanced metallicity of cluster galaxies compared to counterpart field galaxies (Hughes et al. 2013). In Chapter 3, we present the first observation of a cluster-scale gradient in the ISM metallicity of star-forming cluster members. We hypothesize that the self-enrichment of cluster members via strangulation and/or the truncation of outer-galactic disk can produce a negative gradient in the integrated metallicity of cluster members. In this paper, we simulate disk-truncation using an analytic model of RPS. We use a stellar-mass matched sample of CALIFA galaxy (Figure 4.1) to create a mock sample of disk truncated cluster galaxies. We compare the prediction from our disk truncation simulations with the observations from Chapter 3 by conducting mock DEIMOS observations.

Our model of disk truncation results in a mean cluster-scale metallicity gradient of −0.03 dex/Mpc with a 1-sigma scatter of 0.06 dex/Mpc (Figure 4.9: right panel). The cluster-scale metallicity gradient observed for MACS J1115+01 in Chapter 3 lies within the cluster-scale metallicity gradient distribution produced by our disk truncation simulation (Figure 4.9: right panel). We estimate a metallicity enhancement of +0.02 dex by comparing the MZ relation of the selected CALIFA galaxies before and after disk truncation (Figure 4.7: right panel). The metallicity enhancement from disk truncation is significantly smaller than the metallicity enhancement observed for MACS J1115+01 (+0.20 dex). The random distribution of galaxies in the clusters produces a 0.08 $\log(M_*/M_\odot)$/Mpc scatter in the stellar mass gradient of cluster members. The scatter in stellar mass distribution is the primary source of scatter in the cluster-scale metallicity gradient estimated in our disk truncation simulation.

RPS induces a negative gradient in the stellar mass of star-forming galaxies (Figure 4.10). The stellar mass of a galaxy remains unaffected in our RPS model, but RPS leads to complete loss of the gas supply of low mass galaxies in the cluster core. Only massive galaxies continue to form stars in the cluster cores, resulting in a negative gradient in the stellar mass of star-forming cluster galaxies with cluster-centric distance. The cluster-scale metallicity gradient predicted in our disk truncation simulation is most sensitive to the stellar mass gradient induced by the RPS (Figure 4.11: right panel). The mass segregation induced by the selective removal of low mass galaxies drive the negative cluster-scale metallicity gradient predicted in our simulation.

The stellar mass independent cluster-scale metallicity gradient predicted by our disk truncation simulation is −0.01 dex/Mpc with a 1-sigma scatter of 0.05 dex/Mpc, which is significantly smaller than the gradient of −0.15 ± 0.08 dex/Mpc observed in MACS J1115+01. Some of the assumptions in our RPS model such as the sharp cut-off in the radial gas profile and single infall in radial orbits only maximize the strength of RP in galaxy clusters (§ 4.6.1). Thus, the truncation of outer galactic disk via RPS alone can not explain the cluster-scale metallicity gradient observed in MACS J1115+01.

Observations of cluster-scale metallicity gradients in more galaxy clusters are required to characterise the full range of cluster-scale metallicity gradients existing in galaxy clusters. A flat mean cluster-scale metallicity gradient and the small metallicity enhancement of the MZ relation in our disk truncation simulation suggest that additional physical mechanisms such as strangulation are likely to be required to reproduce the observed cluster-scale metallicity gradient. In the future, we plan to incorporate a simple chemical evolution model with stripped neutral Hydrogen to understand the effect of strangulation on the integrated cluster member metallicities.

Acknowledgements

The author thank the referee for providing useful comments and suggestions to improve the quality of the paper. This study uses data provided by the Calar Alto Legacy Integral Field Area (CALIFA) survey (http://califa.caha.es/). Based on observations collected at the Centro Astronómico Hispano Alemán (CAHA) at Calar Alto, operated jointly by the Max-Planck-Institut fűr Astronomie and the Instituto de Astrofísica de Andalucía (CSIC). A.G. acknowledges I-Ting Ho for help with the CALIFA data and Melanie Kaasinen for her help in the editing of this paper. L.J.K. gratefully acknowledges support from an Australian Research Council (ARC) Laureate Fellowship (FL150100113). K. Tran acknowledges support by the National Science Foundation under Grant #1410728. Davide Martizzi was supported by the Swiss National Science Foundation as an Advanced Postdoc.Mobility Fellow until November 2016; grant number P300P2_161062.

Chapter 5

Chemical pre-processing of star-forming cluster galaxies

Context and Contribution

This chapter is originally accepted as *Chemical pre-processing of cluster galaxies over the past 10 billion years in the IllustrisTNG simulations*, **A. Gupta, T. Yuan, P. Torrey, M. Vogelsberger, D. Martizzi, K. Tran, L. Kewley, F. Marinacci, D. Nelson, A. Pillepich, L. Hernquist, S. Genel, V. Springel, in press, MNRAS. This chapter is included in the thesis as a representation of my contribution to understanding the origin of metallicity enhancement for star-forming cluster galaxies in IllustrisTNG simulation. The analysis technique was conceived and conducted by me. The whole paper was written by myself with suggestions provided by co-authors.**

5.1 Introduction

The chemical abundance of galaxies encodes the cumulative history of baryonic processes such as star formation and gas inflow/outflow. Observations clearly show that the cluster environment causes morphological and color transformations of galaxies (e.g., Dressler 1980). However, the impact of cluster-scale overdensities on the chemical evolution of galaxies remains controversial. Observations at $z \sim 0$ find a minimal difference (at most 0.05 dex) in the mass-metallicity relation (MZR) of cluster and field star-forming (SF) galaxies (Ellison et al. 2009; Pasquali et al. 2012; Pilyugin et al. 2017a). On the other hand, significant dependencies of the gas-phase metallicity on the cluster-centric distance and the cluster dynamic state are observed (Petropoulou et al. 2012; Gupta et al. 2016). Observations of the MZR at $z > 1.0$ are reported for only a handful of clusters with conflicting results (Tran et al. 2015; Valentino et al. 2015; Kacprzak et al. 2015).

In a hierarchical ΛCDM Universe, massive clusters form through the merger of smaller galaxy groups. Physical properties of group galaxies may be modified prior to accretion onto the main cluster, a process referred to as "pre-processing" (e.g., Zabludoff & Mulchaey 1998; Hou et al. 2014). The most recent observational evidence of pre-processing includes H I-deficiency and quenching of SF in galaxy groups (Brown et al. 2017b; Bianconi et al. 2018), though the significance of group pre-processing is debatable (e.g., Berrier et al. 2009). Darvish et al. (2015a) find ~ 0.10 dex higher metallicity for galaxies in a filamentary structure at $z \sim 0.5$ than the counterpart field galaxies, suggesting a pre-processing role of galaxy filaments on the metallicity. Whether, when and how the chemical abundance of galaxies is altered in the cluster formation history remains an open question.

Current observations are plagued by poorly understood systematic errors such as projection effects, interlopers, selection biases and metallicity diagnostics. These errors can easily overwhelm the chemical enrichment signal as a function of environment, particularly at high redshifts. In addition, the diverse definition of environment makes comparisons across different studies ambiguous (Ellison et al. 2009; Peng & Maiolino 2014). Cosmological simulations with a full 3-dimensional formation history of cluster galaxies are a powerful tool to overcome observational biases and understand the physics of the environmental dependence of the chemical evolution (Davé et al. 2011; Genel 2016; Bahe et al. 2016).

In this Letter, we explore the MZR evolution as a function of the formation history of galaxy groups and clusters in IllustrisTNG, a large-scale cosmological simulation. Using a novel method of separating progenitor cluster galaxies into accreted and infalling categories, we report for the first time a clear systematic signature of "chemical pre-processing" in cluster galaxies over the past 10 Gyrs. We show the effectiveness of pre-enriched gas inflows in driving the chemical evolution of cluster galaxies out to twice the virial radius.

5.2 Methods

Our results are based on the IllustrisTNG simulations (Pillepich et al. 2018; Nelson et al. 2017; Springel et al. 2017; Marinacci et al. 2017; Naiman et al. 2018). The galaxy formation model is an updated and extended version of the Illustris model (Vogelsberger et al. 2013; Torrey et al. 2014). Details of the model modifications are described in Weinberger et al. (2017) and Pillepich et al. (2017). We use the TNG100 simulation that has a volume of $\sim (100\,\mathrm{Mpc})^3$ and $m_b = 9.4 \times 10^5\,\mathrm{M}_\odot$, where m_b is the baryonic mass per particle.

From the TNG100 simulation, we select all halos with $M_{200c} \geq 10^{13.0}\,\mathrm{M}_\odot$ where M_{200c} is total mass enclosed within R_{200c} (the radius within which the mean density is 200 times the critical density of the Universe at the halo redshift). This leads to a selection of 127 galaxy clusters and groups at $z = 0$. The mean cluster halo mass of our sample is $10^{13.4}\,\mathrm{M}_\odot$. We define the boundary of a cluster as twice the R_{200c} of the cluster halo, which is similar to the splashback radius (Diemer et al. 2017). Out of all Friends-of-Friends (FOF) subhalos associated with the cluster at $z = 0$, all galaxies whether centrals or satellites residing within twice the R_{200c} make up our

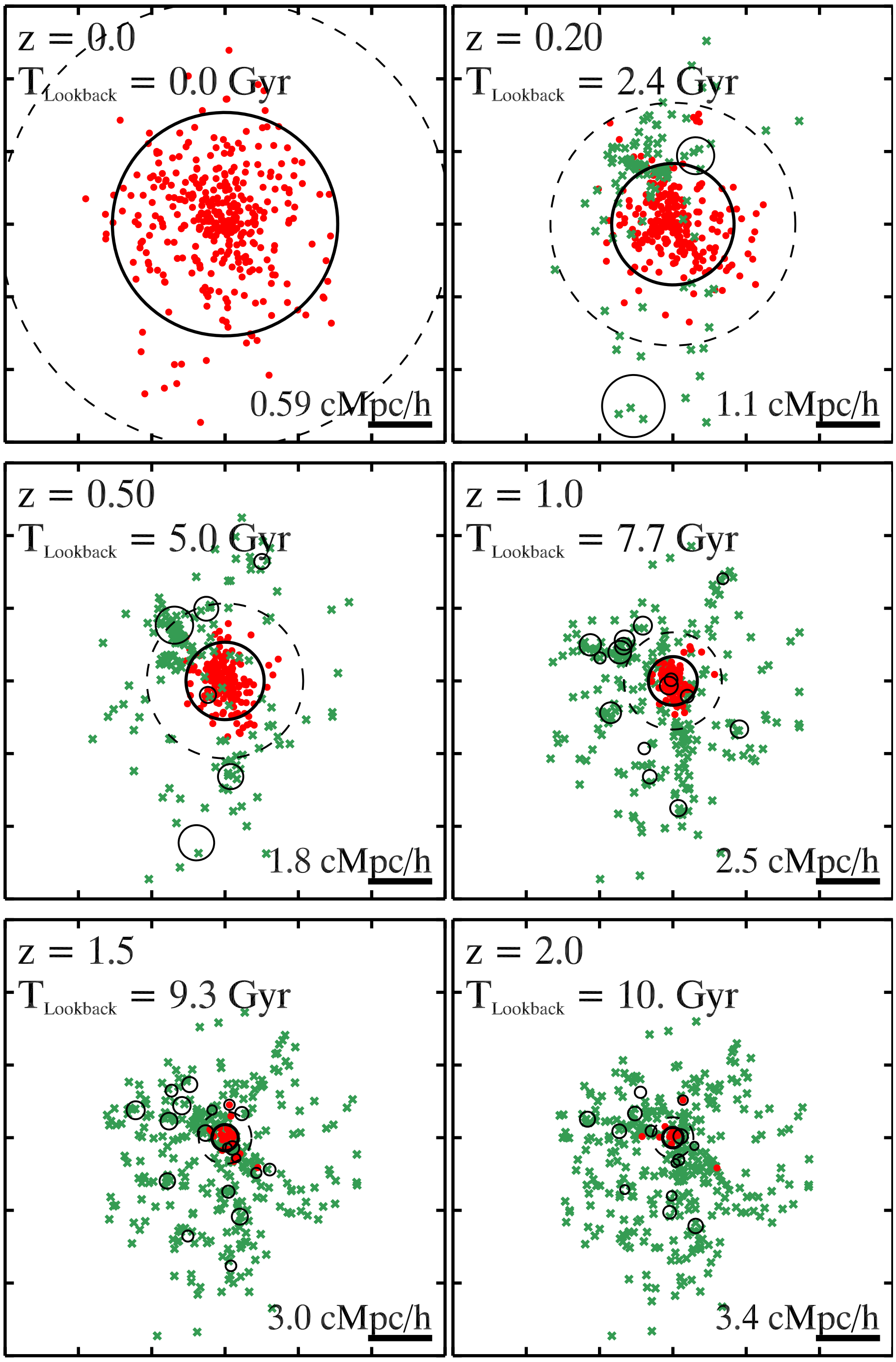

Figure 5.1: The assembly history of the most massive galaxy cluster ($10^{14.4}\,M_\odot$) in the TNG100 simulation from the projected spatial distribution of cluster members. The red circles and green asterisks represent accreted ($z_{\rm infall} > z$) and infalling ($z_{\rm infall} < z$) cluster members respectively. The solid black circles corresponds to the R_{200c} of the dark matter halos associated with the progenitor cluster galaxies. The dashed-black circle represents the cluster boundary ($2\times R_{200c}$) at each snapshot. All distances are represented in projected comoving scale. Throughout this Letter we present the evolution of physical properties of galaxies in six redshift slices $z = [0.0, 0.2, 0.5, 1.0, 1.5, 2.0]$.

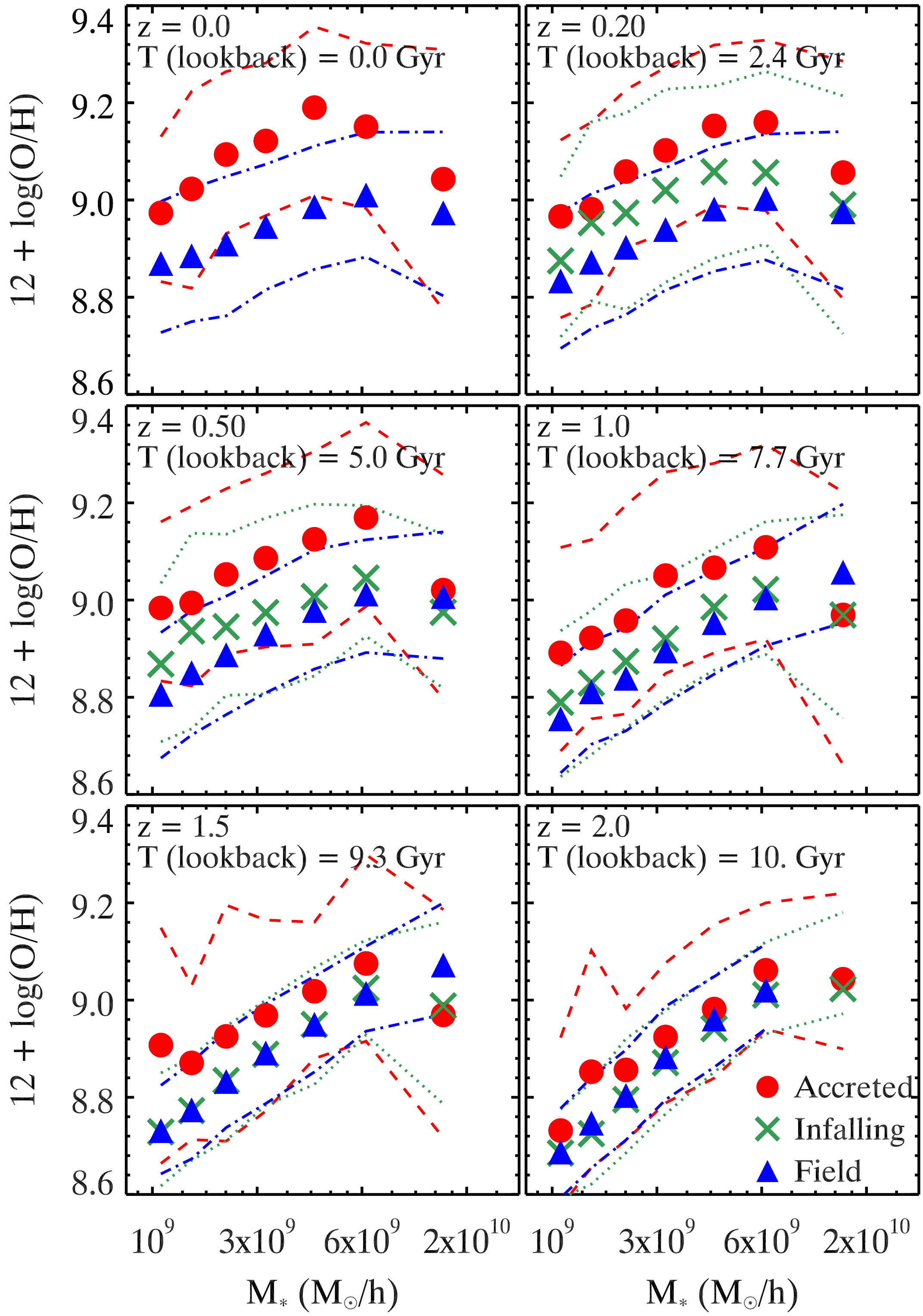

Figure 5.2: Evolution of the mass-metallicity relation for the accreted cluster (red circles), infalling cluster (green asterisks) and field galaxies (blue triangle). At any given redshift, we are plotting the mean SFR-weighted gas-phase metallicity of galaxies with SFR>0. The coloured dashed and dotted lines represents the 16th and 84th percentiles. The accreted cluster members show nearly $0.10-0.18$ dex metal enhancement with respect to field galaxies at each stellar mass bin at $z \leq 1.5$. The infalling cluster members show $0.05-0.08$ dex metal enhancement with respect to field galaxies at $z \leq 0.5$ suggesting chemical pre-processing of infalling galaxies.

cluster member galaxy sample. Note that we exclude flybys and satellite galaxies in the process of splashing back at $z = 0$ from our analysis.

We restrict this analysis to a stellar mass range of $10^9 - 10^{10.5}\,\mathrm{M_\odot}$. The lower stellar mass cut is to minimize numerical uncertainties such that there are at least 1000 stellar particles per galaxy (a single star particle in TNG100 has a mass of about $10^6\,\mathrm{M_\odot}$). We impose the upper mass cut of $< 10^{10.5}\,\mathrm{M_\odot}$ to reduce contaminations from active galactic nuclei (AGN) activities (Pillepich et al. 2018). The removal of high-mass star-forming ($M_* > 10^{10.5}\,\mathrm{M_\odot}$) galaxies does not change our results significantly because environmental effects are more efficient for low mass galaxies. We select 3567 cluster member galaxies with stellar mass $10^9 - 10^{10.5}\,\mathrm{M_\odot}$, without any star formation rates (SFR) cut at $z = 0$. Most cluster galaxies at $z = 0$ are not forming stars.

Our field galaxy sample consists of 8900 galaxies at $z = 0$ that reside in host halos of mass $M_{200c} < 10^{12.0}\,\mathrm{M_\odot}$, have SFR > 0, and $10^9 < M_* < 10^{10.5}\,\mathrm{M_\odot}$. We focus on the SFR-weighted gas-phase metallicity represented in terms of fractional oxygen abundance ($12 + \log(\mathrm{O/H})$) to facilitate a direct comparison with the nebular metallicity observations. Throughout this Letter the stellar mass and SFR are measured within twice the stellar half mass radius. Our SFR-weighted gas metallicity is independent of aperture and has been found to provide a good approximation of the global metallicity from observations (Davé et al. 2011; Bahe et al. 2016; Torrey et al. 2017).

We track *all* $z = 0$ cluster and field galaxies back in time, but galaxies with stellar mass between $10^9 - 10^{10.5}\,\mathrm{M_\odot}$ and SFR > 0 at a given redshift, will only be shown in Figure 5.2, 5.3 and 5.4. We use merger tree catalog based on the technique of Rodriguez-Gomez et al. (2015) to track progenitors of the cluster and field galaxy samples at $z = 0$. At each redshift slice, we use the host halo of the progenitor central cluster galaxy to identify the cluster center and the cluster boundary based on its R_{200c}. We estimate z_{infall} for each progenitor of the present-day cluster member galaxy as the earliest time (highest redshift) at which the galaxy crosses the cluster boundary ($R < 2\times R_{200c}$ of the central cluster halo) for the first time. Using z_{infall}, we separate progenitor cluster galaxies into two subgroups at each redshift slice: accreted ($z_{\mathrm{infall}} > z$) and infalling ($z_{\mathrm{infall}} < z$) galaxies.

This technique can unambiguously separate the infalling galaxies from the accreted cluster galaxies that are on their second passage into the cluster potential. At each redshift, the progenitors of the field galaxy sample form our comparison sample. Figure 5.1 shows the assembly history of the most massive cluster in TNG100 ($M_{200c} = 10^{14.4}\,\mathrm{M_\odot}$) through the projected spatial distribution of progenitors at a few redshift snapshots. At high redshift ($z \sim 1.5$), progenitor cluster galaxies have a comoving spatial extent of $\sim 10 - 20\,\mathrm{Mpc}/h$, consistent with the recent work by Chiang et al. (2017).

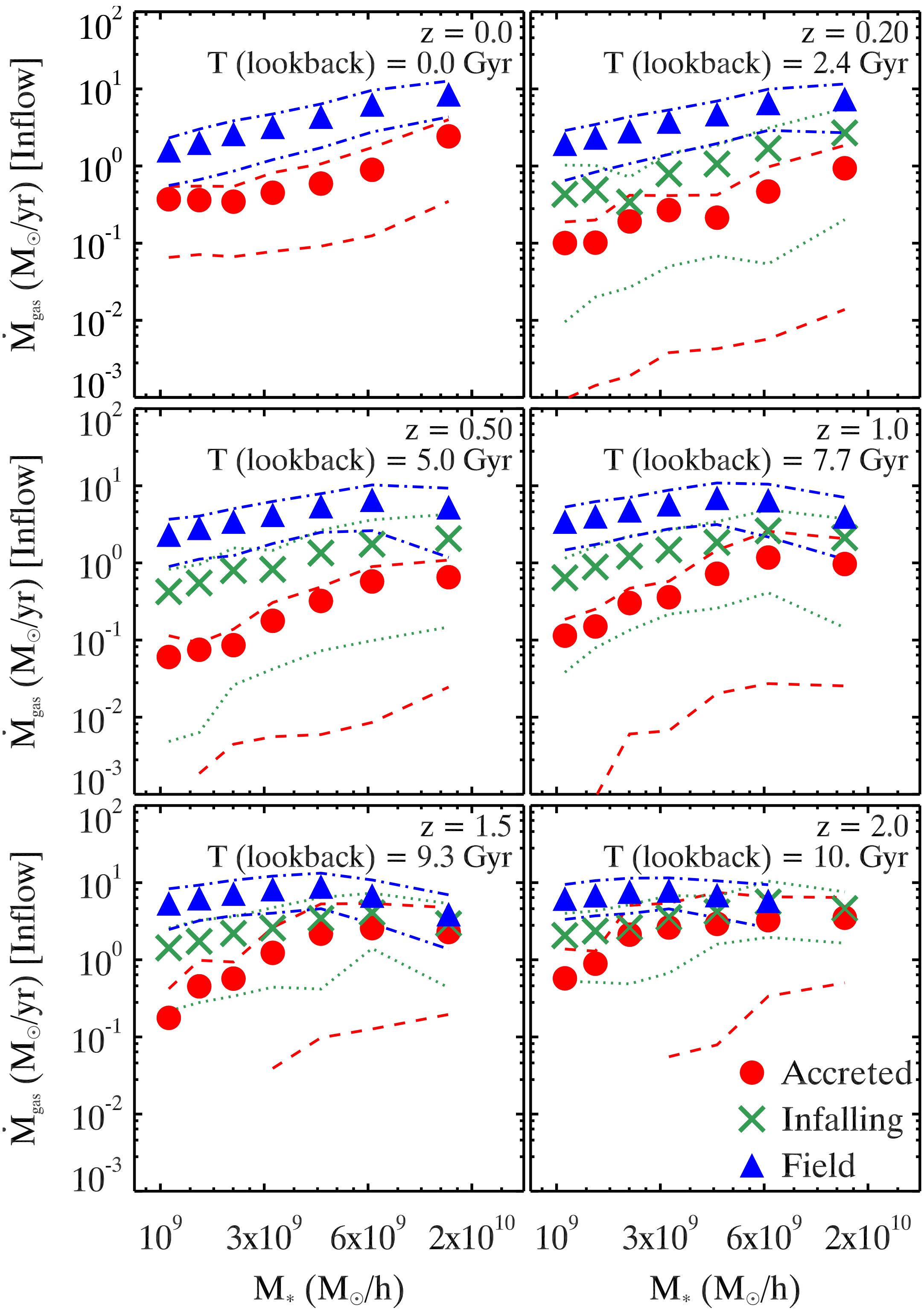

Figure 5.3: Gas mass inflow rate versus stellar mass for the accreted cluster (red circles), infalling cluster (green asterisks) and field (blue triangles) galaxies. Only star-forming galaxies (SFR> 0) are included in the analysis at any given redshift. The data points represent the mean gas mass inflow rate, and the lines indicate the 16th and 84th percentiles for the respective sample. At each redshift snapshot, cluster satellite galaxies have consistently lower gas inflow rates compared to field galaxies.

5.3 Results

5.3.1 Cosmic evolution of the mass-metallicity relation with environment

Figure 5.2 shows the stellar mass versus SFR-weighted gas-phase metallicity for our three galaxy samples (accreted cluster, infalling cluster, and field) at six different redshifts. We restrict our gas metallicity analysis only to galaxies with SFR > 0 at any given redshift. We bin the data by stellar mass such that each stellar mass bin has nearly the same number of galaxies at $z = 0$. At any given redshift, we use the same stellar mass bins defined at $z = 0$ and only plot bins that have at least 10 galaxies. The MZR of accreted and infalling galaxies is consistent with the MZR of the field galaxy sample at $z = 2.0$. Signs of the environmental dependence of metallicity emerge around $z = 1.5$, in particular the low mass accreted galaxies ($< 10^{9.5}\,\mathrm{M_\odot}$) are ~ 0.05 dex more metal-rich compared to counterpart field galaxies. At $z \leq 1.0$, the gas-phase metallicity of accreted cluster galaxies show a consistent metallicity enhancement of $0.15 - 0.20$ dex with respect to field galaxies.

The MZR of infalling galaxies lies persistently in between accreted and field galaxies for $z \sim 0 - 2$, signalling the action of chemical pre-processing in infalling galaxies before they are fully accreted onto their respective clusters. The low mass infalling galaxies ($< 10^{9.5}\,\mathrm{M_\odot}$) at $z = 0.5$ show an offset of ~ 0.05 dex from the counterpart field galaxies. The metal enhancement permeates to even higher mass infalling galaxies ($< 10^{10}\,\mathrm{M_\odot}$) at $z \sim 0.2$. The infalling galaxies have not crossed the cluster boundary ($2\times R_{200c}$), hence the metallicity offset between infalling cluster and field galaxies appears prior to infall. Our MZR analysis shows for the first time a systematic signature of chemical pre-processing in infalling galaxies. In this Letter, we use the term pre-processing more broadly to describe the modification in the properties of galaxies prior to infall onto the main cluster irrespective of their prior group membership.

The MRZ evolution of cluster and field shows a qualitative agreement with observations (Ellison et al. 2009; Pilyugin et al. 2017a), though a detailed quantitative comparison with observations is not feasible because of discrepancies in emission line diagnostics (Kewley & Ellison 2008), the choice of nucleosynthesis yields in the simulations, diverse definition of environments, and selection effects. Most observations find a maximum of 0.05 dex metallicity enhancement for cluster galaxies (Pilyugin et al. 2017a), significantly lower than the one predicted by simulations. Contamination by interlopers or infalling galaxies due to projection effects and the lack of dynamic time estimates can easily wash out the metallicity enhancement in observations. Also, a higher SFR cut in observations specifically removes cluster galaxies undergoing change due to the environment. We test different SFR cuts and find a maximum SFR cut of $0.1\,\mathrm{M_\odot}$/yr is required to observe the environment driven changes in the metallicity, any higher SFR cut will dilute the observed metallicity enhancement.

The simulation shows a 1-sigma scatter of ~ 0.20 dex in the MZR. The large scatter underlines the cluster-to-cluster variation and shows the challenge of detecting the metallicity enhancement with relatively small cluster samples in observations. Meanwhile, we notice that the scatter of the simulated MZR at $z \sim 0$ seems to be large in comparison with observations (e.g., Pilyugin et al. 2017a). We plan to investigate the origin of the scatter in more detail in a future work. Simulations predict no significant evolution in the average metallicity of the highest mass bin ($10^{10} - 10^{10.5}\,M_{\odot}$) between $z = 2.0$ to $z = 0.0$ for any galaxy sample. The average metallicity in the highest mass bin is biased towards galaxies with either extremely low SFRs and/or significant AGN contribution.

5.3.2 Properties of gas accretion in high-density environment

To understand the origin of the environmental dependence of the MZR and the chemical pre-processing, we investigate the gas accretion history of our three samples using Monte Carlo tracer particles (Genel et al. 2013). At any given redshift, we measure the tracer flux associated with baryons entering the galaxy for the first time over a time interval of 1 Gyr. We then multiply the tracer count with an effective tracer mass to estimate a "raw gas mass inflow rate" (Nelson et al. 2015). The median number of tracer particles associated with the gas mass inflow rate is about $800 - 15000$.

Figure 5.3 shows the average gas mass inflow rate for the three samples (accreted, infalling and field) in six redshift slices. We find that the gas mass inflow rate is consistently lower by $0.4 - 1.0$ dex for accreted and infalling cluster galaxies compared to field galaxies across all redshift slices. The difference in the average gas mass inflow rate between cluster (accreted and infalling) and field galaxies increases slightly with cosmic time, i.e., increases from ~ 0.4 dex at $z = 2.0$ to ~ 1.0 dex at $z < 0.5$. Almost 50% of accreted cluster galaxies with non-zero gas mass inflow rate and SFRs have been accreted onto the main cluster in the past 2 Gyrs. In TNG100, cluster galaxies have on average 0.5 dex lower SFRs than field galaxies at all epochs. Torrey et al. (2017) show that the MZR of field galaxies evolves through either the accretion dominant or enrichment dominant phase.

Figure 5.4 shows the redshift evolution of the mean metallicity of the inflowing gas. The average metallicity of the baryons associated with the raw gas mass inflow rate is defined as the mean metallicity of inflowing gas. The mass abundance of all metals used in Figure 5.4 relates to the oxygen number abundance by a simple multiplicative factor (~ 0.03). The average metallicity of the inflowing gas increases with cosmic time, irrespective of the galaxy sample or the stellar mass bin. However, galaxies in the cluster environment (accreted or infalling) receive more metal-rich inflowing gas than galaxies in the field, and relatively more so at lower redshifts (Figures 5.4). Even at $z = 1.5$, accreted cluster galaxies are receiving almost 1.3 times more metal-rich gas than field galaxies; at $z \sim 0$ the difference in metal content can be

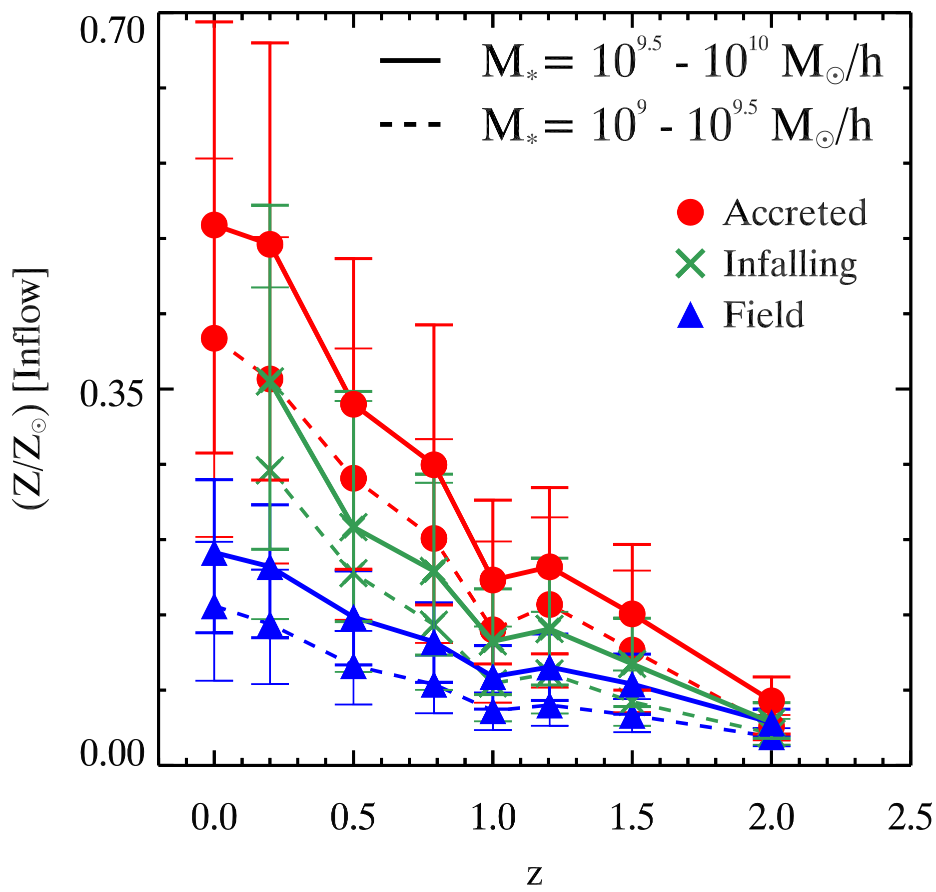

Figure 5.4: Cosmic evolution of the mean metallicity of the inflowing gas for cluster (red), infalling (green) and field (blue) galaxies. The solid and dashed lines represent galaxies in stellar mass bins labeled in the figure. The inflowing gas for both accreted and infalling cluster galaxies is $2-3$ times more metal rich at $z=0$ than field galaxies. Note that we are plotting the total metal content not the fractional oxygen abundance.

as large as a factor of 3. Yet, the inflowing gas mass rate is ~ 1.0 dex lower for cluster galaxies than field galaxies. We also find a secondary positive correlation in the metallicity of inflowing gas and the stellar mass, consistent with previous suggestions (Fraternali 2017; Kacprzak et al. 2016).

The average metallicity of the inflowing gas for infalling galaxies continues to lie in-between accreted cluster and field galaxies at all epochs (Figure 5.4). In fact, at $z < 0.5$, infalling galaxies are accreting $1.5 - 2$ times more metal-rich gas compared to field galaxies. The infalling galaxies have never crossed the boundary of the central cluster potential ($2\times R_{200c}$) and are receiving metal-rich gas compared to field galaxies, suggesting that enriched gas inflows can be significant at distances larger than $2\times R_{200c}$. Figure 5.3 and Figure 5.4 suggest that the enriched gas inflows contribute significantly to the chemical enrichment of galaxies in overdense environments.

5.4 Discussion and Conclusion

Using the IllustrisTNG cosmological simulation, we demonstrate the first systematic signature of "chemical pre-processing" of infalling cluster galaxies, namely galaxies which will be accreted by $z = 0$ into a massive host. Before infall, these galaxies exhibit a ~ 0.05 dex enhancement in the MZR in comparison to field galaxies, a difference observable at low redshifts ($z < 0.5$, Figure 5.2). The simulation also predicts a systematic pre-enrichment of the gas which is available for inflow into cluster galaxies (Figure 5.4). At $z < 1.0$, cluster galaxies (both already accreted and infalling) accrete gas which is $2 - 3$ times more metal-rich compared to field galaxies.

We suggest that infalling galaxies exhibiting pre-processing signatures may or may not belong to smaller, infalling groups, a distinction that will be checked in a follow-up paper. The underlying pre-processing physical mechanisms do not act necessarily on the cluster galaxies themselves, but rather on the gas around them which is available for accretion. Gas removal via gravitational or hydrodynamic interactions in infalling groups has instead previously been suspected as the cause of pre-processing of infalling galaxies (Cortese et al. 2006; Scott et al. 2015). Our definition of cluster boundary to separate infalling and accreted cluster galaxies is similar to the splashback radius (Diemer et al. 2017). The signature of chemical pre-processing can be used as an observational identification for the splashback radius.

The metallicity enhancement of cluster galaxies on the MZR is qualitatively consistent with observations and recent investigations of cosmological simulations (Davé et al. 2011; Genel 2016; Bahe et al. 2016). Genel (2016) attribute the metallicity enhancement to either the reduced inflow of metal-poor gas or SFR concentration towards the inner, more metal-rich parts for galaxies with stellar mass $\sim 10^{10.3}\,M_\odot$. Observations show that environmental processes are mostly effective for galaxies with $M_* < 10^{10}\,M_\odot$ (Peng et al. 2010). Chapter 4 shows that star formation suppression in the galactic outskirts due to ram pressure stripping (RPS) can not directly produce a significant enhancement in the SFR-weighted metallicity. However, a relative increase in the metallicity of cluster galaxies compared to field galaxies due to suppression of pristine gas inflow by RPS can not be ruled out. We also consistently find lower gas mass inflow rates for both infalling and accreted cluster galaxies compared to field galaxies in the simulation.

The pre-enrichment of the inflowing gas in clusters follows the cosmic evolution of intra-cluster medium (ICM) enrichment (Vogelsberger et al. 2017). Peng & Maiolino (2014) also suggested that the mixing of the inflowing gas with the metal-rich ICM can be responsible for the pre-enrichment of inflowing gas in the cluster environment. We speculate that the inflow of pre-enriched gas in combination with the suppression of gas inflows drive the chemical pre-processing of infalling galaxies and the metallicity enhancement of star-forming cluster galaxies. Carefully designed observations are needed to confirm the chemical pre-processing of infalling galaxies and the pre-enrichment signal in overdense environment.

Acknowledgements

PT was supported by NASA through Hubble Fellowship grant HST-HF-51384.001-A. MV acknowledges support from a MIT RSC award, the Alfred P. Sloan Foundation, and by NASA ATP grant NNX17AG29G. L.J.K. gratefully acknowledges support from an Australian Research Council (ARC) Laureate Fellowship (FL150100113). T.Y. acknowledges support from an ASTRO 3D fellowship. K. Tran acknowledges support by the National Science Foundation under Grant Number 1410728. Parts of this research were conducted by the Australian Research Council Centre of Excellence for All Sky Astrophysics in 3 Dimensions (ASTRO 3D), through project number CE170100013. The IllustrisTNG simulations and the ancillary runs were run on the HazelHen Cray XC40-system (project GCS-ILLU), Stampede supercomputer at TACC/XSEDE (allocation AST140063), at the Hydra and Draco supercomputers at the Max Planck Computing and Data Facility, and on the MIT/Harvard computing facilities supported by FAS and MIT MKI.

Chapter 6

Concluding Remarks

6.1 General Summary

Local environment transforms star-forming galaxies with spiral disks into spheroidal ellipticals with little or no on-going star formation activity. The chemical abundance of a galaxy (ratio of heavy elements to Hydrogen) is a cumulative product of its star-formation activity modulated by gas inflows and outflows. However, whether environment plays a role in the chemical evolution is still under debate. In this thesis, I use observations, semi-analytical models, and cosmological hydrodynamic simulations to study how the environment impacts the chemical evolution of star-forming galaxies.

In the first part of my thesis, I observe two galaxy clusters at $z \sim 0.35$, MACS1115+01 and RXJ1532+30, with DEIMOS at Keck-II telescope. In Chapter 2, I conduct a systematic quantification of the flux calibration errors for DEIMOS. We find that the standard flux calibration techniques result in a flux calibration accuracy of $\sim 20\%$ for extragalactic objects (Figure 2.6).

In Chapter 3, I find for the first time that the gas-phase metallicity of star-forming cluster galaxies shows a negative correlation with distance from the cluster center, i.e., galaxies towards the cluster center are metal enhanced compared to galaxies in the cluster outskirt (Figure 3.7). The negative cluster-scale gradient is independent of the stellar mass within the limitations of our sample. On the MZ relation, star-forming cluster members for MACS1115+01 are 0.20 dex metal-rich compared to counterpart field galaxies.

In contrast, star-forming cluster members for RXJ1532+30 show a bimodal metallicity distribution with the projected cluster-centric distance (Figure 3.8). The low stellar mass galaxies ($\log(M_*/\mathrm{M}_\odot) < 9.5$) show a positive cluster-scale metallicity gradient whilst galaxies in the high stellar mass bin ($\log(M_*/\mathrm{M}_\odot) > 9.5$) exhibit a negative cluster-scale gradient similar to one observed for MACS1115+01. The MZ relation of cluster members of RXJ1532+30 is statistically consistent with field galaxies (Figure 3.6). I speculate that the low stellar mass galaxies in RXJ1532+30 are part of a merging sub-cluster and/or interlopers. The X-ray observations also show evidence of minor merger with a cooler sub-cluster for RXJ1532+30 (Hlavacek-

Larrondo et al. 2013).

The different cluster-scale metallicity distribution and the MZ relation of the MACS1115+01 and RXJ1532+30 suggests that differences in the dynamical state of galaxy clusters can get imprinted on the chemical properties of the cluster members. Local studies of the MZ relation in high density environments combine data for more than 100 galaxy clusters to achieve a statistically significant sample of star-forming cluster galaxies (Ellison et al. 2009). However, combining data for galaxy clusters at various stages of their formation history can dilute environment-dependent metallicity enhancement signatures.

The cluster-scale abundance gradient provides a new outlook on identifying the environmental impact on the chemical evolution of galaxies. In Chapter 3, I speculate that the negative cluster-scale gradient observed for MACS1115+01 and massive galaxies in RXJ1532+30, can be produced by the disk-truncation via ram pressure stripping (RPS) and/or strangulation. Disk truncation is the concentration of star formation in the central part of a cluster galaxy due to the RPS of the gas from galactic outskirts. Observations of integrated metallicity in disk-truncated galaxies would be biased towards the central, metal-rich part, resulting in the relative metallicity of cluster galaxies compare to field galaxies.

Observations and cosmological simulations suggest that the observational bias introduced by the disk truncation might be sufficient to explain the observed metallicity enhancement of cluster galaxies (Hughes et al. 2013; Genel 2016; Bahe et al. 2016). I combine semi-analytic model of RPS and mock-observation techniques, to test if disk truncation is sufficient to explain the enhanced metallicity of the MZ relation and the negative cluster-scale abundance gradient, as observed for MACS1115+01. In Chapter 4, I generate disk-truncated cluster galaxies by applying semi-analytic model of RPS on galaxies selected from CALIFA survey. We conduct mock-observations of disk-truncated galaxies with same observational constraints as used for our observations in Chapter 3, to make the uncertainties into metallicity measurement from integrated light comparable.

I find that disk truncation produces a minimal cluster-scale abundance gradient or the metallicity enhancement for cluster galaxies on the MZ relation (Figure 4.7 and 4.9). In fact, the small negative cluster-scale metallicity gradient predicted by disk truncation is because the RPS preferentially strips off the gas supply and quenches the star formation for the low mass galaxies near the cluster core. Preferential removal of low stellar mass galaxies from the cluster cores produces a negative stellar mass gradient (Figure 4.10 and 4.11). Numerical simulations show that the semi-analytical model of RPS overestimates the effect of the RPS because of inherent assumptions such as radial orbits, instantaneous stripping (Steinhauser et al. 2016, for more see Section 4.6). My disk-truncation simulation provides an upper-limit on the influence of disk truncation on the integrated metallicity measurement.

The integrated metallicity measurement via nebular emission lines are luminosity weighted, and thus are inherently biased towards the central parts of the galaxy.

Hence, our disk-truncation simulations suggest that the complete suppression of SFR in the galactic outskirts does not significantly affect the integrated metallicity measurement. Other physical processes such as strangulation or enriched inflows are needed to explain the observation of negative abundance gradients and higher metal content of cluster galaxies observed in Chapter 3.

In the last part of my thesis, I use the new generation of cosmological hydrodynamical simulation, (IllustrisTNG; Pillepich et al. 2018) to understand the complex interplay of physical processes governing the chemical evolution in the cluster environment. We utilise the full formation history of cluster galaxies to identify when and where the environment imprints its signature on the chemical evolution of galaxies.

In Chapter 5, I make the first predictions of a systematic signature of the "chemical pre-processing" of cluster galaxies. The infalling[1] cluster galaxies exhibit signs of higher chemical abundance than the counterpart field galaxies (Figure 5.2). The chemical pre-processing signature appears at $z < 0.5$ and is stronger for low mass galaxies. The accreted[2] cluster galaxies at $z < 1.5$ are $0.10 - 0.15$ dex metal rich compare to field galaxies irrespective of the stellar mass bin. The metallicity enhancement of cluster galaxies in simulations is qualitatively consistent with observations.

IllustrisTNG simulations also predict systematic pre-enrichment of the inflowing gas in high density environments, in particular at $z < 1.0$ (Figure 5.4). The inflowing gas for both infalling and accreted cluster galaxies is $2 - 3$ times more metal-rich compared to the gas flowing into field galaxies. In fact, the evolution of pre-enrichment of inflowing gas follows the evolution of ICM enrichment, suggesting that the mixing with the enriched ICM is responsible for the enrichment of inflowing gas.

Using simulation and observations in this thesis (Chapter 3 and 5), I show that environment plays a secondary but significant role in the chemical evolution of galaxies. I find that galaxies in high density environment are $0.10 - 0.15$ dex metal rich compare to field galaxies. I prove that suppression of star-formation in outer galactic disks because of RPS, is not sufficient to explain high metal content of cluster galaxies. Using cosmological hydrodynamic simulations, I identify that the accretion of pre-enriched gas and the reduced gas mass inflow rate are key drivers of chemical evolution in the high density environment, in particular for galaxies in the stellar mass range $10^9 < M_* < 10^{10}\,\mathrm{M}_\odot$. This thesis shows that the signature of environment-dependent changes in properties of inflowing gas extends to infalling galaxies, i.e., for galaxies well outside the virial radius of clusters.

[1]yet to cross the cluster boundary

[2]have crossed the cluster boundary at least once

6.2 Future Work

During my PhD, I have gained extensive experience with simulations and observations, ideally placing me to tackle the debate on the physical drivers of the baryonic cycle in the cluster environment in unprecedented detail. Cosmological simulations are an excellent tool to understand selection effects and observational biases and can greatly improve the design of future observations aimed at observing the small environment dependent chemical signatures.

6.2.1 Observations

Using mock observations from cosmological simulations, I find that the key criteria to successfully detect the environment-dependent chemical evolution signatures in observations are (1) a well-defined cluster sample with a range of dynamic states, (2) a self-consistent control field sample, (3) a minimal SF cut of SFR $> 0.1\,\mathrm{M_\odot}$/year, (4) a minimal number of clusters to minimize cluster-to-cluster variations, (5) a large covering distance ($\sim 3 \times R_{200c}$) and, (6) reliable metallicity diagnostics across different redshift ranges.

Chemical pre-processing of infalling galaxies and cluster-scale Abundance Gradient

In Chapter 5, I make first prediction of chemical pre-processing of infalling galaxies. I will use deep and wide-field spectroscopic observations of intermediate redshift ($0.2 < z < 0.6$) galaxy clusters to observationally confirm the chemical pre-processing signature. Most current spectroscopic follow-ups target galaxies within one virial radius, but my work with IllustrisTNG simulations suggests that observations of galaxies out to $2 - 5\,R_{200c}$ are required to identify signature of chemical pre-processing.

In Chapter 3, the two clusters show that the cluster-scale abundance distribution depends on the dynamical state or the formation history of the galaxy cluster (Figure 3.7). By selecting a larger and dynamically diverse sample of galaxy clusters at intermediate redshift ($0.2 < z < 0.6$), I will confirm the existence of a cluster-scale abundance gradient and its dependence on the dynamical state of the cluster. I will also analyse the dependence of the cluster-scale scale abundance gradient on other global properties of galaxy clusters such as the X-ray temperature and the halo mass.

Cosmic Evolution of Cluster-scale Abundance Gradient

In Chapter 5, I show that the onset of environmental impact on metallicity evolution of galaxies happens between $z = 1.5$ and $z = 2.0$ (Figure 5.2). The impact is most significant for galaxies of $\log(M_*/\mathrm{M}_\odot) < 9.5$. The past $3-4$ years have seen an explosion in the number of confirmed galaxy clusters at $z > 1.0$ using a variety of observational techniques in surveys such as Wylezalek et al. (CARLA; 2013), Franck & McGaugh (CCPC; 2016) and Paterno-Mahler et al. (COBRA; 2016). Hence, deeper spectroscopic surveys aimed at identifying the epoch of onset of environmental impact on galaxy evolution are extremely timely. I will use near-infrared spectrographs such as MOSFIRE/Keck, KMOS/VLT, to acquire deep spectroscopic data for galaxy clusters at redshift $z > 1.0$.

6.2.2 Quantitative Comparison with IllustrisTNG simulations

In Chapter 5, I focused on the properties of the inflowing gas such as mass inflow rate and metallicity, and how those change in the overdense environment. I am currently working on a follow-up paper analysing the properties of the gas outflows and their dependence on the large-scale environment. This work will track the properties of gas flowing in and out of cluster galaxies, and their relative effect on the chemical evolution of star-forming cluster galaxies in unprecedented details. My work with IllustrisTNG simulations shows that simulations are excellent tool for understanding the relative significance of various observational biases and selection effects. By incrementally incorporating various observational effects such as projection and SFR cut in simulated cluster galaxies, I will constrain their relative significance in the cluster-scale abundance gradient and the mass-metallicity relation observations.

This thesis focuses on the gas-phase metallicity and its dependence on the environment, but observations of other baryonic components such as gas, dust and stars are essential to construct a cohesive picture of baryonic cycle in cluster environment. ALMA has revolutionised the understanding of gas physics in high redshift Universe especially for the high redshift galaxy clusters and protoclusters. Future observations with ALMA of cold gas in intermediate redshift galaxy clusters would provide useful insight into gas dynamics in galaxy clusters.

Bibliography

Abadi M. G., Moore B., Bower R. G., 1999, Monthly Notices of the Royal Astronomical Society, 308, 947

Abazajian K. N., et al., 2009, The Astrophysical Journal Supplement Series, 182, 543

Abell G. O., 1965, Annual Review of Astronomy and Astrophysics, 3, 1

Abramson A., Kenney J. D. P., Crowl H. H., Chung A., van Gorkom J. H., Vollmer B., Schiminovich D., 2011, The Astronomical Journal, 141, 164

Adami C., Biviano A., Durret F., Mazure A., 2005, Astronomy and Astrophysics, 443, 17

AdelmanMcCarthy J. K., et al., 2006, The Astrophysical Journal Supplement Series, 162, 38

Alam S., et al., 2015, The Astrophysical Journal Supplement Series, 219, 12

Allen S. W., Rapetti D. A., Schmidt R. W., Ebeling H., Morris R. G., Fabian A. C., 2007, Monthly Notices of the Royal Astronomical Society, 383, 879

Andrews B. H., Martini P., 2013, The Astrophysical Journal, 765, 140

Annunziatella M., et al., 2016, Astronomy & Astrophysics, 585, A160

Aragón-Salamanca A., Bedregal A. G., Merrifield M. R., 2006, Astronomy and Astrophysics, 458, 101

Arnouts S., Cristiani S., Moscardini L., Matarrese S., Lucchin F., Fontana A., Giallongo E., 1999, Monthly Notices of the Royal Astronomical Society, 310, 540

Bahe Y. M., Schaye J., Crain R. A., McCarthy I. G., Bower R. G., Theuns T., McGee S. L., Trayford J. W., 2016, Monthly Notices of the Royal Astronomical Society, 464, 508

Baldry I. K., Balogh M. L., Bower R. G., Glazebrook K., Nichol R. C., Bamford S. P., Budavari T., 2006, Monthly Notices of the Royal Astronomical Society, 373, 469

Baldwin a., Phillips M. M., Terlevich R., 1981, Publications of the Astronomical Society of the Pacific, 93, 817

Balogh M. L., Morris S. L., Yee H. K. C., Carlberg R. G., Ellingson E., 1999, The Astrophysical Journal, 527, 54

Balogh M. L., Navarro J. F., Morris S. L., 2000, The Astrophysical Journal, 540, 113

Balogh M., et al., 2004, Monthly Notices of the Royal Astronomical Society, 348, 1355

Barrera-Ballesteros J. K., Sánchez S. F., Heckman T., Blanc G. A., 2017, The Astrophysical Journal, 844, 80

Bayliss M. B., Hennawi J. F., Gladders M. D., Koester B. P., Sharon K., Dahle H., Oguri M., 2011, The Astrophysical Journal Supplement Series, 193, 8

Bedregal A. G., Cardiel N., Aragón-Salamanca A., Merrifield M. R., 2011, Monthly Notices of the Royal Astronomical Society, 415, 2063

Bekki K., 2009, Monthly Notices of the Royal Astronomical Society, 399, 2221

Bekki K., 2014, Monthly Notices of the Royal Astronomical Society, 438, 444

Bellhouse C., et al., 2017, The Astrophysical Journal, 844, 49

Bellstedt S., Forbes D. A., Foster C., Romanowsky A. J., Brodie J. P., Pastorello N., Alabi A., Villaume A., 2017, Monthly Notices of the Royal Astronomical Society, 467, 4540

Berrier J. C., Stewart K. R., Bullock J. S., Purcell C. W., Barton E. J., Wechsler R. H., 2009, The Astrophysical Journal, 690, 1292

Bialas D., Lisker T., Olczak C., Spurzem R., Kotulla R., 2015, Astronomy & Astrophysics, 576, A103

Bianconi M., Smith G. P., Haines C. P., McGee S. L., Finoguenov A., Egami E., 2018, Monthly Notices of the Royal Astronomical Society: Letters, 473, L79

Bigiel F., Blitz L., 2012, The Astrophysical Journal, 756, 183

Blake C., et al., 2011, Monthly Notices of the Royal Astronomical Society, 418, 1707

Bohlin R. C., Gordon K. D., Tremblay P.-E., 2014, Publications of the Astronomical Society of the Pacific, pp 000–000

Boselli A., Cortese L., Boquien M., 2014a, Astronomy & Astrophysics, 564, A65

Boselli A., Cortese L., Boquien M., 2014b, Astronomy & Astrophysics, 564, A65

Bosma A., 2016, eprint arXiv:1612.05272, pp 1–38

Brinchmann J., Charlot S., White S. D. M., Tremonti C., Kauffmann G., Heckman T., Brinkmann J., 2004, Monthly Notices of the Royal Astronomical Society, 351, 1151

Broadhurst T. J., Ellis R. S., Koo D. C., Szalay A. S., 1990, Nature, 343, 726

Brown T., et al., 2017a, Monthly Notices of the Royal Astronomical Society, 466, 1275

Brown T., et al., 2017b, Monthly Notices of the Royal Astronomical Society, 466, 1275

Bruzual G., Charlot S., 2003, Monthly Notices of the Royal Astronomical Society, 344, 1000

Budzynski J. M., Koposov S. E., McCarthy I. G., McGee S. L., Belokurov V., 2012, Monthly Notices of the Royal Astronomical Society, 423, 104

Calzetti D., Armus L., Bohlin R. C., Kinney A. L., Koornneef J., StorchiBergmann T., 2000, The Astrophysical Journal, 533, 682

Cappellari M., Emsellem E., 2004, Publications of the Astronomical Society of the Pacific, 116, 138

Casado J., Ascasibar Y., Gavilán M., Terlevich R., Terlevich E., Hoyos C., Díaz A. I., 2015, Monthly Notices of the Royal Astronomical Society, 451, 888

Chabrier G., 2003, Publications of the Astronomical Society of the Pacific, 115, 763

Chiang Y.-K., Overzier R. A., Gebhardt K., Henriques B., 2017, The Astrophysical Journal, 844, L23

Chung A., van Gorkom J. H., Kenney J. D. P., Crowl H., Vollmer B., 2009, The Astronomical Journal, 138, 1741

Collister A. A., Lahav O., 2005, Monthly Notices of the Royal Astronomical Society, 361, 415

Consolandi G., Gavazzi G., Fossati M., Fumagalli M., Boselli A., Yagi M., Yoshida M., 2017, Astronomy & Astrophysics, 606, A83

Cooper M. C., Tremonti C. A., Newman J. A., Zabludoff A. I., 2008, Monthly Notices of the Royal Astronomical Society, 390, 245

Cooper M. C., et al., 2011, The Astrophysical Journal Supplement Series, 193, 14

Cooper M. C., et al., 2012, Monthly Notices of the Royal Astronomical Society, 419, 3018

Cora S. A., Tornatore L., Tozzi P., Dolag K., 2008, Monthly Notices of the Royal Astronomical Society, 386, 96

Cormier D., et al., 2016, Monthly Notices of the Royal Astronomical Society, 463, 1724

Cortese L., Gavazzi G., Boselli A., Franzetti P., Kennicutt R. C., O'Neil K., Sakai S., 2006, Astronomy & Astrophysics, 453, 847

Cortese L., et al., 2007, Monthly Notices of the Royal Astronomical Society, 376, 157

Cortese L., et al., 2010, Astronomy and Astrophysics, 518, L63

Cortese L., Catinella B., Boissier S., Boselli A., Heinis S., 2011, Monthly Notices of the Royal Astronomical Society, 415, 1797

Cowie L. L., Songaila A., Hu E. M., Cohen J. G., 1996, The Annals of Statistics, 112, 839

Daddi E., et al., 2007, The Astrophysical Journal, 670, 156

Darvish B., Mobasher B., Sobral D., Hemmati S., Nayyeri H., Shivaei I., 2015a, The Astrophysical Journal, 814, 84

Darvish B., Mobasher B., Sobral D., Hemmati S., Nayyeri H., Shivaei I., 2015b, The Astrophysical Journal, 814, 84

Darvish B., Mobasher B., Martin D. C., Sobral D., Scoville N., Stroe A., Hemmati S., Kartaltepe J., 2017, The Astrophysical Journal, 837, 16

Davé R., Finlator K., Oppenheimer B. D., 2011, Monthly Notices of the Royal Astronomical Society, 416, 1354

Davis M., Meiksin A., Strauss M. A., da Costa L. N., Yahil A., 1988, The Astrophysical Journal, 333, L9

Davis M., et al., 2002, Proceedings of the SPIE, 4834, 12

De Grandi S., Molendi S., 2001, The Astrophysical Journal, 551, 153

De Grandi S., et al., 2016, Astronomy & Astrophysics, 592, A154

De Lucia G., Blaizot J., 2007, Monthly Notices of the Royal Astronomical Society, 375, 2

De Lucia G., Kauffmann G., White S. D. M., 2004, Monthly Notices of the Royal Astronomical Society, 349, 1101

De Rossi M. E., Theuns T., Font A. S., Mccarthy I. G., 2015, Monthly Notices of the Royal Astronomical Society, 452, 486

Diemer B., Mansfield P., Kravtsov A. V., More S., 2017, The Astrophysical Journal, 843, 140

Doi M., et al., 2010, The Astronomical Journal, 139, 1628

Dopita M. A., Kewley L. J., Sutherland R. S., Nicholls D. C., 2016, Astrophysics and Space Science, 311, 177

Dressler A., 1980, The Astrophysical Journal, 236, 351

Dressler A., Gunn J. E., 1982, The Astrophysical Journal, 263, 533

Dressler A., Gunn J. E., 1983, The Astrophysical Journal, 270, 7

Dressler A., Shectman S. a., 1988, The Astronomical Journal, 95, 985

Dutton A. A., Macciò A. V., 2014, Monthly Notices of the Royal Astronomical Society, 441, 3359

Ebeling H., Edge a. C., Böhringer H., Allen S. W., Crawford C. S., Fabian a. C., Voges W., Huchra J. P., 1998, in Monthly Notices of the Royal Astronomical Society. pp 881–914 (`arXiv:9812394`), doi:10.1046/j.1365-8711.1998.01949.x, `http://arxiv.org/abs/astro-ph/9812394`

Ebeling H., Edge A. C., Mantz A., Barrett E., Henry J. P., Ma C. J., van Speybroeck L., 2010, Monthly Notices of the Royal Astronomical Society, 407, 83

Ebeling H., Ma C.-J., Barrett E., 2014, The Astrophysical Journal Supplement Series, 211, 21

Eisenstein D. J., et al., 2005, The Astrophysical Journal, 633, 560

Elbaz D., et al., 2007, in Astronomy and Astrophysics. pp 33–48 (`arXiv:0703653`), doi:10.1051/0004-6361:20077525, `http://adsabs.harvard.edu/abs/2007A{%}26A...468...33E`

Ellison S. L., Patton D. R., Simard L., McConnachie A. W., 2008, The Astrophysical Journal, 672, L107

Ellison S. L., Simard L., Cowan N. B., Baldry I. K., Patton D. R., McConnachie A. W., 2009, Monthly Notices of the Royal Astronomical Society, 396, 1257

Erfanianfar G., et al., 2016, Monthly Notices of the Royal Astronomical Society, 455, 2839

Faber S. M., et al., 2003, Proc. SPIE, 4841, 1657

Fitzpatrick E. L., 1999, Publications of the Astronomical Society of the Pacific, 111, 63

Franck J. R., McGaugh S. S., 2016, The Astrophysical Journal, 817, 158

Fraternali F., 2017, Astrophysics and Space Science Library, pp 323–353

Gavazzi G., Randone I., Branchini E., 1995, The Astrophysical Journal, 438, 590

Genel S., 2016, The Astrophysical Journal, 822, 107

Genel S., Vogelsberger M., Nelson D., Sijacki D., Springel V., Hernquist L., 2013, Monthly Notices of the Royal Astronomical Society, 435, 1426

Genel S., et al., 2017, preprint (arXiv:1707.05327), 000

George M. R., Ma C.-P., Bundy K., Leauthaud A., Tinker J., Wechsler R. H., Finoguenov A., Vulcani B., 2013, The Astrophysical Journal, 770, 113

Gianninas A., Bergeron P., Ruiz M. T., 2011, The Astrophysical Journal, 743, 138

González Delgado R. M., et al., 2014, The Astrophysical Journal, 791, L16

Gonzalez A. H., Sivanandam S., Zabludoff A. I., Zaritsky D., 2013, The Astrophysical Journal, 778, 14

Groenewegen M., Lamers H., 1989, Astronomy and Astrophysics Supplement Series, 79, 359

Gunn J. E., Gott J. R. I., 1972, The Astrophysical Journal, 176, 1

Guo Q., et al., 2011, Monthly Notices of the Royal Astronomical Society, 413, 101

Guo Q., Cole S., Eke V., Frenk C., Helly J., 2013, Monthly Notices of the Royal Astronomical Society, 434, 1838

Gupta A., Yuan T., Tran K.-V. H., Martizzi D., Taylor P., Kewley L. J., 2016, The Astrophysical Journal, 831, 104

Hahn O., Martizzi D., Wu H.-Y., Evrard A. E., Teyssier R., Wechsler R. H., 2015, preprint, 000 (arXiv:1509.04289)

Hausman M. A., Ostriker J. P., 1978, The Astrophysical Journal, 224, 320

Haynes M. P., Giovanelli R., Kent B. R., 2007, The Astrophysical Journal, 665, L19

Heß S., Springel V., 2012, Monthly Notices of the Royal Astronomical Society, 426, 3112

Hinshaw G., et al., 2013, The Astrophysical Journal Supplement Series, 208, 19

Hlavacek-Larrondo J., et al., 2013, The Astrophysical Journal, 777, 163

Ho I.-T., Kudritzki R.-P., Kewley L. J., Zahid H. J., Dopita M. a., Bresolin F., Rupke D. S. N., 2015, Monthly Notices of the Royal Astronomical Society, 448, 2030

Hou A., Parker L. C., Harris W. E., 2014, Monthly Notices of the Royal Astronomical Society, 442, 406

Houghton R. C. W., 2015, Monthly Notices of the Royal Astronomical Society, 451, 3427

Hubble E., Humason M. L., 1931, The Astrophysical Journal, 74, 43

Hughes T. M., Cortese L., 2009, Monthly Notices of the Royal Astronomical Society: Letters, 396, 41

Hughes T. M., Cortese L., Boselli A., Gavazzi G., Davies J. I., 2013, Astronomy & Astrophysics, 550, A115

Huss A., Jain B., Steinmetz M., 1999, The Astrophysical Journal, 517, 64

Ilbert O., et al., 2006, Astronomy and Astrophysics, 457, 841

Jáchym P., Köppen J., Palouš J., Combes F., 2009, Astronomy and Astrophysics, 500, 693

Jáchym P., Sun M., Combes F., Cortese L., Kenney J. D., 2014, Proceedings of the International Astronomical Union, 10, 227

Jáchym P., et al., 2017, The Astrophysical Journal, 839, 114

Jones D. H., et al., 2009, Monthly Notices of the Royal Astronomical Society, 399, 683

Jones T., Ellis R. S., Richard J., Jullo E., 2013, The Astrophysical Journal, 765, 48

Kaasinen M., Bian F., Groves B., Kewley L., Gupta A., 2016, Monthly Notices of the Royal Astronomical Society, 465, 3220

Kacprzak G. G., et al., 2015, The Astrophysical Journal, 802, L26

Kacprzak G. G., et al., 2016, The Astrophysical Journal, 826, L11

Kale R., Venturi T., Giacintucci S., Dallacasa D., Cassano R., Brunetti G., Macario G., Athreya R., 2013, Astronomy & Astrophysics, 557, A99

Kang X., van den Bosch F. C., 2008, The Astrophysical Journal, 676, L101

Kapferer W., et al., 2007, Astronomy and Astrophysics, 466, 813

Kapferer W., et al., 2009, Astronomy & Astrophysics, 504, 719

Kauffmann G., et al., 2003a, Monthly Notices of the Royal Astronomical Society, 341, 54

Kauffmann G., et al., 2003b, Monthly Notices of the Royal Astronomical Society, 346, 1055

Kauffmann G., White S. D. M., Heckman T. M., M??nard B., Brinchmann J., Charlot S., Tremonti C., Brinkmann J., 2004, Monthly Notices of the Royal Astronomical Society, 353, 713

Kawinwanichakij L., et al., 2017, The Astrophysical Journal, 847, 134

Kennicutt, Jr. R. C., 1998, in The Astrophysical Journal. pp 541–552 (`arXiv:9712213`), doi:10.1086/305588

Kewley L. J., Dopita M. a., 2002, The Astrophysical Journal Supplement Series, 142, 35

Kewley L. J., Ellison S. L., 2008, The Astrophysical Journal, 681, 1183

Kewley L. J., Dopita M. a., Sutherland R. S., Heisler C. a., Trevena J., 2001, The Astrophysical Journal, 556, 121

Kewley L. J., Jansen R. A., Geller M. J., 2005, Publications of the Astronomical Society of the Pacific, 117, 227

Kewley L. J., Groves B., Kauffmann G., Heckman T., 2006, Monthly Notices of the Royal Astronomical Society, 372, 961

Kewley L. J., Maier C., Yabe K., Ohta K., Akiyama M., Dopita M. A., Yuan T., 2013a, The Astrophysical Journal, 774, L10

Kewley L. J., Dopita M. A., Leitherer C., Davé R., Yuan T., Allen M., Groves B., Sutherland R., 2013b, The Astrophysical Journal, 774, 100

Kewley L. J., Zahid H. J., Geller M. J., Dopita M. a., Hwang H. S., Fabricant D., 2015, The Astrophysical Journal, 812, L20

Kewley L. J., et al., 2016, The Astrophysical Journal, 819, 100

Kimm T., et al., 2009, Monthly Notices of the Royal Astronomical Society, 394, 1131

Kobulnicky H. a., Kewley L. J., 2004, The Astrophysical Journal, 617, 240

Kovač K., et al., 2014, Monthly Notices of the Royal Astronomical Society, 438, 717

Laganá T. F., Ulmer M. P., 2018, Monthly Notices of the Royal Astronomical Society, 475, 523

Lara-López M. A., et al., 2010, Astronomy and Astrophysics, 521, L53

Larson R. B., Tinsley B. M., Caldwell C. N., 1980, The Astrophysical Journal, 237, 692

Le Fèvre O., et al., 2005, Astronomy and Astrophysics, 439, 845

LeFevre O., et al., 2003, Instrument Design and Performance for Optical/Infrared Ground-based Telescopes, 4841, 1670

Lee H., Skillman E. D., Cannon J. M., Jackson D. C., Gehrz R. D., Polomski E. F., Woodward C. E., 2006, The Astrophysical Journal, 647, 970

Lee S.-K., Im M., Kim J.-W., Lotz J., McPartland C., Peth M., Koekemoer A., 2015, The Astrophysical Journal, 810, 90

Lequeux J., Peimbert M., Rayo J., Serrano A., Torres-Peimbert S., 1979, Astronomy & Astrophysics, 80, 155

Lewis I., et al., 2002, Monthly Notices of the Royal Astronomical Society, 334, 673

Lilly S. J., et al., 2007, The Astrophysical Journal Supplement Series, 172, 70

Lopes P. A. A., Ribeiro A. L. B., Rembold S. B., 2014, Monthly Notices of the Royal Astronomical Society, 437, 2430

Luo Y., Kang X., Kauffmann G., Fu J., 2016, Monthly Notices of the Royal Astronomical Society, 458, 366

Madau P., Dickinson M., 2014, Annual Review of Astronomy and Astrophysics, 52, 415

Maier C., et al., 2016, Astronomy & Astrophysics, 590, A108

Maiolino R., et al., 2008, Astronomy & Astrophysics, 488, 463

Makino N., Sasaki S., Suto Y., 1998, The Astrophysical Journal, 497, 555

Mannucci F., Cresci G., Maiolino R., Marconi A., Gnerucci A., 2010, Monthly Notices of the Royal Astronomical Society, 408, 2115

Marinacci F., et al., 2017, preprint (arXiv:1707.03396), 26, 1

Martínez H. J., Coenda V., Muriel H., 2008, Monthly Notices of the Royal Astronomical Society, 391, 585

Martizzi D., Hahn O., Wu H.-y., Evrard A. E., Teyssier R., Wechsler R. H., 2016, Monthly Notices of the Royal Astronomical Society, 459, 4408

Mastropietro C., Moore B., Mayer L., Debattista V. P., Piffaretti R., Stadel J., 2005, Monthly Notices of the Royal Astronomical Society, 364, 607

McCarthy I. G., Frenk C. S., Font A. S., Lacey C. G., Bower R. G., Mitchell N. L., Balogh M. L., Theuns T., 2008, Monthly Notices of the Royal Astronomical Society, 383, 593

McLean I. S., et al., 2012, in McLean I. S., Ramsay S. K., Takami H., eds, Vol. 8446, Ground-based and Airborne Instrumentation for Astronomy IV. Proceedings of the SPIE. p. 84460J, doi:10.1117/12.924794, http://adsabs.harvard.edu/abs/2012SPIE.8446E..0JMhttp://proceedings.spiedigitallibrary.org/proceeding.aspx?doi=10.1117/12.924794

McPartland C., Ebeling H., Roediger E., Blumenthal K., 2016, Monthly Notices of the Royal Astronomical Society, 455, 2994

Méndez-Abreu J., et al., 2017, Astronomy & Astrophysics, 598, A32

Merten J., et al., 2015, The Astrophysical Journal, 806, 4

Monroe J. T., Tran K.-V. H., Gonzalez A. H., 2017, The Astrophysical Journal, 836, 1

Moore B., Katz N., Lake G., Dressler A., Oemler A., 1996, Nature, 379, 613

Mosleh M., Williams R. J., Franx M., 2013, The Astrophysical Journal, 777, 117

Mouhcine M., Baldry I. K., Bamford S. P., 2007, Monthly Notices of the Royal Astronomical Society, 382, 801

Munari U., et al., 2014, The Astronomical Journal, 148, 81

Muzzin A., et al., 2012, Astrophysical Journal, 746

Muzzin A., et al., 2014, The Astrophysical Journal, 796, 65

Naiman J. P., et al., 2018, Monthly Notices of the Royal Astronomical Society, 18, 1

Natarajan P., et al., 2017, Monthly Notices of the Royal Astronomical Society, 468, 1962

Navarro J. F., Frenk C. S., White S. D. M., 1997, The Astrophysical Journal, 490, 493

Nelson D., Genel S., Vogelsberger M., Springel V., Sijacki D., Torrey P., Hernquist L., 2015, Monthly Notices of the Royal Astronomical Society, 448, 59

Nelson D., et al., 2017, preprint (arXiv:1707.03395)

Newman J. a., et al., 2013, The Astrophysical Journal Supplement Series, 208, 5

Odekon M. C., et al., 2016, The Astrophysical Journal, 824, 17

Oi N., Goto T., Malkan M., Pearson C., Matsuhara H., 2017, Publications of the Astronomical Society of Japan, 69, 1

Oke J. B., 1990, The Astronomical Journal, 99, 1621

Oke J. B., et al., 1995, Publications of the Astronomical Society of the Pacific, 107, 375

Onodera M., et al., 2016, The Astrophysical Journal, 822, 42

Osterbrock D. E., 1989, Astrophysics of gaseous nebulae and active galactic nuclei. `http://adsabs.harvard.edu/abs/1989agna.book.....O`

Ostriker J. P., Tremaine S. D., 1975, The Astrophysical Journal, 202, L113

Owen F. N., Keel W. C., Wang Q. D., Ledlow M. J., Morrison G. E., 2006, The Astronomical Journal, 131, 1974

Owers M. S., Couch W. J., Nulsen P. E. J., Randall S. W., 2012, The Astrophysical Journal, 750, L23

Paccagnella A., et al., 2016, The Astrophysical Journal, 816, L25

Paccagnella A., et al., 2017, The Astrophysical Journal, 838, 148

Pasquali A., Gallazzi A., van den Bosch F. C., 2012, Monthly Notices of the Royal Astronomical Society, 425, 273

Paterno-Mahler R., Blanton E. L., Brodwin M., Ashby M. L. N., Golden-Marx E., Decker B., Wing J. D., Anand G., 2016, arXiv e-prints

Peng Y.-j., Maiolino R., 2014, Monthly Notices of the Royal Astronomical Society, 438, 262

Peng Y.-j., et al., 2010, The Astrophysical Journal, 721, 193

Peng Y.-j., Lilly S. J., Renzini A., Carollo M., 2012, The Astrophysical Journal, 757, 4

Peng Y., Maiolino R., Cochrane R., 2015, Nature, 521, 192

Petropoulou V., Vílchez J., Iglesias-Páramo J., 2012, The Astrophysical Journal, 749, 133

Pettini M., Pagel B. E. J., 2004, Monthly Notices of the Royal Astronomical Society, 348, 5

Phillips M. M., Jenkins C. R., Dopita M. A., Sadler E. M., Binette L., 1986, The Astronomical Journal, 91, 1062

Pickles A., Depagne É., 2010, Publications of the Astronomical Society of the Pacific, 122, 1437

Pillepich A., et al., 2017, preprint (arXiv:1707.03406), 000

Pillepich A., et al., 2018, Monthly Notices of the Royal Astronomical Society, 473, 4077

Pilyugin L. S., Grebel E. K., Zinchenko I. A., Nefedyev Y. A., Mattsson L., 2017a, Monthly Notices of the Royal Astronomical Society, 465, 1358

Pilyugin L. S., Grebel E. K., Zinchenko I. A., Nefedyev Y. A., Mattsson L., 2017b, Monthly Notices of the Royal Astronomical Society, 465, 1358

Poggianti B. M., Smail I., Dressler A., Couch W. J., Barger A. J., Butcher H., Ellis R. S., Oemler, Jr. A., 1999, The Astrophysical Journal, 518, 576

Poggianti B. M., et al., 2017, The Astrophysical Journal, 844, 48

Postman M., et al., 2012, The Astrophysical Journal Supplement Series, 199, 25

Pota V., et al., 2013, Monthly Notices of the Royal Astronomical Society, 428, 389

Rasia E., et al., 2015, The Astrophysical Journal, 813, L17

Rauch T., Werner K., Bohlin R., Kruk J. W., 2013, Astronomy & Astrophysics, 560, A106

Ribeiro A., Lopes P., Rembold S., 2013, Astronomy & Astrophysics, 556, A74

Richard J., Jones T., Ellis R., Stark D. P., Livermore R., Swinbank M., 2011, Monthly Notices of the Royal Astronomical Society, 413, 643

Riess A. G., et al., 1998, The Astronomical Journal, 116, 1009

Rodriguez-Gomez V., et al., 2015, Monthly Notices of the Royal Astronomical Society, 449, 49

Rodríguez del Pino B., et al., 2017, Monthly Notices of the Royal Astronomical Society, 20, stx228

Roediger E., Brüggen M., 2006, Monthly Notices of the Royal Astronomical Society, 369, 567

Roediger E., Brüggen M., 2007, Monthly Notices of the Royal Astronomical Society, 380, 1399

Roediger E., Hensler G., 2005, Astronomy and Astrophysics, 433, 875

Sánchez S. F., et al., 2012, Astronomy & Astrophysics, 538, A8

Sánchez S. F., et al., 2014, Astronomy & Astrophysics, 563, A49

Sánchez S. F., et al., 2016, Astronomy & Astrophysics, 594, A36

Sánchez S. F., et al., 2017, Monthly Notices of the Royal Astronomical Society, 469, 2121

Sanders R. L., et al., 2015, The Astrophysical Journal, 799, 138

Scannapieco C., et al., 2012, Monthly Notices of the Royal Astronomical Society, 423, 1726

Schaye J., et al., 2014, Monthly Notices of the Royal Astronomical Society, 446, 521

Schenker M. A., Stark D. P., Ellis R. S., Robertson B. E., Dunlop J. S., McLure R. J., Kneib J. P., Richard J., 2012, Astrophysical Journal, 744

Scott T. C., Usero A., Brinks E., Bravo-Alfaro H., Cortese L., Boselli A., Argudo-Fernández M., 2015, Monthly Notices of the Royal Astronomical Society, 453, 328

Scoville N., et al., 2007, The Astrophysical Journal Supplement Series, 172, 150

Scudder J. M., Ellison S. L., Mendel J. T., 2012, Monthly Notices of the Royal Astronomical Society, 423, 2690

Serna A., Gerbal D., 1996, Astronomy and Astrophysics, 309, 65

Shapley H., 1933, Proceedings of the National Academy of Science, 19, 591

Shapley A. E., et al., 2014, Astrophysical Journal, 801, 88

Shields G. A., Skillman E. D., Kennicutt, Robert C. J., 1991, The Astrophysical Journal, 371, 82

Shimakawa R., Kodama T., Tadaki K.-i., Hayashi M., Koyama Y., Tanaka I., 2015a, Monthly Notices of the Royal Astronomical Society, 448, 666

Shimakawa R., et al., 2015b, Monthly Notices of the Royal Astronomical Society, 451, 1284

Shimakawa R., et al., 2018, Monthly Notices of the Royal Astronomical Society, 473, 1977

Skillman E. D., Kennicutt, Robert C. J., Shields G. A., Zaritsky D., 1996, The Astrophysical Journal, 462, 147

Smith R., et al., 2015, Monthly Notices of the Royal Astronomical Society, 454, 2502

Sobral D., et al., 2015, Monthly Notices of the Royal Astronomical Society, 451, 2303

Springel V., Frenk C. S., White S. D. M., 2006, Nature, 440, 1137

Springel V., et al., 2017, preprint (arXiv:1707.03397), 23, 1

Steinhauser D., Schindler S., Springel V., 2016, Astronomy & Astrophysics, 591, A51

Sun M., Jones C., Forman W., Nulsen P. E. J., Donahue M., Voit G. M., 2006, The Astrophysical Journal Letters, 637, L81

Suzuki R., et al., 2008, Publications of the Astronomical Society of Japan, 60, 1347

Suzuki T. L., et al., 2017, The Astrophysical Journal, 849, 39

Swaters R. a., van Albada T. S., van der Hulst J. M., Sancisi R., 2005, Astronomy & Astrophysics, 390, 829

Tanaka M., et al., 2013, The Astrophysical Journal, 772, 113

Taranu D. S., Hudson M. J., Balogh M. L., Smith R. J., Power C., Oman K. a., Krane B., 2014, Monthly Notices of the Royal Astronomical Society, 440, 1934

Taylor P., Kobayashi C., 2015, Monthly Notices of the Royal Astronomical Society, 448, 1835

Tecce T. E., Cora S. A., Tissera P. B., Abadi M. G., Lagos C. d. P., 2010, Monthly Notices of the Royal Astronomical Society, 408, 2008

Tegmark M., et al., 2004, Physical Review D, 69, 103501

Telford O. G., Dalcanton J. J., Skillman E. D., Conroy C., 2016, The Astrophysical Journal, 827, 35

Tonnesen S., Bryan G. L., 2012, Monthly Notices of the Royal Astronomical Society, 422, 1609

Torrey P., Vogelsberger M., Genel S., Sijacki D., Springel V., Hernquist L., 2014, Monthly Notices of the Royal Astronomical Society, 438, 1985

Torrey P., et al., 2017, 000

Tran K. V. H., et al., 2010, Astrophysical Journal Letters, 719, 126

Tran K.-V. H., et al., 2015, The Astrophysical Journal, 811, 28

Tremonti C. A., et al., 2004, The Astrophysical Journal, 613, 898

Valentino F., et al., 2015, The Astrophysical Journal, 801, 132

Van Den Bosch F. C., Aquino D., Yang X., Mo H. J., Pasquali A., McIntosh D. H., Weinmann S. M., Kang X., 2008, Monthly Notices of the Royal Astronomical Society, 387, 79

Van der Wel A., 2008, The Astrophysical Journal, 675, L13

Vazdekis a., Sánchez-Blázquez P., Falcón-Barroso J., Cenarro a. J., Beasley M. a., Cardiel N., Gorgas J., Peletier R. F., 2010, Monthly Notices of the Royal Astronomical Society, 32, 1

Veilleux S., Osterbrock D. E., 1987, The Astrophysical Journal Supplement Series, 63, 295

Vogelsberger M., Genel S., Sijacki D., Torrey P., Springel V., Hernquist L., 2013, Monthly Notices of the Royal Astronomical Society, 436, 3031

Vogelsberger M., et al., 2014a, Monthly Notices of the Royal Astronomical Society, 444, 1518

Vogelsberger M., et al., 2014b, Nature, 509, 177

Vogelsberger M., et al., 2017, preprint (arXiv:1707.05318), 21, 1

Vulcani B., et al., 2011, Monthly Notices of the Royal Astronomical Society, 412, 246

Wagner C. R., Courteau S., Brodwin M., Stanford S. A., Snyder G. F., Stern D., 2016, The Astrophysical Journal, 834, 53

Walcher C. J., et al., 2014, Astronomy & Astrophysics, 569, A1

Wang J., et al., 2014, Monthly Notices of the Royal Astronomical Society, 441, 2159

Weinberger R., et al., 2017, Monthly Notices of the Royal Astronomical Society, 465, 3291

Weinmann S. M., Kauffmann G., Van Den Bosch F. C., Pasquali A., McIntosh D. H., Mo H., Yang X., Guo Y., 2009, Monthly Notices of the Royal Astronomical Society, 394, 1213

Wetzel A. R., Tinker J. L., Conroy C., van den Bosch F. C., 2013, Monthly Notices of the Royal Astronomical Society, 432, 336

Wu H.-Y., Evrard A. E., Hahn O., Martizzi D., Teyssier R., Wechsler R. H., 2015, Monthly Notices of the Royal Astronomical Society, 452, 1982

Wuyts E., et al., 2016, The Astrophysical Journal, 827, 74

Wylezalek D., et al., 2013, The Astrophysical Journal, 769, 79

Yahil A., Vidal N. V., 1977, The Astrophysical Journal, 214, 347

York D. G., et al., 2000, The Astronomical Journal, 120, 1579

Yuan T.-T., Kewley L. J., Swinbank a. M., Richard J., Livermore R. C., 2011, The Astrophysical Journal, 732, L14

Yuan T.-T., Kewley L. J., Richard J., 2013a, The Astrophysical Journal, 763, 9

Yuan T.-T., Kewley L. J., Rich J., 2013b, The Astrophysical Journal, 767, 106

Zabludoff A. I., Mulchaey J. S., 1998, The Astrophysical Journal, 496, 39

Zahid H. J., Kewley L. J., Bresolin F., 2011, The Astrophysical Journal, 730, 137

Zahid H. J., Bresolin F., Kewley L. J., Coil A. L., Davé R., 2012, Astrophysical Journal, 750

Zahid H. J., Geller M. J., Kewley L. J., Hwang H. S., Fabricant D. G., Kurtz M. J., 2013, The Astrophysical Journal, 771, L19

Zahid H. J., Dima G. I., Kudritzki R.-P., Kewley L. J., Geller M. J., Hwang H. S., Silverman J. D., Kashino D., 2014a, The Astrophysical Journal, 791, 130

Zahid H. J., et al., 2014b, The Astrophysical Journal, 792, 75

Zandivarez A., Martínez H. J., 2011, Monthly Notices of the Royal Astronomical Society, 415, 2553

Zaritsky D., Kennicutt, Robert C. J., Huchra J. P., 1994, The Astrophysical Journal, 420, 87

Zenteno A., et al., 2016, Monthly Notices of the Royal Astronomical Society, 462, 830

Appendices

Appendix A

The offset from the mass-metallicity relation

From observations presented in Chapter 3, we separate the effect of mass and environment on the chemical evolution by sudying the offset in cluster member metallicity from the mass-metallicity relation of the local comparison sample. For MACS1115+01, cluster members in the inner parts show enhanced metallicity at a fixed stellar mass range compared to cluster members in the outskirts (Figure A.1: left panel). In contrast, cluster members in RXJ1532+30 do not show a correlation between the metallicity offset and the projected distance (Figure A.1: right panel). The existence of the negative gradient in the offset from mass-metallicity relation for MACS1115+01 suggests that the cluster-scale negative abundance gradient is not driven by the stellar mass of galaxies. However, our conclusion is limited by the small sample size of our data.

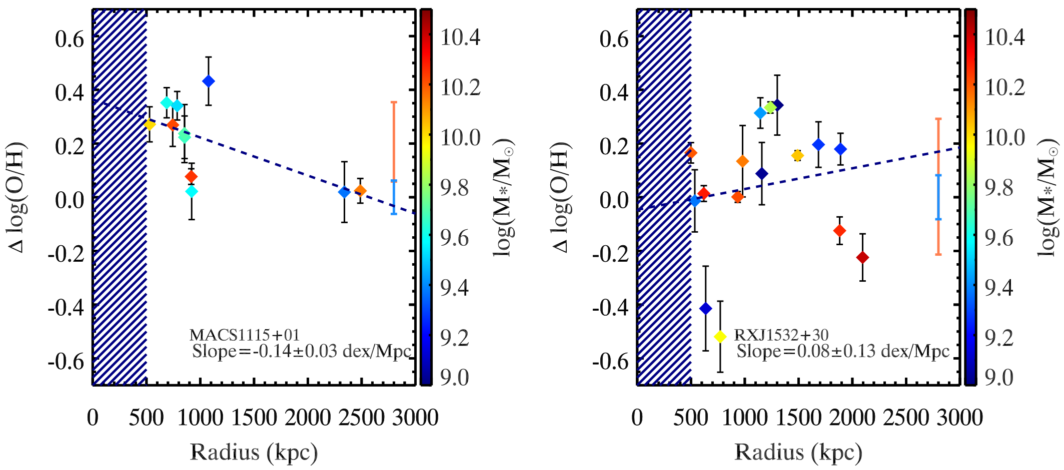

Figure A.1: The offset from the mass-metallicity relation of the local comparison sample (Figure 3.6: red curve) with the projected distance. **Left panel:** MACS1115+01, and **right panel:** RXJ1532+30. The dashed line represents the best linear fit. The slope and standard error in slope are labelled in each figure. The blue and red error bar represents the scatter and median metallicity offset of the comparison sample and the cluster data. The offset from the MZR also exhibit anti-correlation with the projected distance for MACS1115+01, which suggests that the metallicity enhancement towards the cluster center is not driven the stellar mass.

Appendix B

Estimation of stellar mass gradient in disk truncation simulation

In section 4.5.3, we compare the stellar mass gradient in our disk truncation simulation with the predicted cluster-scale gradient in integrated metallicity. The $\nabla M^{*}_{\rm cl}$ is the best-fit slope between the stellar mass of galaxies and the cluster-centric distance for a single realisation of disk truncation simulation. For each realisation of disk truncation simulation, we measure a $\nabla M^{*}_{\rm cl}$ before and after applying the RPS model. The $\nabla M^{*}_{\rm cl}$ after stripping is measured by only including galaxies for which gas-phase metallicity can be estimated. Figure B.1 shows the stellar mass distribution for three realisations of the disk truncation simulation before and after stripping. For realisations with an initial $\nabla M^{*}_{\rm cl}$ equal to either positive or negative, the $\nabla M^{*}_{\rm cl}$ after truncation remains statistically unchanged (Figure B.1: top & bottom rows). Whereas, the disk truncation realisation with a zero $\nabla M^{*}_{\rm cl}$ before stripping can have a $\nabla M^{*}_{\rm cl}$ after stripping (Figure B.1: middle row).

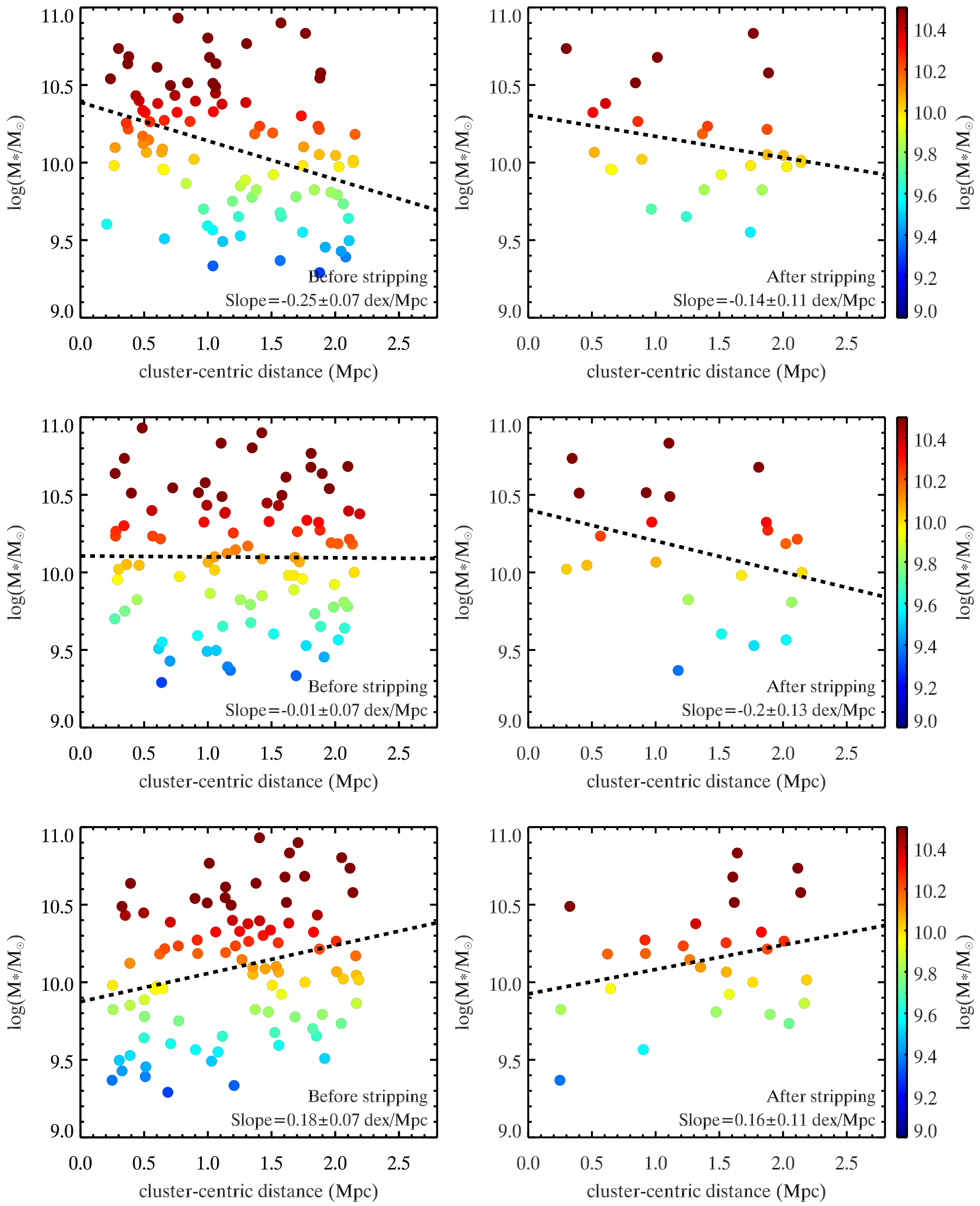

Figure B.1: Examples demonstrating the estimation of $\nabla M^*_{\rm cl}$ for different realisations of disk truncation simulations. The left column shows the stellar mass distribution with the cluster-centric distance before implementing the RPS model. The right column shows the stellar mass distribution of truncated cluster galaxies with measurable gas-phase metallicities. The dashed line in each panel represents the best linear fit to the data. The data points in each figure are color coded with stellar mass. The $\nabla M^*_{\rm cl}$ before stripping is positive in first row, zero in the middle row and negative for the last row. The $\nabla M^*_{\rm cl}$ for the first and the last row remains statistically the same after stripping but the $\nabla M^*_{\rm cl}$ shifts to negative value for the middle row after stripping.